

## INFORMATION TO USERS

While the most advanced technology has been used to photograph and reproduce this manuscript, the quality of the reproduction is heavily dependent upon the quality of the material submitted. For example:

- Manuscript pages may have indistinct print. In such cases, the best available copy has been filmed.
- Manuscripts may not always be complete. In such cases, a note will indicate that it is not possible to obtain missing pages.
- Copyrighted material may have been removed from the manuscript. In such cases, a note will indicate the deletion.

Oversize materials (e.g., maps, drawings, and charts) are photographed by sectioning the original, beginning at the upper left-hand corner and continuing from left to right in equal sections with small overlaps. Each oversize page is also filmed as one exposure and is available, for an additional charge, as a standard 35mm slide or as a 17"x 23" black and white photographic print.

Most photographs reproduce acceptably on positive microfilm or microfiche but lack the clarity on xerographic copies made from the microfilm. For an additional charge, 35mm slides of 6"x 9" black and white photographic prints are available for any photographs or illustrations that cannot be reproduced satisfactorily by xerography.



8712883

Iverson, Arthur Evan

THE MATHEMATICAL MODELING OF TIME-DEPENDENT  
PHOTOCONDUCTIVE PHENOMENA IN SEMICONDUCTORS

*The University of Arizona*

PH.D. 1987

University  
Microfilms  
International 300 N. Zeeb Road, Ann Arbor, MI 48106



**PLEASE NOTE:**

In all cases this material has been filmed in the best possible way from the available copy. Problems encountered with this document have been identified here with a check mark .

1. Glossy photographs or pages \_\_\_\_\_
2. Colored illustrations, paper or print \_\_\_\_\_
3. Photographs with dark background \_\_\_\_\_
4. Illustrations are poor copy \_\_\_\_\_
5. Pages with black marks, not original copy \_\_\_\_\_
6. Print shows through as there is text on both sides of page \_\_\_\_\_
7. Indistinct, broken or small print on several pages
8. Print exceeds margin requirements \_\_\_\_\_
9. Tightly bound copy with print lost in spine \_\_\_\_\_
10. Computer printout pages with indistinct print \_\_\_\_\_
11. Page(s) \_\_\_\_\_ lacking when material received, and not available from school or author.
12. Page(s) \_\_\_\_\_ seem to be missing in numbering only as text follows.
13. Two pages numbered \_\_\_\_\_. Text follows.
14. Curling and wrinkled pages \_\_\_\_\_
15. Dissertation contains pages with print at a slant, filmed as received
16. Other \_\_\_\_\_  
\_\_\_\_\_  
\_\_\_\_\_

University  
Microfilms  
International



THE MATHEMATICAL MODELING OF TIME-DEPENDENT  
PHOTOCONDUCTIVE PHENOMENA IN SEMICONDUCTORS

by

Arthur Evan Iverson

---

A Dissertation Submitted to the Faculty of the  
COMMITTEE ON APPLIED MATHEMATICS

In Partial Fulfillment of the Requirements  
For the Degree of

DOCTOR OF PHILOSOPHY

In the Graduate College

THE UNIVERSITY OF ARIZONA

1987

---

THE UNIVERSITY OF ARIZONA  
GRADUATE COLLEGE

As members of the Final Examination Committee, we certify that we have read  
the dissertation prepared by Arthur Evan Iverson

entitled The Mathematical Modeling of Time-Dependent Photoconductive  
Phenomena in Semiconductors

and recommend that it be accepted as fulfilling the dissertation requirement  
for the Degree of Doctor of Philosophy.

Olyvid A. Polusinski 4/20/87  
Date

John A. Reardon 4/20/87  
Date

DW McFarr 4/20/87  
Date

\_\_\_\_\_  
Date

\_\_\_\_\_  
Date

Final approval and acceptance of this dissertation is contingent upon the  
candidate's submission of the final copy of the dissertation to the Graduate  
College.

I hereby certify that I have read this dissertation prepared under my  
direction and recommend that it be accepted as fulfilling the dissertation  
requirement.

Olyvid A. Polusinski 4/20/87  
Dissertation Director Date

## STATEMENT BY AUTHOR

This dissertation has been submitted in partial fulfillment of requirements for an advanced degree at the University of Arizona and is deposited in the University Library to be made available to borrowers under rules of the library.

Brief quotations from this dissertation are allowable without special permission, provided that accurate acknowledgement of source is made. Requests for permission for extended quotation from or reproduction of this manuscript in whole or in part may be granted by the head of the major department or the Dean of the Graduate College when in his or her judgment the proposed use of the material is in the interest of scholarship. In all other instances, however, permission must be obtained from the author.

SIGNED: A. Evan Iverson

## DEDICATION

This dissertation is dedicated to my daughters, Michelle and Jennifer, and to my parents.

## ACKNOWLEDGMENTS

I acknowledge Dr. Darryl L. Smith for providing guidance for much of the work in this dissertation. I also acknowledge my advisor, Dr. Olgierd A. Palusinski, for his help and interest in this work.

## TABLE OF CONTENTS

	Page
LIST OF ILLUSTRATIONS .....	vii
ABSTRACT .....	x
1. INTRODUCTION .....	1
Applications of Photoconductors .....	3
The Time-dependent Response of Photoconductive Devices ...	5
2. GOVERNING EQUATIONS .....	10
Basic Semiconductor Device Equations .....	11
Maxwell's Equations .....	11
Continuity Equations .....	16
Boltzmann Transport and the Current Equations .....	20
Deep-level Impurities and Trapping Kinetics .....	26
Band Structure and Deep-level Trapping .....	27
Trapping Kinetics Modeling .....	31
3. NONLINEAR BULK MATERIAL RESPONSE RESULTING FROM DEEP-LEVEL TRAPPING .....	33
Introduction .....	33
Experimental Observations .....	35
Model Development and Results .....	40
Discussion and Conclusion .....	51
4. GENERATION-RECOMBINATION NOISE EFFECTS RESULTING FROM DEEP-LEVEL TRAPPING .....	57
Introduction .....	58
Theoretical Approach .....	61
Solution for the Green's Functions .....	73
Dependence on Trap Density and Temperature .....	79
Conclusion .....	92

TABLE OF CONTENTS — Continued

	Page
5. NONLINEAR, TIME-DEPENDENT PHOTOCONDUCTIVE DEVICE MODELING .....	95
Introduction .....	95
The Model Equations .....	99
The Numerical Solution Method .....	111
Computational Results .....	114
Experimental Observations of Overshoot .....	136
Conclusion .....	138
6. CONCLUSION .....	142
REFERENCES .....	151

## LIST OF ILLUSTRATIONS

	Page
Figure	
1.1 A generic semiconductor photoconductor in operation. ....	2
2.1 Band-to-band generation and recombination processes. ....	29
2.2 Deep-level trapping and emission processes. ....	30
3.1 Measured response, in arbitrary units, of an InP:Fe photoconductor to impulse excitation. ....	37
3.2 Measured response, in mV, of an InP:Fe photoconductor to 93-ns rectangular-pulse, laser-diode excitation. ....	39
3.3 Calculated response of an InP:Fe photoconductor to impulse excitation. ....	48
3.4 Calculated response of an InP:Fe photoconductor to 93-ns rectangular-pulse excitation. ....	50
4.1 A plot of the log of several carrier densities as a function of $100/T$ . ....	82
4.2 The function $\beta$ at low frequency as a function of $100/T$ for three values of the deep-level density ....	83
4.3 Responsivity at two values of the deep-level density as a function of the bias field. ....	85
4.4 The three noise voltage components and the total noise voltage as a function of the bias field. ....	87

LIST OF ILLUSTRATIONS — Continued

	Page
Figure	
4.5 A log plot of the three noise voltage components as a function of $100/T$ . . . . .	88
4.6 Detectivity for three values of the background photon flux as a function of the deep-level density . . . . .	91
4.7 A log-log plot of the three noise voltage components as a function of frequency. . . . .	93
5.1 Normalized total current density as a function of time for a 100- $\mu\text{m}$ -long photoconductor with 5-V bias. . . . .	119
5.2 Normalized excess electron density as a function of spatial position at four different times for the case $L = 100 \mu\text{m}$ and $V_o = 5 \text{ V}$ . . . . .	121
5.3 Normalized excess hole density as a function of spatial position at four different times for the case $L = 100 \mu\text{m}$ and $V_o = 5 \text{ V}$ . . . . .	123
5.4 Normalized excess negatively charged trap density as a function of spatial position at four different times for the case $L = 100 \mu\text{m}$ and $V_o = 5 \text{ V}$ . . . . .	125
5.5 Normalized electric field as a function of spatial position at four different times for the case $L = 100 \mu\text{m}$ and $V_o = 5 \text{ V}$ . . . . .	126
5.6 Normalized total current density as a function of time for a 100- $\mu\text{m}$ -long photoconductor with 1-V bias. . . . .	129

LIST OF ILLUSTRATIONS — Continued

	Page
Figure	
5.7 Normalized total current density as a function of time for a 100- $\mu\text{m}$ -long photoconductor with 25-V bias. ....	130
5.8 Normalized total current density as a function of time for a 1000- $\mu\text{m}$ -long photoconductor with 50-V bias. ....	132
5.9 Normalized total current density as a function of time for a 10- $\mu\text{m}$ -long photoconductor with 0.5-V bias. ....	133
5.10 Normalized total current density for double-pulse excitation as a function of time for a 100- $\mu\text{m}$ -long photoconductor with 5-V bias. ....	135
5.11 Experimental data showing overshoot behavior of the electron current component. ....	137

## ABSTRACT

This dissertation presents results pertaining to the mathematical modeling of semiconductor photoconductors and includes the formulation, analysis, and solution of photoconductive device model equations. The fundamental semiconductor device equations of continuity and transport are derived for the case of a material which contains a large density of deep-level impurities. Electron and hole trapping on deep-level impurities is accounted for by trapping-kinetics rate equations. The coupling between carrier drift and the electric field is completed through Poisson's equation.

Simple, nonlinear model equations are presented for bulk-material response based on the dynamics of electron and hole trapping and recombination on deep-level impurities. The characteristics of the solution to these model equations are observed to depend strongly on the excitation intensity. These model equations qualitatively reproduce observed experimental behavior of an iron-doped indium phosphide photoconductor.

A theory of the effect of deep-level centers on the generation-recombination noise and responsivity of an intrinsic photoconductor is presented. It is shown that the deep-level centers can influence the generation-

recombination noise and responsivity in three main ways: (i) they can shorten the bulk carrier lifetime by Shockley-Read-Hall recombination; (ii) for some values of the capture cross sections, deep-level densities, and temperature, the deep-level centers can trap a significant fraction of the photogenerated minority carriers. This trapping reduces the effective minority carrier mobility and diffusivity and thus reduces the effect of carrier sweep out on both generation noise and responsivity; (iii) the deep-level centers add a new thermal noise source, which results from fluctuations between bound and free carriers. The strength of this new noise source decreases with decreasing temperature at a slower rate than band-to-band thermal generation-recombination noise.

Photoconductive device model equations based on time-dependent, convective/diffusive transport equations are presented. The system of model equations is solved numerically with boundary conditions that represent ideal ohmic contacts. Computed results are presented for different photoconductor lengths and bias voltages with spatially uniform, rectangular light-pulse illumination.

## CHAPTER 1

### INTRODUCTION

Photoconductivity is an increase in the electrical conductivity of a material resulting from the absorption of radiation. A photoconductor is a two-terminal semiconductor device whose electrical conductivity is controlled by radiation absorbed by the device. The conductivity may be very low before the incidence of radiation and can be greatly increased by the absorption of radiation. The increase in electrical conductivity of a semiconductor photoconductor results from the generation of free (mobile) electrons and holes by the absorbed radiation energy (see figure 1.1). The negatively charged electrons and positively charged holes can move in the semiconductor under the influence of an applied electric field. The movement of the electrons and holes constitutes a flux and, since they are electrically charged, we speak in terms of an electrical current. The response of the photoconductor, i.e., the magnitude of the electrical current, is a function of the characteristics of the semiconductor material, the

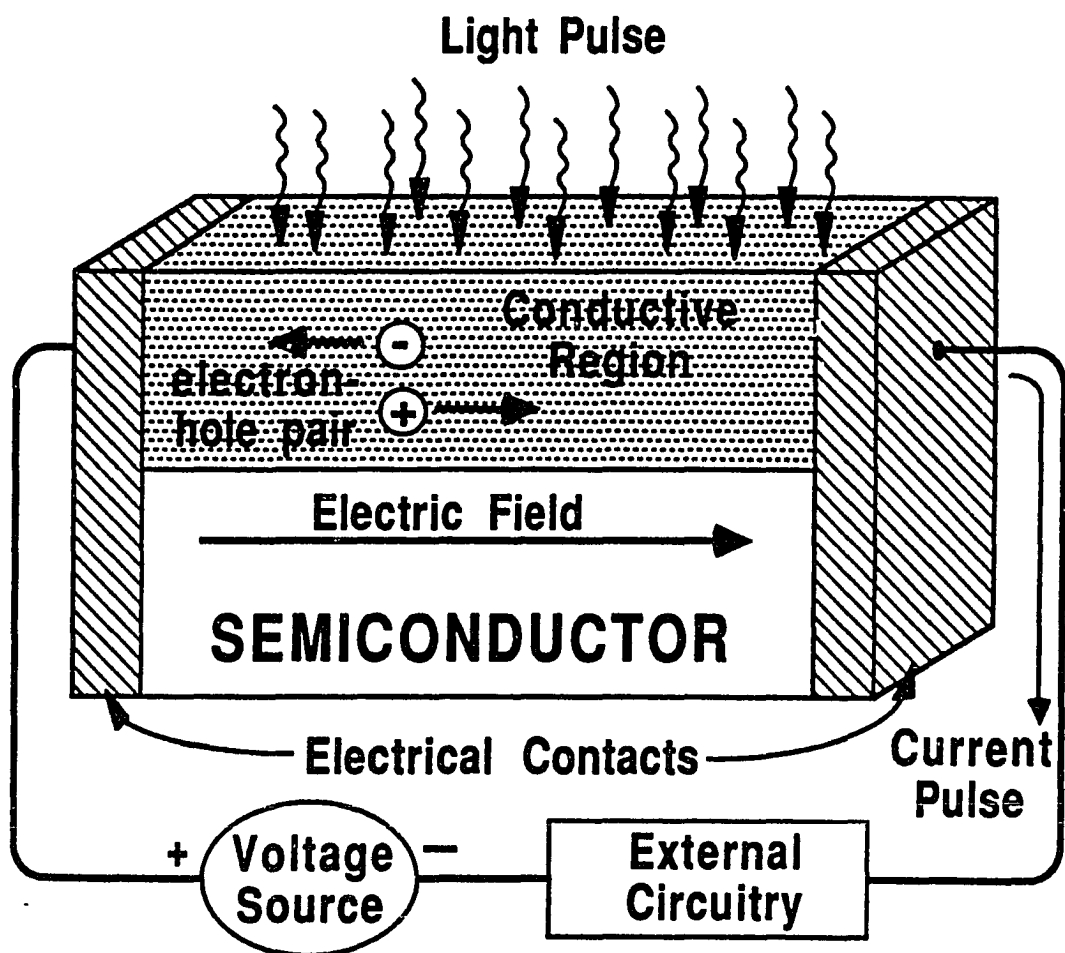


Figure 1.1: A generic semiconductor photoconductor in operation.

device construction, the device operating conditions, and the characteristics of the applied radiation. This dissertation presents results pertaining to the mathematical modeling of semiconductor photoconductors and includes the formulation, analysis, and solution of photoconductive device model equations.

### Applications of Photoconductors

The use of photoconductors is restricted to a somewhat limited range of applications. Photoconductors are not a common component in electronic engineering and the use of photoconductors is fairly specialized.

Perhaps the primary application of photoconductors is as photodetectors and radiation detectors. The source of excitation in these applications may be photons or ionizing radiation in the form of charged particles such as electrons or protons. The photoconductor may be used to detect either a single photon or a charged particle, or a flux of photons or particles. In most of these applications temporal information is required, therefore, the characteristics of the time-dependent (transient) response of the photoconductor are of interest. The time scale on which the incident excitation varies may range over many orders of magnitude depending on

---

the particular application. The response characteristics of the photoconductor over a wide range of intensity of the incident excitation are also of great importance.

A more recent application of photoconductors has been as electrical switching elements. These applications are closely coupled with the development of pulsed laser systems. On one end of the spectrum of these applications, photoconductors are used, along with lasers producing subpicosecond-wide pulses, in high-speed signal generation and sampling systems. The time resolution achievable using this measurement technique is many times greater than that obtainable using sampling techniques based on standard high-speed semiconductor devices. With this technique it is possible to do large-signal, transient characterization of microwave devices. At the other end of the spectrum, photoconductors are used, along with powerful nanosecond pulsed lasers, as high-voltage, high-power switches. The advantages of high speed and electrical isolation, compared to standard pulsed-power devices such as thyratrons, makes photoconductors a viable choice for certain advanced applications. In these applications the time-dependent response of the photoconductor is, again, of primary importance.

---

### The Time-dependent Response of Photoconductive Devices

The time-dependent response of a photoconductor is a function of the characteristics of the semiconductor material, the device construction, the device operating conditions, and the characteristics of the incident radiation.

Semiconductor materials used as photoconductors are generally chosen to have a high electrical resistivity so that the current composed of thermally generated electrons and holes under conditions of no incident radiation is relatively small. High resistivity semiconductors are often produced by doping the material with deep-level impurities. A deep-level impurity has an energy state that is near the middle of the semiconductors band gap and provides a mechanism by which the thermally generated electron and hole densities can be reduced. The mechanism is that a mobile electron or hole can be captured or trapped on a deep-level impurity with an appropriate charge state. This lowers the resistivity of the material and pins the Fermi energy level near the center of the band gap. These types of semiconductor materials are known as semi-insulating and are often used as photoconductors.

---

The deep-level impurities also capture electrons and holes produced by incident radiation. This process is a source of nonlinearity because the rate at which electrons and holes are captured on deep-level impurities is proportional to the product of the free carrier density and the density of appropriate deep-level impurities available to capture that carrier type. The presence of deep-level impurities gives the photoconductor a faster response decay time by reducing the mean carrier lifetime.

Deep-level impurity trapping and recombination processes will be discussed in more detail in the second section of chapter 2. A simple, nonlinear model of photoconductor response based on deep-level trapping is the subject of chapter 3, and the effects of deep-level centers on the generation-recombination noise and responsivity of intrinsic photoconductors is the subject of chapter 4.

The device construction is another factor in the response of a photoconductor. The device geometry and size may vary considerably depending on the particular application for which it is to be used. One common photoconductor geometry is that of a gap in a microstrip or coplanar transmission line constructed using a high-resistivity semiconductor material as the dielectric. This geometry is used in applications where high-speed

operation is critical, such as in picosecond pulse generation and sampling. Another geometry is that of a block of semiconductor material with the electrical contacts fabricated on opposing faces of the block. Photoconductors with this geometry may range in size from less than 1 mm on a side to greater than 1 cm on a side.

The properties of the electrical contacts are another factor of the device construction which has an effect on photoconductor transient response. Very little is understood about the characteristics of semiconductor electrical contacts. For the work presented in this dissertation, the electrical contacts will be assumed to be ohmic and to have an infinite surface recombination velocity.

The operating conditions of a photoconductor are determined by the applied bias voltage and the characteristics of the external circuit in which the photoconductor operates. For most applications, the external circuit can be assumed to be resistive and constant. Two basic types of operation can be defined based on the relative value of the minimum electrical impedance which the photoconductor obtains under illumination and the impedance of the external circuit. If the photoconductors impedance always remains much greater than that of the external circuit impedance,

the bias voltage applied to the photoconductor can be assumed to remain constant. This is the case for most detector and sampling applications. If the photoconductor impedance becomes comparable to or less than the circuit impedance, such as in a switching application, then the bias voltage applied to the photoconductor will vary in time as a function of the total current and the circuit impedance. The results presented in this dissertation are for the case of relatively high photoconductor impedance, thus, constant bias voltage is assumed. The ratio of the applied bias voltage to the length of the photoconductor is an important parameter in that it gives the equilibrium electrical field strength in the photoconductor. The force on an electron or hole is proportional to the strength of the electric field and, therefore, the convective (drift) component of the current will be greater for a stronger electric field.

The type of radiation incident on the photoconductor influences the response by the way in which it is absorbed by the semiconductor material. The absorption of photons or ionizing particles creates electrons and holes in pairs with the number of electron-hole pairs produced depending on the intensity and energy of the radiation. The absorption of radiation is characterized by an absorption length which assumes an

exponential absorption profile of the radiation in the material. For visible light the absorption length is generally quite short (on the order of  $1 \mu\text{m}$ ) and, therefore, the electron-hole pairs are produced in a relatively small volume near the surface of the photoconductor. High-energy photons and particles penetrate much deeper into the material producing bulk excitation. For the case of surface absorption, the characteristics of the surface of the semiconductor may have an effect on the response of the device. Surface effects are inherently quite complicated and, for the work presented in this dissertation, it will be assumed that the photoconductor is bulk excited and surface effects can be neglected.

The development of photoconductive device model equations which include the characteristics of the semiconductor material, the device construction, the device operating conditions, and the characteristics of the incident radiation is the subject of chapter 2. The solution of this system of time-dependent partial differential equations for a variety of cases is the subject of chapter 5.

---

## CHAPTER 2

### GOVERNING EQUATIONS

In this chapter time-dependent semiconductor device equations of continuity, transport, carrier interaction with deep-level impurities, and electric potential dependency are derived. From Maxwell's equations, continuity equations are derived for electron, hole, and deep-level charge state densities. Poisson's equation, which relates the dependency of the electric field on space charge, is also derived from Maxwell's equations. A reduction of the Boltzmann transport equation yields the current relations for electrons and holes in a semiconductor. A discussion of the kinetics of carrier trapping on deep-level impurities, an important process in many photoconductors, is presented and model equations for this process are given. The resulting system of nonlinearly coupled partial differential equations describes the electrodynamic behavior of semiconductor devices in terms of carrier densities, deep-level charge state densities, and electric potential.

Basic Semiconductor Device Equations

Maxwell's Equations

Maxwell's equations describe the evolution of electromagnetic field quantities and can be written in MKS rationalized units as:

$$\nabla \times \mathbf{H} = \mathbf{J} + \frac{\partial \mathbf{D}}{\partial t}, \quad (2.1)$$

$$\nabla \times \mathbf{E} + \frac{\partial \mathbf{B}}{\partial t} = 0, \quad (2.2)$$

$$\nabla \cdot \mathbf{D} = \rho, \quad (2.3)$$

$$\nabla \cdot \mathbf{B} = 0, \quad (2.4)$$

where  $\mathbf{E}$  and  $\mathbf{D}$  are the electric field and displacement vectors,  $\mathbf{H}$  and  $\mathbf{B}$  are the magnetic field and induction vectors,  $\mathbf{J}$  is the conduction current density, and  $\rho$  is the electric charge density. Equation (2.1) is Amperes's law to which Maxwell added the displacement term  $\frac{\partial \mathbf{D}}{\partial t}$  which is required to make the system of equations consistent. Equation (2.2) is Faraday's law, equation (2.3) is Coulomb's law, and equation (2.4) states the absence of magnetic monopoles. For macroscopic media, the dynamical response of the aggregate atoms is summarized in the constitutive relations which

connect  $\mathbf{D}$  and  $\mathbf{J}$  with  $\mathbf{E}$  and  $\mathbf{H}$  with  $\mathbf{B}$ .

$$\mathbf{D} = \epsilon \mathbf{E} \quad (2.5)$$

$$\mathbf{J} = \sigma \mathbf{E} \quad (2.6)$$

$$\mathbf{B} = \mu \mathbf{H} \quad (2.7)$$

The permittivity  $\epsilon$ , conductivity  $\sigma$ , and permeability  $\mu$  are, in general, tensors, but for semiconductors which are isotropic, permeable, and conducting they reduce to scalar parameters.

Maxwell's equations consist of a set of four, coupled, first-order partial differential equations relating the various components of electric and magnetic fields. It is useful to introduce two potentials which allow these four first-order equations to be written as two second-order equations. These potentials are the scalar electric potential  $\psi$  and the magnet vector potential  $\mathbf{A}$ . Since  $\nabla \cdot \mathbf{B} = 0$ ,  $\mathbf{B}$  can be defined in terms of a vector potential  $\mathbf{A}$  as

$$\mathbf{B} = \nabla \times \mathbf{A}. \quad (2.8)$$

Faraday's law (2.2) can then be written as

$$\nabla \times \left[ \mathbf{E} + \frac{\partial \mathbf{A}}{\partial t} \right] = 0. \quad (2.9)$$

This means that the quantity with the vanishing curl in equation (2.9) can be written as the gradient of some scalar function, namely, the scalar electric potential  $\psi$ .

$$\mathbf{E} + \frac{\partial \mathbf{A}}{\partial t} = -\nabla \psi \quad (2.10)$$

or

$$\mathbf{E} = -\nabla \psi - \frac{\partial \mathbf{A}}{\partial t} \quad (2.11)$$

The definition of  $\mathbf{B}$  and  $\mathbf{E}$  in terms of the potentials  $\mathbf{A}$  and  $\psi$  according to equations (2.8) and (2.11) satisfies identically the two homogeneous Maxwell's equations. The two inhomogeneous equations determine the dynamic behavior of  $\mathbf{A}$  and  $\psi$ . Writing these two inhomogeneous equations in terms of  $\mathbf{A}$  and  $\psi$  we get

$$\nabla^2 \mathbf{A} - \epsilon \mu \frac{\partial^2 \mathbf{A}}{\partial t^2} - \nabla \left[ \nabla \cdot \mathbf{A} + \epsilon \mu \frac{\partial \psi}{\partial t} \right] = -\mu \mathbf{J} \quad (2.12)$$

and

$$\nabla^2 \psi + \frac{\partial}{\partial t} \nabla \cdot \mathbf{A} = -\frac{1}{\epsilon} \rho. \quad (2.13)$$

The set of four Maxwell's equations has been reduced to a set of two coupled equations, (2.12) and (2.13), by introducing the potentials  $\mathbf{A}$  and  $\psi$ . These equations can be uncoupled by exploiting the fact that an arbitrary factor can be added to the definition of the potentials. For the

definition of  $\mathbf{B}$  in terms of  $\mathbf{A}$ , the choice of  $\mathbf{A}$  is arbitrary in that the gradient of some scalar function  $\zeta$  can be added. Thus the definition of  $\mathbf{B}$  is left unchanged by the transformation

$$\mathbf{A} \longrightarrow \mathbf{A} + \nabla\zeta. \quad (2.14)$$

In order that the definition of the electric field  $\mathbf{E}$  remain unchanged, the simultaneous transformation

$$\psi \longrightarrow \psi - \frac{\partial\zeta}{\partial t} \quad (2.15)$$

is made. The potentials  $\mathbf{A}$  and  $\psi$  are now free to be chosen such that

$$\nabla \cdot \mathbf{A} + \epsilon\mu \frac{\partial\psi}{\partial t} = 0. \quad (2.16)$$

This uncouples equations (2.12) and (2.13) which can then be written as

$$\nabla^2 \mathbf{A} - \epsilon\mu \frac{\partial^2 \mathbf{A}}{\partial t^2} = -\mu \mathbf{J} \quad (2.17)$$

and

$$\nabla^2 \psi - \epsilon\mu \frac{\partial^2 \psi}{\partial t^2} = -\frac{1}{\epsilon} \rho. \quad (2.18)$$

This set of two, uncoupled, second-order equations, along with equation (2.16), is equivalent to the four Maxwell's equations in every respect. These equations are hyperbolic and exemplify the propagating nature of electromagnetic disturbances. The quantity  $\epsilon\mu$  is related to the

velocity of propagation  $U$  of electromagnetic radiation by the equation

$$U = \frac{1}{\sqrt{\epsilon\mu}}. \quad (2.19)$$

The electric permittivity  $\epsilon$  and the magnetic permeability  $\mu$  are written in terms of their free space values,  $\epsilon_o$  and  $\mu_o$ , times their values relative to free space,  $\epsilon_r$  and  $\mu_r$ , as

$$\epsilon = \epsilon_r \epsilon_o \quad (2.20)$$

and

$$\mu = \mu_r \mu_o. \quad (2.21)$$

The value of the free space permittivity is  $\epsilon_o = 8.845 \times 10^{-14}$  F/cm and the value of the free space permeability is  $\mu_o = 4\pi \times 10^{-9}$  H/cm. The velocity of propagation can then be written as

$$U = \frac{1}{\sqrt{\epsilon_r \mu_r}} \frac{1}{c}, \quad (2.22)$$

where  $c = 1/\sqrt{\epsilon_o \mu_o}$  is the velocity of light in free space. For semiconductors the relative permittivity or dielectric constant  $\epsilon_r$  is on the order of 10 and the relative permeability  $\mu_r$  is very close to 1 so that electromagnetic disturbances travel at  $\sim \frac{1}{3}$  the velocity of light.

Equation (2.18) is recognized as being the complete form of Poisson's equation. For most semiconductor devices the time scale on which

the device operates is much longer than the time that it takes an electromagnetic disturbance to travel the length of the device. This allows the second-order time derivative term in equation (2.18) to be neglected giving the elliptic form of Poisson's equation which will be used in modeling photoconductive devices.

$$\nabla^2\psi = -\frac{1}{\epsilon}\rho \quad (2.23)$$

### Continuity Equations

The continuity equations for electrons and holes can be derived directly from the first Maxwell equation (2.1). Applying the divergence operator to this equation gives

$$\nabla \cdot (\nabla \times \mathbf{H}) = \nabla \cdot \mathbf{J} + \frac{\partial \rho}{\partial t} = 0. \quad (2.24)$$

In a semiconductor the conduction current  $\mathbf{J}$  results from the flow of electrons and holes and can be written as the sum of an electron component  $\mathbf{J}_n$  and a hole component  $\mathbf{J}_p$ .

$$\mathbf{J} = \mathbf{J}_n + \mathbf{J}_p \quad (2.25)$$

The charge density  $\rho$ , however, depends not only on the mobile electrons and holes, but on the charge states of any impurities or other sites in the

crystal lattice which may develop a charge state by ionization or by capturing or trapping mobile electrons and holes. If we assume for a moment that there are no other charged species present other than electrons and holes, the charge density  $\rho$  can be written as

$$\rho(\mathbf{r}, t) = q[p(\mathbf{r}, t) - n(\mathbf{r}, t)], \quad (2.26)$$

where  $q = 1.602 \times 10^{-19} \text{ C}$  is the electronic charge,  $p(\mathbf{r}, t)$  is the density of holes and  $n(\mathbf{r}, t)$  is the density of electrons. Equation (2.24) can then be written as

$$\frac{\partial}{\partial t}(p - n) = -\frac{1}{q} \nabla \cdot (\mathbf{J}_n - \mathbf{J}_p). \quad (2.27)$$

This equation of continuity relates the sources and sinks of the total conduction current to the time variation of the mobile charge. The goal is to obtain a separate continuity equation for the electron and hole densities. In a photoconductor electrons and holes are generated in pairs by the excitation which leads to the introduction of an electron-hole-pair generation term  $G(\mathbf{r}, t)$ . Electron-hole pair reduction can also occur through a process known as band-to-band recombination which is written as  $R_B(\mathbf{r}, t)$ . The splitting of equation (2.27) can now be accomplished using these two

presently undefined functions.

$$\frac{\partial n}{\partial t} = G - R_B + \frac{1}{q} \nabla \cdot \mathbf{J}_n \quad (2.28)$$

$$\frac{\partial p}{\partial t} = G - R_B - \frac{1}{q} \nabla \cdot \mathbf{J}_p \quad (2.29)$$

No new information is gained by writing equation (2.27) as two separate equations, but it does lead to some insight into the relationship of electrons and holes. The quantity  $(G - R_B)$  is seen to be a function representing the generation and recombination of electrons and holes in pairs. The function  $G(\mathbf{r}, t)$  which represents the generation of electron-hole pairs by the excitation applied to the photoconductor is easily understood in terms of the absorption of the excitation radiation in the semiconductor. (A small density of electron-hole pairs is also produced thermally.) The function  $R_B(\mathbf{r}, t)$ , which represents electron and hole recombination in pairs, requires knowledge of the physics of semiconductors in order to be defined.

For the case of charge trapping, which is commonly important in the materials used as photoconductors, equations of continuity are required for the various types of trapping sites in the material. In order to illustrate the formulation of these required equations, the simple case of a single type of charge trapping site which can exist in either a neutral or a negative

charge state is considered. A site which has a neutral charge state can capture (trap) an electron thereby becoming negatively charged, and a site in a negatively charged state can capture a hole and become neutral. The inverse process of thermal emission of an electron or hole from a deep-level also exists. In most cases this process will be insignificant, so terms representing this process are not included in the governing equations presented here.

We will represent the density of neutrally charged trapping sites as  $n_T^o(\mathbf{r}, t)$  and the density of negatively charged trapping sites as  $n_T^-(\mathbf{r}, t)$ . Because the trapping sites themselves are nonmobile and are always considered to remain active, the two charge state densities are related by

$$n_T^o(\mathbf{r}, t) + n_T^-(\mathbf{r}, t) = N_T, \quad (2.30)$$

where  $N_T$  is the total density of trapping sites.  $N_T$  does not vary with time and will be assumed to be spatial uniform. Because  $n_T^o$  and  $n_T^-$  are related by the constant  $N_T$ , only a single continuity equation is required to account for the trapping dynamics. Choosing  $n_T^-$  as the variable in which to write this continuity equation gives

$$\rho(\mathbf{r}, t) = q[p(\mathbf{r}, t) - n(\mathbf{r}, t) - n_T^-(\mathbf{r}, t)]. \quad (2.31)$$

Equation (2.24) can then be written as three separate continuity equations.

$$\frac{\partial n}{\partial t} = G - R_B - R_n + \frac{1}{q} \nabla \cdot \mathbf{J}_n \quad (2.32)$$

$$\frac{\partial p}{\partial t} = G - R_B - R_p - \frac{1}{q} \nabla \cdot \mathbf{J}_p \quad (2.33)$$

$$\frac{\partial n_T^-}{\partial t} = R_n - R_p \quad (2.34)$$

The function  $R_n(\mathbf{r}, t)$  accounts for the trapping of electrons on neutrally charged sites and the function  $R_p(\mathbf{r}, t)$  accounts for the trapping of holes on negatively charged sites. These functions are, as yet, undefined and will be discussed in detail in the section of this chapter on deep-level impurities and trapping kinetics.

### Boltzmann Transport and the Current Equations

To complete the system of equations which are used in semiconductor device modeling, equations relating the electron and hole currents to the carrier densities and electric field are required. These equations are derived from transport theory based on the Boltzmann transport equation. The considerations necessary to derive the current equations in detail are based on an extremely wide range of physics which will not be presented here. In this section only a superficial derivation of the current equations will be presented.

For the purpose of analysis, a semiconductor can be thought of as consisting of three interacting components: the crystal lattice structure and two fluids. One fluid consists of the conduction band electrons, and the other consists of the valence band holes. The quantum theory of transport would be used to describe this system from first principles, but this approach would not yield macroscopic model equations. A semiclassical, statistical approach is employed to describe the behavior of conduction band electrons and valence band holes where quantum effects are accounted for by phenomenological macroscopic models. Because electrons and holes in a semiconductor are dual particles, the derivation of the current equations will be presented only for the conduction band electrons. The derivation of the valence band hole current equation would follow in an analogous manner.

A complete description of the evolution of a system of particles in time under the action of forces is given by the Liouville equation. The Boltzmann equation, which gives a semiclassical description in terms of a distribution function, has proven to be the most useful in the study of transport processes. The Boltzmann equation is an integro-differential equation in seven independent variables: the position vector  $r$ ,

the momentum vector  $\mathbf{k}$ , and time  $t$ . It can be written for conduction band electrons as

$$\frac{Df^c}{Dt} = C^c[f^c], \quad (2.35)$$

where  $f^c(\mathbf{r}, \mathbf{k}, t)$  is the conduction band electron distribution function,  $D/Dt$  is the convective derivative, and  $C^c[f^c]$  represents the conduction band electron collision integral. The collision integral will, in general, contain many terms each accounting for one of the various collision processes that a particle can participate in, such as scattering by a phonon. The convective derivative can be expanded as

$$\frac{Df^c}{Dt} = \frac{\partial f^c}{\partial t} + \frac{\partial \mathbf{r}}{\partial t} \frac{\partial f^c}{\partial \mathbf{r}} + \frac{\partial \mathbf{k}}{\partial t} \frac{\partial f^c}{\partial \mathbf{k}}. \quad (2.36)$$

The time rate of change of position and momentum are known to be

$$\frac{\partial \mathbf{r}}{\partial t} = \mathbf{v}_n \quad (2.37)$$

and

$$\frac{\partial \mathbf{k}}{\partial t} = \frac{\mathbf{F}_n}{\hbar}, \quad (2.38)$$

where  $\mathbf{v}_n$  is the electron group velocity,  $\mathbf{F}_n$  is the external force on the electron, and  $\hbar = 1.055 \times 10^{-34}$  J-sec is Plank's constant divided by  $2\pi$ .

The collision integral accounts for the internal forces resulting from collision processes. Using the relaxation time approximation, the collision integral is written as

$$C^c[f^c] = -\frac{f^c - f_o^c}{\tau_n}, \quad (2.39)$$

where  $f_o^c$  is the thermal-equilibrium distribution function and  $\tau_n$  is the time constant for the return to equilibrium of a perturbed distribution function. Using relations (2.37) and (2.38) and the relaxation time approximation (2.39), the Boltzmann transport equation is written as

$$\frac{\partial f^c}{\partial t} = -\mathbf{v}_n \cdot \frac{\partial f^c}{\partial \mathbf{r}} - \frac{\mathbf{F}_n}{\hbar} \cdot \frac{\partial f^c}{\partial \mathbf{k}} - \frac{f^c - f_o^c}{\tau_n}. \quad (2.40)$$

The Boltzmann transport equation is then multiplied by  $\mathbf{v}_n$  and integrated over the Brillouin zone in momentum space. The resulting four integrals are well known and are presented here without derivation as

$$\int_{BZ} \mathbf{v}_n \cdot \frac{\partial f^c}{\partial t} \cdot d\mathbf{k} = 4\pi^3 \frac{\partial}{\partial t} (n\mathbf{v}_n), \quad (2.41)$$

$$\int_{BZ} \mathbf{v}_n \cdot \left( \mathbf{v}_n \frac{\partial f^c}{\partial \mathbf{r}} \right) \cdot d\mathbf{k} = 4\pi^3 \frac{1}{m_n^*} \frac{\partial}{\partial \mathbf{r}} (k_B n T_L), \quad (2.42)$$

$$\int_{BZ} \mathbf{v}_n \cdot \left( \frac{\mathbf{F}_n}{\hbar} \frac{\partial f^c}{\partial \mathbf{k}} \right) \cdot d\mathbf{k} = -4\pi^3 \frac{1}{m_n^*} \mathbf{F}_n n, \quad (2.43)$$

$$\int_{BZ} \mathbf{v}_n \cdot \left( \frac{f^c - f_o^c}{\tau_n} \right) \cdot d\mathbf{k} = 4\pi^3 \frac{1}{\tau_n} n\mathbf{v}_n, \quad (2.44)$$

where  $n(\mathbf{r}, t)$  is the electron density,  $m_n^*$  is the electron effective mass,  $k_B$  is

Boltzmann's constant, and  $T_L$  is the lattice temperature. The Boltzmann transport equation after the integration can then be written as

$$\frac{\partial}{\partial t} (n\mathbf{v}_n) = -\frac{1}{m_n^*} \nabla (k_B n T_L) + \frac{1}{m_n^*} \mathbf{F}_n n - \frac{1}{\tau_n} n \mathbf{v}_n. \quad (2.45)$$

This equation is a macroscopic force balance equation.

The external force  $\mathbf{F}_n$  results from electromagnetic effects on the negatively charged electrons. If the Lorentz force proportional to the magnetic induction  $\mathbf{B}$  is neglected,  $\mathbf{F}_n$  can be written in terms of the electric field  $\mathbf{E}$  as

$$\mathbf{F}_n = -q\mathbf{E}. \quad (2.46)$$

The goal of this derivation is to find an expression which relates the electron current to the electron density and the electric field. The electron current can, in general, be written as the product of the electronic charge, the electron density, and the average electron velocity.

$$\mathbf{J}_n = -qn\mathbf{v}_n \quad (2.47)$$

An effective electron mobility  $\mu_n$  is defined as

$$\mu_n = \frac{q\tau_n}{m_n^*}. \quad (2.48)$$

Multiplying equation (2.45) by  $q\tau_n$  and making use of equations (2.46), (2.47), and (2.48) gives

$$\tau_n \frac{\partial}{\partial t} \mathbf{J}_n + \mathbf{J}_n = q\mu_n \mathbf{E}n + \mu_n \nabla(k_B T_L n). \quad (2.49)$$

The average collision time  $\tau_n$  is very small, typically less than one picosecond. Equation (2.49) can therefore be thought of as being singularly perturbed in time. It is natural to consider a solution based on an expansion in terms of powers of the perturbation parameter  $\tau_n$ . Keeping only the zeroth order term of the expansion gives

$$\mathbf{J}_n \approx q\mu_n \mathbf{E}n + \mu_n \nabla(k_B T_L n). \quad (2.50)$$

This equation is a formal approximation of order  $\tau_n$ .

It is further assumed that the lattice temperature  $T_L$  is constant and that the Einstein relation

$$D_n = \frac{k_B T_L}{q} \mu_n \quad (2.51)$$

is valid to define the diffusion coefficient  $D_n$ . This gives the final result for the electron current in terms of the sum of a drift component and a diffusion component.

$$\mathbf{J}_n = q\mu_n \mathbf{E}n + qD_n \nabla n \quad (2.52)$$

In an analogous manner, an expression for the hole current is found to be

$$\mathbf{J}_p = q\mu_p \mathbf{E}p - qD_p \nabla p. \quad (2.53)$$

### Deep-level Impurities and Trapping Kinetics

The system of semiconductor device governing equations derived in the first section of this chapter can be thought of as consisting of four components. The first, and main, component is comprised of the equations of continuity which are written in terms of the density of the dynamically variable charged species. The continuity equations contain terms for the generation and reduction of the densities of the species and, if the species are mobile, a term for transport. Secondly, there are the current transport equations for the mobile electrons and holes which define the flux (current) in terms of the densities. The third component of the governing equations is Poisson's equation which relates the electric potential and the electric field (the driving force behind the convective component of the flux) to the spatial distribution of the charged species. This is an important source of coupling in the system of equations. The final component of the governing equations is that of relations describing the generation and reduction of electrons and holes. These relations further couple the system of continuity

---

equations. The photogeneration of electron-hole pairs is defined in terms of the characteristics of the absorption of the incident excitation by the photoconductor. The reduction of electron and hole densities through the trapping process is the subject of this section.

### Band Structure and Deep-level Trapping

In discussing the generation and reduction of electron and hole densities, it is useful to consider a simple valence and conduction band diagram. This diagram relates electron and hole interactions with energy transitions. In this diagram, energy is plotted on the vertical axis. The horizontal axis can represent spatial position, but this is not important for the purposes of this discussion.

The generation of electron-hole pairs (referred to as a band-to-band process) by thermal or photo-induced processes is driven by the transfer of sufficient energy (greater than the bandgap energy) from a phonon or photon to a nonmobile valence band electron causing it to undergo an energy transition to the conduction band where it is mobile. A mobile hole is simultaneously generated in the valence band. This hole can be thought of as a quasiparticle representing the vacancy produced by the

electron transition from the valence band to the conduction band. The inverse process, that of band-to-band recombination, is represented as a transition in the opposite sense and is accompanied by a release of energy. These processes are shown in figure 2.1. The thermal band-to-band generation process and the band-to-band recombination process proceed at the same rate when the semiconductor material is in thermal equilibrium. This thermodynamic law is referred to as detailed balance. It is important to remember that the equations are written in terms of the mobile conduction band electrons and the mobile valence band holes.

A deep-level impurity is represented as having an energy state near the center of the bandgap. Transitions of electrons or holes to and from a deep-level energy state are dependent on the charge state of the deep-level site. Both thermal emission of electrons or holes from deep levels and trapping of electrons or holes on deep levels are possible. The possible transitions for the case of a deep-level site which can exist in only the negative or neutral charge states are shown in figure 2.2. The law of detailed balance applies and, at thermal equilibrium, each process and its inverse proceed at the same rate.

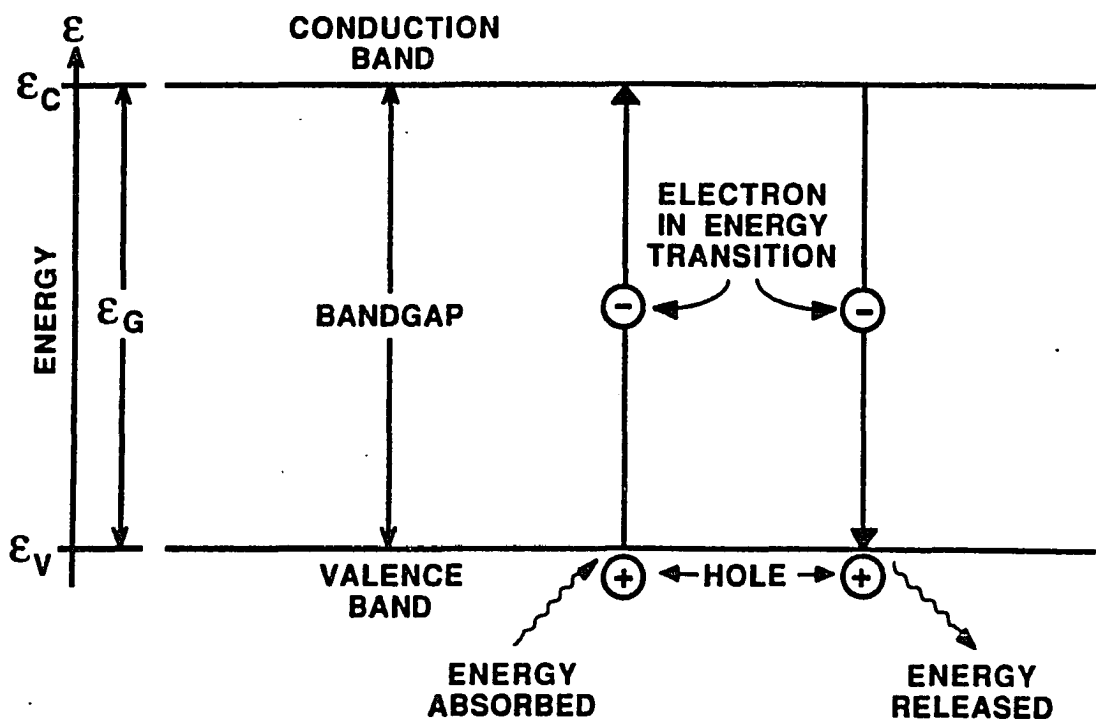


Figure 2.1: Band-to-band generation and recombination processes.

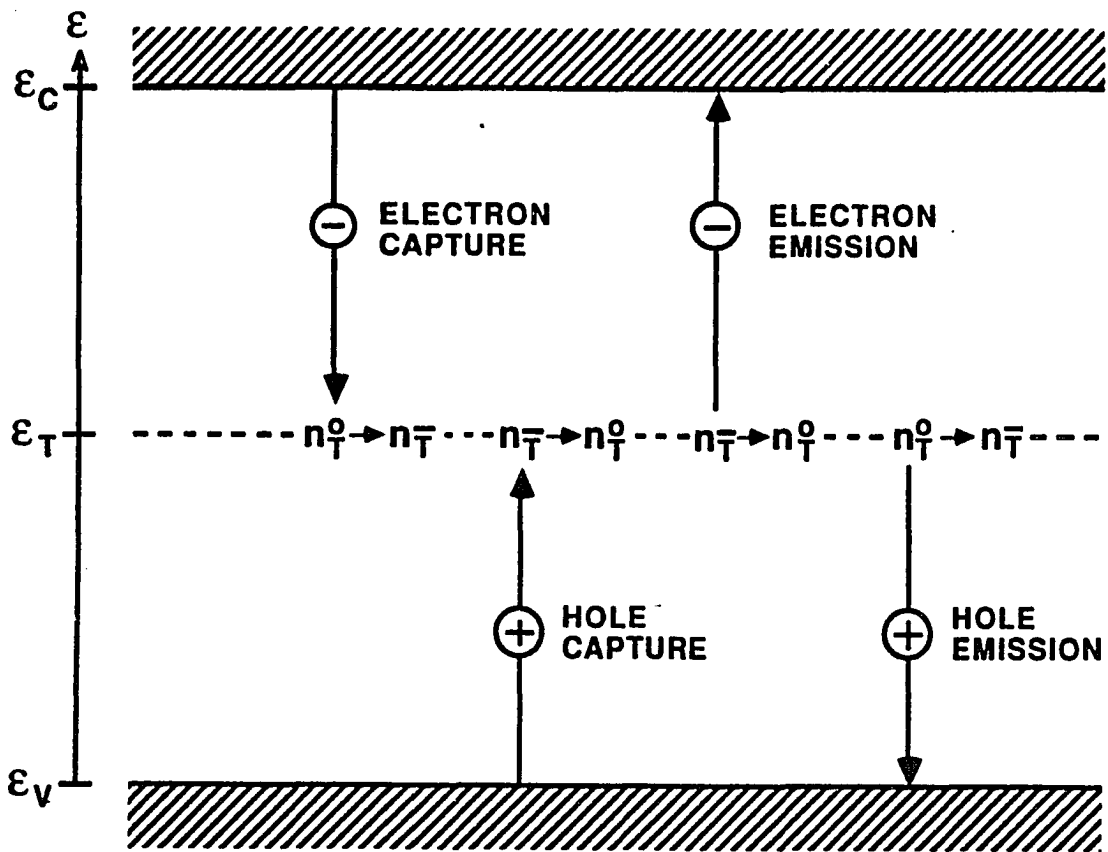


Figure 2.2: Deep-level trapping and emission processes.

### Trapping Kinetics Modeling

Expressions relating the rate functions  $R_n$  and  $R_p$  to the various densities are required to complete the derivation of the system of governing equations. As is the case in many dynamical systems, the rates are assumed to be proportional to the product of the density of species available to make the transition and the density of sites available to accept these species. Using this common idea, the rate functions are written as

$$R_n = B_n n n_T^o \quad (2.54)$$

and

$$R_p = B_p p n_T^- \quad (2.55)$$

for the case of deep levels which can exist in either a neutral or negative charge state. The rate constants  $B_n$  and  $B_p$  can further be defined in terms of physical characteristics of the species making the transition and the deep level as

$$B_n = \langle v_n \rangle \sigma_n, \quad (2.56)$$

$$B_p = \langle v_p \rangle \sigma_p. \quad (2.57)$$

Here  $\langle v_n \rangle$  and  $\langle v_p \rangle$  are the electron and hole thermal velocities, and  $\sigma_n$  and  $\sigma_p$  are the electron and hole capture cross sections on a deep-

level trapping site. The rate functions for the inverse process of thermal emission from a deep level and for band-to-band recombination can be written in a similar manner. The process of trapping of electrons and holes on deep levels is sometimes referred to as trap assisted recombination or as Schockley-Read-Hall recombination.

## CHAPTER 3

### NONLINEAR BULK MATERIAL RESPONSE RESULTING FROM DEEP-LEVEL TRAPPING

In this chapter experimental transient response data for iron-doped indium phosphide (InP:Fe) photoconductors subject to impulse and rectangular-pulse excitation over a wide range of intensities is presented. The photoconductor temporal response is observed to depend strongly on the excitation intensity. A model for bulk-material response based on the dynamics of electron and hole trapping and recombination on the deep-level iron impurities is presented. The model qualitatively reproduces the observed experimental behavior.

#### Introduction

A material of interest for photoconductive applications is iron-doped indium phosphide (InP:Fe). The iron in indium phosphide is a deep acceptor and provides a mechanism by which free electrons and holes can

recombine. The presence of this trapping mechanism reduces the characteristic lifetime of the photogenerated carriers, thereby giving the material a faster response time than if the iron impurities were not present. The iron can also pin the Fermi energy level near the center of the band gap causing the material to be semi-insulating.

In this chapter, experimentally observed transient response characteristics of InP:Fe photoconductors are presented. A simple model of the bulk-material transient photoconductive response for InP:Fe based on the trapping and recombination of electrons and holes on the iron sites is developed. The characteristics of this bulk-material-response model are compared with the experimentally observed behavior and qualitative agreement between the model and the observations is found.

The chapter is organized as follows: in the second section, experimental observations of the transient response of InP:Fe photoconductors are presented; the third section contains the development of the model equations and computational results based on these equations; and in the fourth section, the ability of the model equations to describe the experimentally observed behavior is discussed.

### Experimental Observations

Semi-insulating, iron-doped indium phosphide was used for the experimental observations reported here. The material had a homogeneous iron concentration of  $\sim 10^{16}\text{cm}^{-3}$ . Iron in indium phosphide is an acceptor-like (charge states 0 and -1) impurity with a single energy level located near the middle of the band gap [3.1, 3.2, 3.3]. The material was semi-insulating (resistivity  $\gg 10^7\Omega\text{cm}$ ) because the iron compensates residual shallow donors causing the Fermi energy level to be pinned near the iron energy level at midgap.

Photoconductors were fabricated from (110) oriented, semi-insulating InP:Fe wafers. Evaporated and annealed AuGeNi contact metalizations were made on 1- by 5- by 0.3-mm<sup>3</sup> pieces cut from the wafers. Photoconductors were constructed with 25- and 580- $\mu\text{m}$  lengths defined by the contact spacing. These photoconductors were inserted in place of a 5-mm section of a 50- $\Omega$  microstrip transmission line fabricated on a 1-mm-thick alumina substrate.

Impulse response measurements on these photoconductors were made using 15-ps, 780-nm-wavelength laser pulses and 50-ps, 6-MeV electron-

beam pulses. The top panel in figure 3.1 shows the impulse response of a 25- $\mu\text{m}$ -gap device biased at 20 V and excited with 15-ps laser pulses. The optical pulse energy on the device was 590 pJ, which produced an electron-hole pair density of  $\sim 10^{18}\text{cm}^{-3}$ . The response decay is seen to be nearly exponential with a time constant of 950 ps. The bottom panel in figure 3.1 shows the impulse response of a 580- $\mu\text{m}$ -gap device biased at 500 V and excited with 50-ps electron-beam pulses. An electron-hole pair density of  $\sim 10^{12}\text{cm}^{-3}$  was generated by the electron-beam excitation. The response decay is seen to be nearly exponential with a time constant of 630 ps.

The carrier densities generated in the experiments yielding the two curves in figure 3.1 differed by approximately six orders of magnitude. For laser excitation, the photogenerated carrier density far exceeded the iron concentration; whereas, for the electron-beam excitation, the carrier density was orders of magnitude less than the iron concentration. In both cases, the signals decayed exponentially. For the high-intensity laser excitation, the decay time constant was about 50% larger than the low-intensity electron-beam excitation decay time constant. The increase in response time with higher-intensity excitation is very systematic and was observed in a large number of InP:Fe samples.

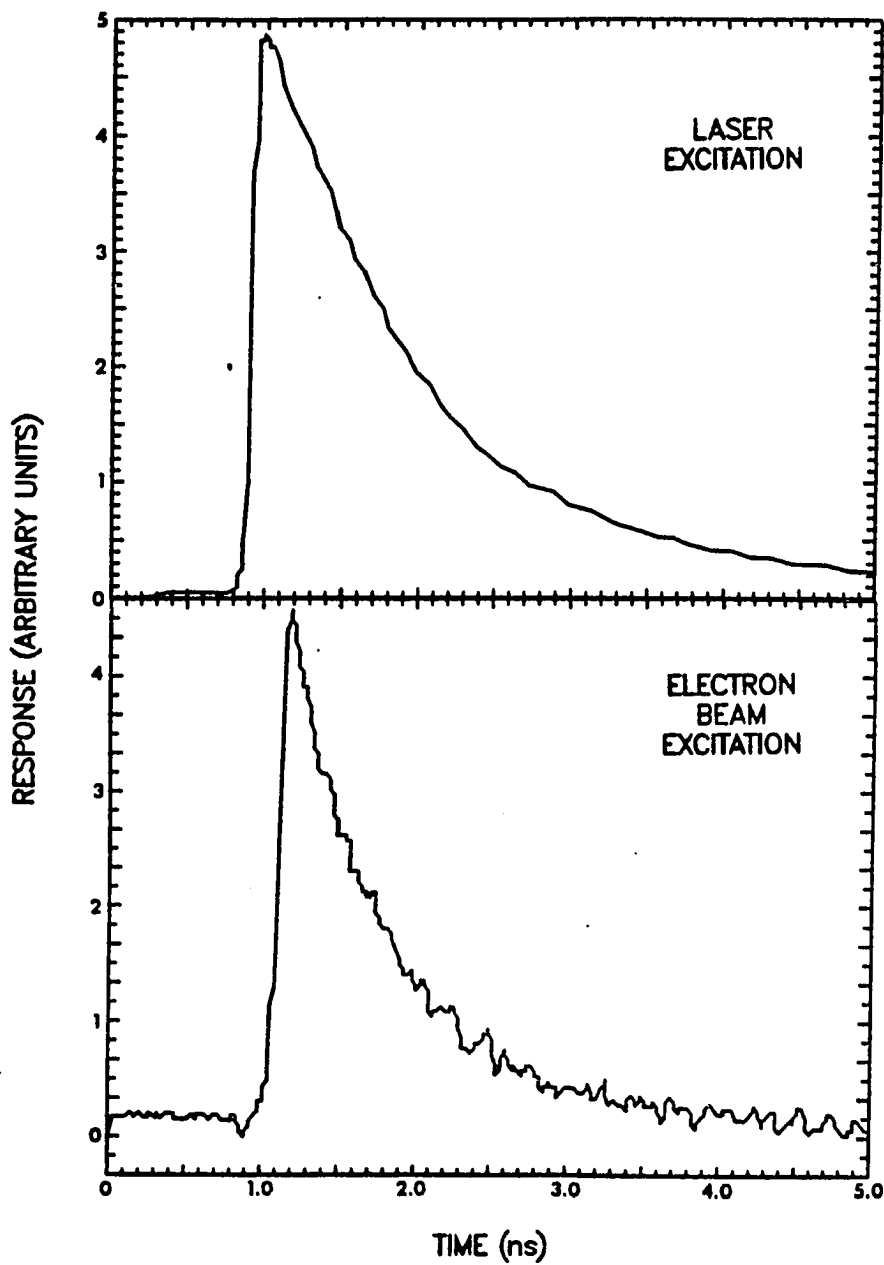


Figure 3.1: Measured response, in arbitrary units, of an InP:Fe photoconductor to impulse excitation.

The response of InP:Fe photoconductors to 93-ns-wide, rectangular light pulses was measured. The light pulses were generated using a single-mode injection laser diode mounted in a transmission line geometry. The 3-mW, 835-nm wavelength pulses from the laser diode had a clean, flat-topped rectangular shape with rise and fall times of  $< 500$  ps.

The curves in figure 3.2 show the response of a 25- $\mu\text{m}$ -gap device with an applied bias voltage of 10 V. The generation rate for the top panel response curve was  $\sim 10^{24}\text{cm}^{-3}\text{s}^{-1}$ . The middle and bottom panels show the response of the same device with the light-pulse intensity attenuated by neutral density filters to 5% and 1%, respectively, of the amplitude for the top panel. Note that the time axis extends to 200 ns for the top and middle panels and extends to 500 ns for the bottom panel. For high-intensity excitation, shown in the top panel of figure 3.2, the photoconductor reproduces the rectangular shape of laser-diode pulse fairly well. As the excitation intensity is reduced to 5% of the previous value, shown in the middle panel of figure 3.2, the photoconductor response develops a slow time constant which results in a long decay tail. As the excitation intensity is further reduced to 1% of the initial value, shown in the bottom panel of figure 3.2, the long time constant tail becomes more prominent.

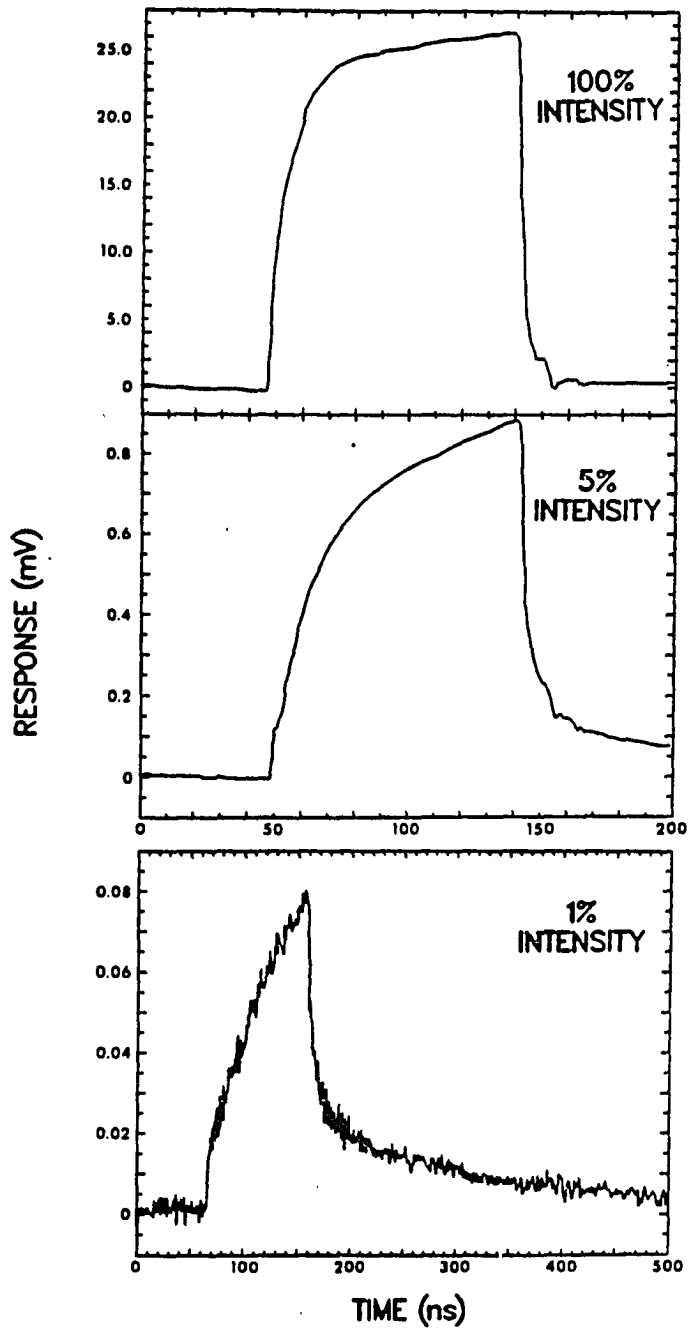


Figure 3.2: Measured response, in mV, of an InP:Fe photoconductor to 93-ns rectangular-pulse, laser-diode excitation.

### Model Development and Results

Iron in indium phosphide is a deep-level, acceptor-like impurity and acts as a trapping and recombination center. The iron site can exist in one of two charge states, negative and neutral. A neutrally charged iron site can capture (trap) an electron, thereby becoming negative, and a negatively charged iron site can capture a hole and become neutral. This provides a mechanism for the recombination of electrons and holes other than band-to-band radiative recombination. The capture cross section of iron in indium phosphide for electrons can be estimated from deep-level transient spectroscopy measurements. One finds that the capture cross section is  $\sim 3 \times 10^{-14} \text{cm}^2$  [3.2, 3.3]. This is a fairly large capture cross section and, for material doped at  $\sim 10^{16} \text{cm}^{-3}$ , leads to rapid electron capture. The hole capture cross section has not been measured directly, but my results suggest that it is comparable to the electron capture cross section. Thus, the trap assisted recombination process in  $\sim 10^{16} \text{cm}^{-3}$ -doped InP:Fe dominates band-to-band radiative recombination. Because iron is a deep-level impurity with an energy state near the middle of the

band gap, thermal emission of electrons or holes from the iron sites at room temperature is negligible on the time scale of interest here.

The dynamics of transient photoconductivity in InP:Fe are assumed to be adequately described by continuity and current equations for electrons and holes, a rate equation for trapping kinetics, and Poisson's equation. From chapter 2, the continuity equations for electrons and holes can be written as

$$\frac{\partial n}{\partial t} = g(\mathbf{r}, t) - R_n(\mathbf{r}, t) + \frac{1}{q} \nabla \cdot \mathbf{J}_n, \quad (3.1)$$

and

$$\frac{\partial p}{\partial t} = g(\mathbf{r}, t) - R_p(\mathbf{r}, t) - \frac{1}{q} \nabla \cdot \mathbf{J}_p, \quad (3.2)$$

where  $n(\mathbf{r}, t)$  and  $p(\mathbf{r}, t)$  denote electron and hole densities,  $g(\mathbf{r}, t)$  is the electron-hole-pair photogeneration rate,  $R_n(\mathbf{r}, t)$  and  $R_p(\mathbf{r}, t)$  are the electron and hole reduction rates resulting from trapping on iron sites,  $q$  is the electronic charge, and  $\mathbf{J}_n(\mathbf{r}, t)$  and  $\mathbf{J}_p(\mathbf{r}, t)$  are the electron and hole current densities. The sum of the density of iron sites in the neutral charge state  $n_T^0$  and the negatively charged state  $n_T^-$  is equal to the total density  $N_T$  of iron sites.

$$n_T^0 + n_T^- = N_T \quad (3.3)$$

The equation for trapping kinetics can be written in terms of negatively charged iron sites (trapped electrons) as

$$\frac{\partial n_T^-}{\partial t} = R_n - R_p. \quad (3.4)$$

Poisson's equation couples the transport of electrons and holes through the electric-field-driven convection (drift) component of the currents and is written as

$$\nabla^2 \psi = -\frac{q}{\epsilon}(p - n - n_T^- + N_D^+ - N_A^-), \quad (3.5)$$

where  $\psi$  is the electric potential,  $\epsilon$  is the static dielectric constant of the material, and  $N_D^+$  and  $N_A^-$  are the shallow donor and acceptor doping densities.

The goal is to develop a simple model, based on trapping and recombination of electrons and holes, which describes the bulk-material-response characteristics of InP:Fe. In order to derive model equations that represent only the bulk-material-response characteristics in terms of trapping dynamics, spatial uniformity is assumed. This is a reasonable assumption for the central region of a long photoconductor where space-charge neutrality holds and the boundary effects of free surfaces and electrical contacts can be neglected. The carrier reduction rates resulting from

trapping of electrons and holes on iron sites are modeled as being proportional to the product of free-carrier density times the number of available trapping sites of which that carrier type can be captured. Thus the carrier reduction rates are written as

$$R_n = B_n n n_T^o \quad (3.6)$$

and

$$R_p = B_p p n_T^- \quad (3.7)$$

where

$$B_n = \langle v_n \rangle \sigma_n \quad (3.8)$$

and

$$B_p = \langle v_p \rangle \sigma_p. \quad (3.9)$$

Here  $\langle v_n \rangle$  and  $\langle v_p \rangle$  are the electron and hole thermal velocities, and  $\sigma_n$  and  $\sigma_p$  are the electron and hole capture cross sections on the iron sites.

The densities can be written in terms of excess densities,  $\Delta n$ ,  $\Delta p$ , and  $\Delta n_T^-$ , which represent deviations from the densities at thermal equilibrium. In the case of transient photoconductivity in semi-insulating InP:Fe, the excess electron and hole densities are large compared to their thermal-equilibrium values.

With the assumption of spatial uniformity, Poisson's equation gives the space-charge neutrality condition for the excess densities,

$$\Delta p - \Delta n - \Delta n_{T}^{-} = 0. \quad (3.10)$$

This allows the four governing equations, (3.1), (3.2), (3.4), and (3.5), to be reduced to two. Choosing to eliminate  $\Delta n_{T}^{-}$ , applying detailed balance, and neglecting the small thermal-equilibrium electron and hole densities yield two model equations in terms of excess electron and hole densities,

$$\frac{d\Delta n}{dt} = g(t) - B_n(N_T - n_{T_o}^{-} - \Delta p + \Delta n)\Delta n \quad (3.11)$$

and

$$\frac{d\Delta p}{dt} = g(t) - B_p(n_{T_o}^{-} + \Delta p - \Delta n)\Delta p, \quad (3.12)$$

where  $n_{T_o}^{-}$  is the thermal-equilibrium, negatively charged iron density.

The model equations are put into dimensionless form. First, the driving term is written as  $g(t) = g_o\phi(t)$ , where  $g_o$  is the maximum generation rate produced by the incident radiation and  $0 \leq \phi(t) \leq 1$  gives the temporal shape of the applied radiation pulse. A basic material time constant (the equilibrium electron-capture time constant) is defined as

$$\tau_{n_o} = \frac{1}{B_n(N_T - n_{T_o}^{-})}. \quad (3.13)$$

A dimensionless time is defined as  $\hat{t} = t/\tau_{n_0}$ . A dimensionless generation rate that represents the intensity of the applied radiation is defined as

$$I = \frac{g_0 \tau_{n_0}}{N_T}. \quad (3.14)$$

The excess electron and hole densities are normalized to the quantity  $g_0 \tau_{n_0}$  giving the dimensionless excess densities,

$$\hat{n} = \frac{\Delta n}{g_0 \tau_{n_0}} \quad (3.15)$$

and

$$\hat{p} = \frac{\Delta p}{g_0 \tau_{n_0}}. \quad (3.16)$$

Finally, two material parameters are defined as

$$B = \frac{B_p}{B_n} \quad (3.17)$$

and

$$C = \frac{n_{T_0}}{N_T}. \quad (3.18)$$

The two model equations in in dimensionless form can then be written as

$$\frac{d\hat{n}}{d\hat{t}} = \phi(\hat{t}) - \hat{n} + \frac{I}{1-C}(\hat{p} - \hat{n})\hat{n} \quad (3.19)$$

and

$$\frac{d\hat{p}}{d\hat{t}} = \phi(\hat{t}) - \frac{BC}{1-C}\hat{p} - \frac{IB}{1-C}(\hat{p} - \hat{n})\hat{p}. \quad (3.20)$$

The material's characteristic transient photoconductive response can be expressed in terms of electrical conductivity,

$$\sigma = q(\mu_n \Delta n + \mu_p \Delta p), \quad (3.21)$$

where  $\mu_n$  and  $\mu_p$  are the electron and hole mobilities. The electrical conductivity can be written in terms of dimensionless variables as

$$\hat{\sigma} = \hat{n} + M\hat{p}, \quad (3.22)$$

where

$$\hat{\sigma} = \frac{\sigma}{qg_0\tau_{n_0}\mu_n} \quad (3.23)$$

and

$$M = \frac{\mu_p}{\mu_n}. \quad (3.24)$$

The material parameters contained in the model equations are  $\tau_{n_0}$ ,  $B$ ,  $C$ , and  $M$ . The electron and hole mobilities in InP:Fe are known [3.4]. From these results, the value for the mobility parameter  $M$  is taken to be 0.05. Because the electron mobility far exceeds the hole mobility, the photoconductor response to low-intensity impulses is dominated by the equilibrium electron capture time constant  $\tau_{n_0}$ . From the low-intensity electron-beam experimental data in figure 3.1, the value of  $\tau_{n_0}$  is taken to

be 630 ps. Experimental data is not available to directly determine the values for  $B$  and  $C$ . The InP:Fe used in these experiments was grown for use as semi-insulating substrate material. For this reason, the iron doping concentration was made to be much larger than the shallow donor concentration. Thus, the compensation ratio parameter  $C$  is much less than one. For the following calculations a value of  $C = 0.01$  was used. In order to determine the value for  $B$ , both the electron and hole capture cross sections must be known. Information is available on the electron capture cross section [3.2, 3.3] but not on the hole capture cross section. The model calculations are in qualitative agreement with the data for  $B \simeq 1$ . For the results presented here, a value of  $B = 0.75$  was used.

The model equations (3.11) and (3.12) are two coupled nonlinear ordinary differential equations. At low intensity ( $I \ll 1$ ), the equations become linear, uncouple, and are easily solved analytically. For intensity parameter  $I$  not vanishingly small, the equations must be solved numerically. A fourth-order Runge-Kutta method was used to solve the coupled, nonlinear model equations.

In figure 3.3, numerically computed solutions for impulse excitation are presented. For the computations, the strength of the impulse is

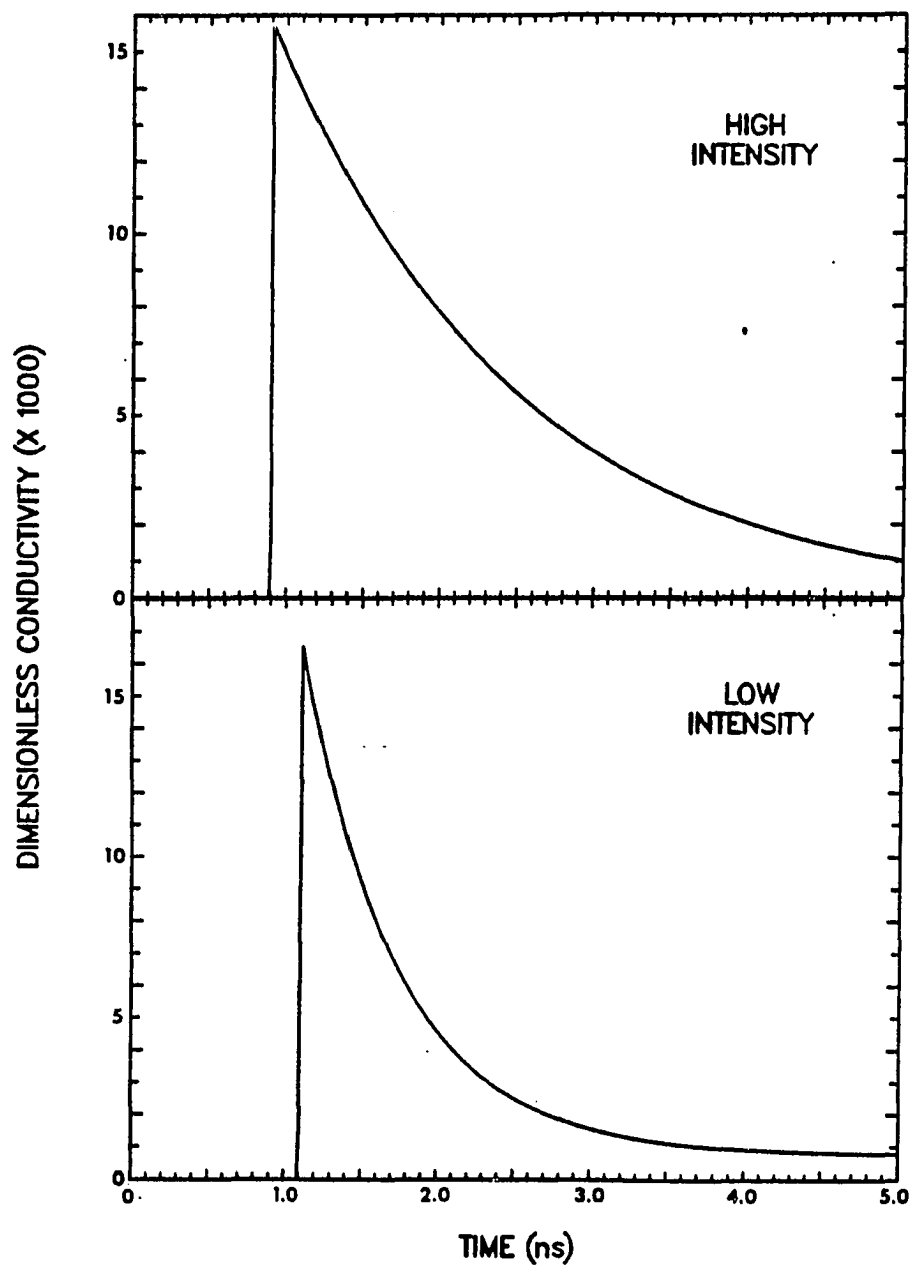


Figure 3.3: Calculated response of an InP:Fe photoconductor to impulse excitation.

determined by the product of the intensity parameter  $I$  and the width of the impulse,  $\hat{t}_w$ . The top panel of figure 3.3 shows a high-intensity impulse result computed with  $I = 10^4$  and  $\hat{t}_w = 0.01$ . The lower panel shows a low-intensity impulse result computed with  $I = 0.001$  and  $\hat{t}_w = 0.01$ . Both high-intensity and low-intensity cases show nearly exponential decays, with the time constant for the high-intensity case being larger than that of the low-intensity case. The low-intensity result shows a weak ( $\sim 5\%$ ) tail in addition to the exponential decay. The model results show good qualitative agreement with the corresponding experimental results in figure 3.1.

In figure 3.4, numerically computed solutions to the model equations for rectangular-pulse excitation are presented. An excitation pulse width of  $\hat{t}_w = 150$  ( $t_w \simeq 93$  ns) was used for these computations. A value of  $I = 0.01$  was used for the result shown in the top panel of figure 3.4. This value of  $I$  corresponds approximately to the experimental generation rate for the top panel of figure 3.2. The solutions to the model equations shown in the middle and bottom panels of figure 3.4 were computed with  $I$  reduced to 5% and 1% of the value for the top panel. These values correspond approximately to the generation rates for the experimental results presented in the corresponding panels of figure 3.2. The relative

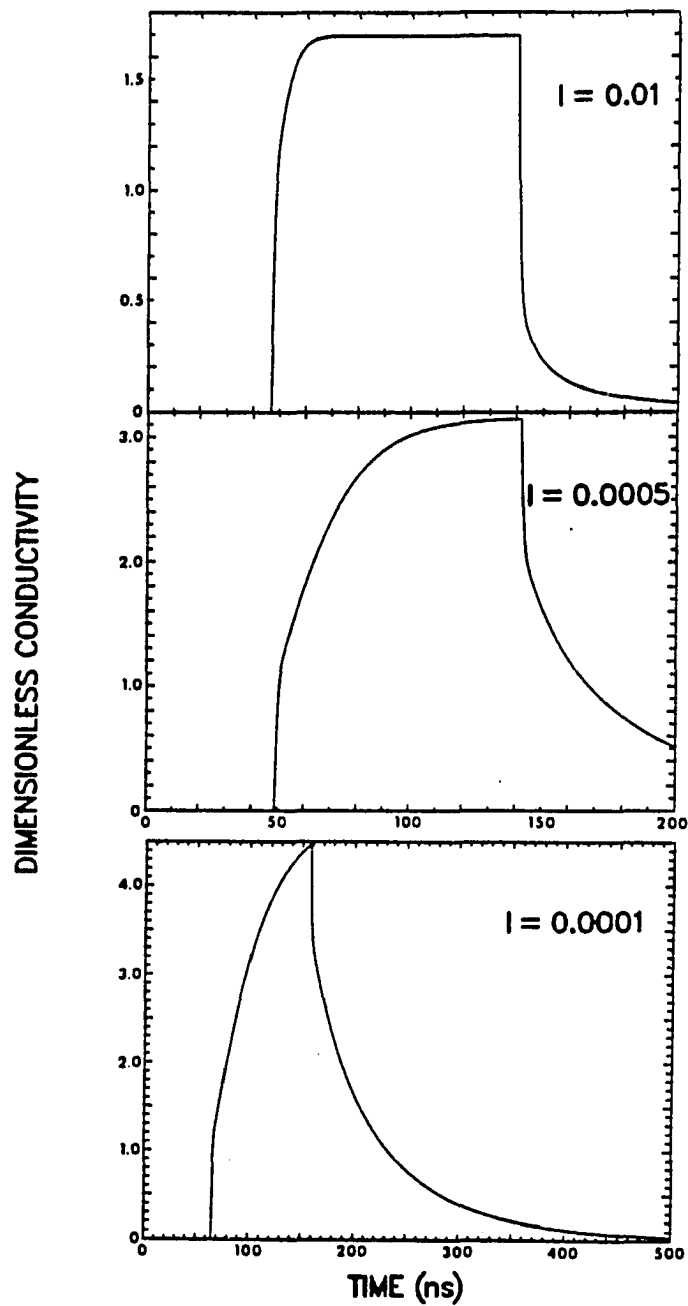


Figure 3.4: Calculated response of an InP:Fe photoconductor to 93-ns rectangular-pulse excitation.

experimental generation rates for figure 3.2 are accurately known, whereas, the absolute generation rates are only approximately known. The computed response shape shown in the top panel of figure 3.4 reproduces the rectangular-shaped driving pulse fairly well. At the lower intensities, the contribution of hole current to the photoconductor response increases and a slower time constant resulting from hole decay can be seen. The model results presented in figure 3.4 show good qualitative agreement with the experimental results presented in figure 3.2.

### Discussion and Conclusion

The essential features of InP:Fe that lead to the experimentally observed behavior are the following:

- (1) The electron mobility is  $\sim 20$  times larger than the hole mobility.
- (2) The capture rate coefficients of electrons and holes,  $B_n$  and  $B_p$ , are approximately equal.
- (3) At thermal equilibrium, the density of neutral iron sites (which can capture electrons) is much greater than the density of negatively charged iron sites (which can capture holes).

Because the electron mobility far exceeds the hole mobility, the electron current dominates the hole current in the photoconductor response unless the density of holes is much greater than the density of electrons. At low intensities, the equilibrium population of iron charge states is not significantly changed by the photogenerated carriers. As a result, the capture rates of electrons and holes are independent of the carrier densities, and the electron and hole densities decay as independent exponentials with different time constants. The model equations describe this behavior in the limit of small  $I$ . In this case, the electron time constant is given by  $\tau_{n_0}$  and the hole time constant is given by  $(1 - C)\tau_{n_0}/BC$ . Because the neutral iron density exceeds the negatively charged iron density ( $C \ll 1$ ), the electron time constant is much less than the hole time constant.

For low-intensity impulse excitation, the electron and hole densities are initially equal so that the electron time constant  $\tau_{n_0}$  dominates the response. This situation is shown in the lower panels of figure 3.1 (experimental result) and figure 3.3 (model result). For low-intensity pulse excitation with a pulse length much greater than  $\tau_{n_0}$ , the hole density can build up to far exceed the electron density. In this case, the contribution to the photoconductor response resulting from hole conduction is important.

The photoconductor response will show a fast time constant owing to electron current and a slow time constant owing to hole current. Because of the larger contribution of hole current, the photoconductor response does not faithfully reproduce the rectangular driving pulse. This case is seen in the lower panels of figure 3.2 (experimental result) and figure 3.4 (model result).

At high intensities, the electron and hole densities do not decay independently. Indeed, for electron and hole densities far exceeding the total iron concentration, the electron and hole densities are approximately equal. Thus, they decay together so that

$$\frac{d\Delta n}{dt} \simeq \frac{d\Delta p}{dt}. \quad (3.25)$$

This equation determines the charge-state densities of the iron impurities.

The mutual decay time constant of the electrons and holes is seen to be

$$\tau_{HI} \simeq \frac{(1 - C)(1 + B)}{B} \tau_{n_0}. \quad (3.26)$$

This high-intensity time constant holds as long as the density of electrons and holes exceeds that of the iron impurities. For high-intensity impulse excitation, the electron and hole densities decay with the time constant  $\tau_{HI}$ . From equation (3.26) it can be seen that  $\tau_{HI}$  is somewhat larger than

$\tau_{n_0}$ . This behavior is shown in the top panels of figure 3.1 (experimental result) and figure 3.3 (model result). For high-intensity pulse excitation, the electron and hole densities are equal and respond with a time constant  $\tau_{HI}$ . Thus, for pulses which are long with respect to  $\tau_{HI}$ , the photoconductor faithfully reproduces the excitation pulse shape. This situation is seen in the top panels of figure 3.2 (experimental result) and figure 3.4 (model result). The middle panels of figures 3.2 and 3.4 show intermediate intensity cases.

InP:Fe photoconductors are often used as radiation detectors. From the results presented here it is shown that, for low-intensity excitation, the material response can be described as having two different time constants. The shorter time constant results from electron trapping and the longer time constant results from hole trapping. For radiation pulse lengths intermediate between these two time constants, detectors can faithfully replicate the temporal shape of the incident radiation signal. For radiation pulse lengths comparable to the longer (hole) time constant, the temporal response shape of the detector will be distorted. Of course, for radiation pulse lengths much longer than the hole time constant, the detector will faithfully replicate the radiation pulse shape. For high-intensity excitation,

the detector response is determined by the single time constant  $\tau_{HI}$ . The detector will faithfully replicate a high-intensity radiation pulse which is long with respect to this time constant.

For fast pulse generation and sampling applications, the impulse response of the photoconductor is the important characteristic. My results show that the material response following impulse excitation is essentially an exponential decay. The decay time constant for low-intensity excitation is the equilibrium electron-capture time constant  $\tau_{n_0}$ . For high-intensity impulse excitation, the decay time constant  $\tau_{HI}$  is longer.

The model presented in this chapter qualitatively accounts for the experimentally observed behavior and provides an understanding of the photoconductive response of InP:Fe based on the trapping and recombination of electrons and holes on deep-level iron impurities. The model parameters  $B$  and  $C$  were chosen to provide the best agreement with the experimental data. It is not claimed that the values chosen for  $B$  and  $C$  accurately represent the true material parameters for InP:Fe. The model displays the same basic behavior with some variation in  $B$  and  $C$ , and some aspects of the model behavior are dependent on the  $BC$  product. There

are quantitative differences between the model results and the experimental data. In order to quantitatively describe photoconductor transient response, it will be necessary to account for the transient spatial distribution of electrons, holes, deep-level impurity charge density, and electric field. The complete photoconductive device model equations, which account for these transport effects, are studied in chapter 5.

## CHAPTER 4

### GENERATION-RECOMBINATION NOISE EFFECTS RESULTING FROM DEEP-LEVEL TRAPPING

In this chapter a theory of the effect of deep-level trapping centers on the generation-recombination (g-r) noise and responsivity of an intrinsic photoconductor is presented. The deep-level centers can influence the g-r noise and responsivity in three main ways: (i) they can shorten the bulk carrier lifetime by Shockley-Read-Hall recombination; (ii) for some values of the capture cross sections, deep-level densities, and temperature, the deep levels can trap a significant fraction of the photogenerated minority carriers which reduces the effective minority carrier mobility and diffusivity and thus reduces the effect of carrier sweep out on both g-r noise and responsivity; (iii) the deep-level centers add a new thermal noise source which results from fluctuations between bound and free carriers. The strength of this new noise source decreases with decreasing temperature at a slower rate than band-to-band thermal g-r noise. Calculations are presented for

an  $X = 0.21$ ,  $n$ -type  $\text{Hg}_{1-x}\text{Cd}_x\text{Te}$  photoconductor using the parameters of a commonly occurring deep-level center in this material. It is shown that, for typical operating conditions, photoconductive detector performance begins to degrade as the deep-level density exceeds  $\sim 10^{16}\text{cm}^{-3}$ .

### Introduction

Arrays of  $\text{HgCdTe}$  photoconductors are presently used in high-resolution thermal imaging systems. Under normal operating conditions, the dominant noise contribution in these devices results from fluctuations in the carrier density [4.1, 4.2]. Discussions of this generation-recombination (g-r) noise for the case in which the density fluctuations result totally from the band-to-band g-r processes have been presented [4.3, 4.4, 4.5]. Here the effect of deep-level centers on g-r noise and responsivity is examined. It will be shown that deep-level centers can affect g-r noise and responsivity in three principal ways: (i) Deep levels can lead to Shockley-Read-Hall (SRH) recombination. This effect can be included in the previous discussions by simply changing the excess carrier lifetime to include this recombination process. (ii) For certain values of the deep-level parameters, a significant fraction of the photogenerated minority carriers may be trapped on the

deep-level sites. This trapping will change effective minority carrier mobilities and diffusivities and hence modify sweep-out effects on both g-r noise and responsivity. (iii) Density fluctuations between free and trapped carriers leads to another noise source. This additional noise source can be particularly important at low temperatures and low background conditions.

The importance of deep-level centers clearly depends on the density and electrical properties of the centers. The electrical properties of a common deep-level center in HgCdTe have been measured by Polla and Jones [4.6] using deep-level transient spectroscopy. They found that this deep level commonly occurs at densities between  $10^{14}\text{cm}^{-3}$  and  $10^{16}\text{cm}^{-3}$ . Electron and hole capture cross sections were measured and found to be  $\sigma_n \sim 10^{-15}\text{cm}^2$  and  $\sigma_p \sim 10^{-17}\text{cm}^2$ . The energy of the deep level was found to be about  $0.4 E_g$  above the valence band where  $E_g$  is the band-gap energy. Based on the sizes of the capture cross sections (the electron cross section being much larger than the hole cross section), they suggest that the electron is likely captured at a Coulomb attractive center and the hole at a neutral center so that the likely charge states for the deep level are neutral and positive. (Charge states of positive and double positive are

another possible interpretation.) The measurements were made on *p*-type materials.

In this chapter, a theory of the effects of a deep-level center with two accessible charge states on the generation-recombination noise and responsivity of an intrinsic photoconductor is presented. Specific calculations are done for *n*-type,  $X = 0.21$   $\text{Hg}_{1-X}\text{Cd}_X\text{Te}$  because this material is currently used for infrared detection in the 8 – 12  $\mu\text{m}$  band. However, the basic theoretical formulation does not depend on the material properties of this system, and these results should apply to other intrinsic photoconductors. The results of Polla and Jones [4.6] are used to describe the deep-level center. (That is, it is assumed that the deep-level center characterized by Polla and Jones in *p*-type material also occurs in *n*-type material.) Although the notation is for centers with neutral and positive charge states, the results are simple to transcribe to centers with other charge states. Because somewhat different behavior is predicted if the deep-level center can trap a significant fraction of the photogenerated minority carriers, calculations are also presented in which the minority carrier (hole) capture cross section is large compared with the majority carrier capture cross section.

### Theoretical Approach

The case of an  $n$ -type photoconductor containing a deep-level center with two accessible charge states is considered. To be specific, the charge states are taken to be neutral and positive. The densities of the neutral and positive charge state deep-level centers will be denoted as  $n_T^0$  and  $n_T^+$ . To convert the results to describe, for example, a center with charge states neutral and negative, one simply replaces  $n_T^0$  by  $n_T^-$  and  $n_T^+$  by  $n_T^0$ . (That is,  $n_T^+$  or  $n_T^0$  refer to the center with a trapped hole and  $n_T^-$  or  $n_T^0$  refer to the center without a trapped hole.) Photoconductors which are made from  $p$ -type material can also be described by the theory by interchanging the role of electrons and holes and interchanging the role of the two charge states of the center. The case is considered in which the free electron density is determined by shallow impurities, not by the deep-level center. Thus, the equilibrium electron density  $n_0$  is much greater than  $n_T^+$ . Small signal excitation, so that the density of photogenerated carriers is small compared to the majority carrier density, is considered.

A one-dimensional model is used to describe the photoconductor. The detector length is  $2L$  and the contacts are at  $x = \pm L$ . The reason

for setting up the problem in this way is that more symmetry is obtained by having the origin of the  $x$ -axis at the center of the photoconductor. The detector width and thickness are  $W$  and  $d$ , respectively. Space charge neutrality is taken to be maintained so that excess densities satisfy the relation

$$\Delta p(x, t) - \Delta n(x, t) + \Delta n_T^+(x, t) = 0, \quad (4.1)$$

where  $\Delta p$  and  $\Delta n$  are the excess hole and electron densities, respectively, and  $\Delta n_T^+$  is the excess density of positively charged deep-level centers. The contacts are taken to be ohmic with an infinite surface recombination velocity so that all excess densities vanish at  $x = \pm L$ .

The determination of the g-r noise voltage begins with the Wiener-Khintchine theorem for the noise spectral density

$$G(V, \omega) = 4 \int_0^\infty \cos(\omega t) \langle \Delta V(t) \Delta V(0) \rangle dt, \quad (4.2)$$

where  $\Delta V$  is the deviation from the time-averaged terminal voltage. The noise voltage is related to the spectral density by

$$V_N = [G(V, \omega) \Delta f]^{1/2}, \quad (4.3)$$

where  $\Delta f$  is the bandwidth. To determine the change in terminal voltage, at a constant current bias, in terms of carrier densities, the equation for

the conduction current density

$$J = qE(\mu_n n + \mu_p p) + q \left( D_n \frac{\partial n}{\partial x} - D_p \frac{\partial p}{\partial x} \right) \quad (4.4)$$

is integrated along the length of the detector. Here  $E$ , the applied electric field, is spatially uniform because of the charge neutrality assumption. Taking the change in carrier densities to be small compared with the majority carrier equilibrium density and noting that the excess densities vanish at the contacts (so the diffusion contribution in equation (4.4) drops out) gives

$$\Delta V(t) = - \frac{V[\mu_n \int_{-L}^L \Delta n(x,t) dx + \mu_p \int_{-L}^L \Delta p(x,t) dx]}{2L(\mu_n n_o + \mu_p p_o)}, \quad (4.5)$$

where  $V$  is the time-average bias voltage. Substituting equation (4.5) into equation (4.2) gives the noise spectral density in terms of density-density correlation functions.

In general, there are four density-density correlation functions to evaluate. Although it is not difficult to evaluate these functions, the results produced are somewhat complicated simply because of the relatively large number of terms involved. For  $X \sim 0.21$   $\text{Hg}_{1-X}\text{Cd}_X\text{Te}$ , the electron mobility is about 400 times the hole mobility, and thus the electron contribution in equation (4.5) is much larger than the hole contribution. For ease of presentation, only the electron terms in equation (4.5) are kept. For other

materials this simplification may not be valid, and it may be necessary to retain the other terms. With this simplification, the noise spectral density becomes

$$G(V, \omega) = \frac{4V^2}{n_0^2} \int_0^\infty \cos(\omega t) \left( \frac{1}{2L} \right)^2 \int_{-L}^L \int_{-L}^L \langle \Delta n(x, t) \Delta n(x', 0) \rangle dx' dx dt. \quad (4.6)$$

It thus becomes necessary to calculate the correlation function  $\langle \Delta n(x, t) \Delta n(x', 0) \rangle$ .

In order to evaluate this correlation function, transport equations describing the evolution of the excess carrier density must be considered. From chapter 2, continuity equations in one spatial dimension for the excess densities can be written as

$$\frac{\partial \Delta n}{\partial t} = G + G_n - R_n - \frac{\Delta p}{\tau} + \frac{1}{q} \frac{\partial}{\partial x} \Delta J_n, \quad (4.7)$$

$$\frac{\partial \Delta p}{\partial t} = G + G_p - R_p - \frac{\Delta p}{\tau} - \frac{1}{q} \frac{\partial}{\partial x} \Delta J_p, \quad (4.8)$$

$$\frac{\partial \Delta n_T^\dagger}{\partial t} = (G_n - R_n) - (G_p - R_p), \quad (4.9)$$

where  $G$  is the electron-hole pair photogeneration rate,  $G_n$  and  $G_p$  are the electron and hole generation rates resulting from thermal emission from the deep-level centers,  $R_n$  and  $R_p$  are the capture rates of electrons and

holes on the deep-level centers,  $\tau$  is the excess carrier lifetime from band-to-band recombination. The excess current densities  $\Delta J_n$  and  $\Delta J_p$  are the usual drift/diffusion equations derived in chapter 2 only written in terms of excess electron and hole densities. The thermal generation and capture rates of excess electrons and holes on deep levels are given by

$$G_n = B_n n_1 (N_T - n_T^+), \quad (4.10)$$

$$R_n = B_n n n_T^+, \quad (4.11)$$

$$G_p = B_p p_1 n_T^+, \quad (4.12)$$

$$R_p = B_p p (N_T - n_T^+), \quad (4.13)$$

where

$$B_n = \langle V_n \rangle \sigma_n, \quad (4.14)$$

$$B_p = \langle V_p \rangle \sigma_p, \quad (4.15)$$

$$n_1 = N_c(T) e^{(E_T - E_c)/kT}, \quad (4.16)$$

$$p_1 = N_v(T) e^{(E_v - E_T)/kT}, \quad (4.17)$$

and  $\langle V_{n(p)} \rangle$  is the electron (hole) thermal velocity,  $\sigma_{n(p)}$  is the electron (hole) capture cross section,  $N_T$  is the total density of deep-level centers,  $N_{c(v)}$  is the electron (hole) effective density of states,  $E_{c(v)}$  is the energy position of

the conduction (valence) band, and  $E_T$  is the energy position of the deep impurity level.

Using the charge neutrality condition [equation (4.1)]  $\Delta p$  can be eliminated and the transport equations become (for low level excitation)

$$G = \Theta_1 \Delta n + \Theta_2 \Delta n_T^+, \quad (4.18)$$

$$0 = \Theta_3 \Delta n + \Theta_4 \Delta n_T^+, \quad (4.19)$$

where the operators  $\Theta_i$  are defined by

$$\Theta_1 = \frac{\partial}{\partial t} + \frac{1}{\tau} + B_n n_{T_o}^+ + \mu E \frac{\partial}{\partial x} - D \frac{\partial^2}{\partial x^2}, \quad (4.20)$$

$$\Theta_2 = B_n (n_1 + n_o) - \frac{1}{\tau} - \gamma \mu_p E \frac{\partial}{\partial x} + \gamma D_p \frac{\partial^2}{\partial x^2}, \quad (4.21)$$

$$\Theta_3 = B_n n_{T_o}^+ - B_p (N_T - n_{T_o}^+), \quad (4.22)$$

$$\Theta_4 = \frac{\partial}{\partial t} + B_n (n_1 + n_o) + B_p [p_1 + p_o + (N_T - n_{T_o}^+)]. \quad (4.23)$$

Here  $\mu$  is the ambipolar mobility (defined positive in  $n$ -type material),  $D$  is the ambipolar diffusivity, the subscript  $o$  indicates equilibrium values, and

$$\gamma = \frac{\mu_n n_o}{\mu_n n_o + \mu_p p_o}. \quad (4.24)$$

It is convenient to define Green's functions for the transport equations by

$$\delta(x - x') \delta(t) = \Theta_1(x, t) K_1(x, x', t) + \Theta_2(x, t) K_3(x, x', t), \quad (4.25)$$

$$0 = \Theta_1(x, t)K_2(x, x', t) + \Theta_2(x, t)K_4(x, x', t), \quad (4.26)$$

$$0 = \Theta_3(x, t)K_1(x, x', t) + \Theta_4(x, t)K_3(x, x', t), \quad (4.27)$$

$$\delta(x - x')\delta(t) = \Theta_3(x, t)K_2(x, x', t) + \Theta_4(x, t)K_4(x, x', t), \quad (4.28)$$

with the boundary and initial conditions

$$K_i(\pm L, x', t) = 0, \quad (4.29)$$

$$K_i(x, x', 0) = 0. \quad (4.30)$$

The Green's function tells how a density fluctuation propagates. Thus, if  $\Delta n(x, 0)$  and  $\Delta n_T^+(x, 0)$  are specified, at a later time one has (in matrix notation)

$$\begin{bmatrix} \Delta n(x, t) \\ \Delta n_T^+(x, t) \end{bmatrix} = \int_{-L}^L \begin{bmatrix} K_1(x, x', t) & K_2(x, x', t) \\ K_3(x, x', t) & K_4(x, x', t) \end{bmatrix} \begin{bmatrix} \Delta n(x', 0) \\ \Delta n_T^+(x', 0) \end{bmatrix} dx'. \quad (4.31)$$

If the problem is specified by an external generation rate, one has

$$\begin{bmatrix} \Delta n(x, t) \\ \Delta n_T^+(x, t) \end{bmatrix} = \int_{-\infty}^t \int_{-L}^L \begin{bmatrix} K_1(x, x', t - t') & K_2(x, x', t - t') \\ K_3(x, x', t - t') & K_4(x, x', t - t') \end{bmatrix} \begin{bmatrix} G(x', t') \\ 0 \end{bmatrix} dx' dt'. \quad (4.32)$$

Equation (4.31) is of use in the g-r noise calculation because it allows the density-density correlation function to be written as

$$\begin{aligned} \langle \Delta n(x, t) \Delta n(x', 0) \rangle &= \int_{-L}^L K_1(x, x'', t) \langle \Delta n(x'', 0) \Delta n(x', 0) \rangle \\ &+ K_2(x, x'', t) \langle \Delta n_T^+(x'', 0) \Delta n(x', 0) \rangle dx''. \end{aligned} \quad (4.33)$$

Thus, the problem reduces to finding the Green's functions and the instantaneous correlation functions (which are already known [4.8]). The solution for the Green's function is given in the following section. Notice that if the term proportional to  $\mu_p$  in equation (4.5) has been kept when substituting into equation (4.2), the additional terms could all be described in terms of the same Green's functions  $K_i$  ( $i = 3$  and  $4$  would also appear) and instantaneous correlation functions which are well known [4.8].

The responsivity is also found in terms of the Green's functions  $K_i$ . It is defined as

$$R(V, \omega) = \frac{[\overline{V_s^2}]^{1/2}}{[\overline{P_s^2}]^{1/2}} \quad (4.34)$$

where  $[\overline{V_s^2}]^{1/2}$  is the rms time average of the output signal voltage and  $[\overline{P_s^2}]^{1/2}$  is the rms time average of the input optical power. The signal voltage is found in terms of the photogenerated carrier density by equation

(4.5). Taking a sinusoidal generation rate of the form

$$g(t) = \frac{\eta Q_s}{d} \cos(\omega t) \quad (4.35)$$

where  $\eta$  is the quantum efficiency and  $Q_s$  is the signal photon flux, the excess carrier densities are found in terms of the Green's functions by equation (4.32). To be consistent with the noise voltage calculation, the contribution from the hole current is neglected as small compared to the electron contribution.

The mathematical details of the determination of the Green's functions and evaluation of various spatial integrals of the Greens's functions are given in the following section. To simplify the results, it is assumed that the ambipolar and minority carrier mobilities and diffusivities are nearly equal, that  $\gamma$  [defined in equation (4.24)] is nearly unity and that  $n_{T_0}^+ \ll N_T$ . These approximations aren't really necessary (that is the problem can still be easily solved without making them), but they are well satisfied for the case considered and they considerably simplify the statement of the results.

The results, for  $n$ -type material, are

$$R(V, \omega) = \frac{\lambda}{hc} \frac{\eta}{2LWd} \frac{V}{n_{T_0}} |Q(\omega)|, \quad (4.36)$$

$$\frac{V_N(V, \omega)}{(\Delta f)^{1/2}} = \frac{2V}{n_o \sqrt{2LWd}} \left[ (p_o + H(\omega)n_{T_o}^+ + F(\omega)\langle \Delta n_B \rangle) \phi(\omega) \right]^{1/2}, \quad (4.37)$$

$$D^*(V, \omega) = \frac{\lambda}{2hc} \left( \frac{\eta}{Q_B} \right)^{1/2} \left[ \frac{\phi(\omega)}{\phi(0)} \langle \Delta n_B \rangle \left( \frac{1 + (\text{Im}[Q(\omega)]/\phi(\omega))^2}{p_o + H(\omega)n_{T_o}^+ + F(\omega)\langle \Delta n_B \rangle} \right) \right]^{1/2} \quad (4.38)$$

where

$$\langle \Delta n_B \rangle = \frac{\eta Q_B}{d} \phi(0), \quad (4.39)$$

$$\phi(\omega) = \text{Re}[Q(\omega)], \quad (4.40)$$

$$F(\omega) = \frac{-\text{Im}[Q(\omega)]}{\omega \phi(\omega) \phi(0)}, \quad (4.41)$$

$$H(\omega) = \frac{\text{Re}\{Q(\omega)[1 - A(\omega)] + \sigma(\omega)\}}{\phi(\omega)}, \quad (4.42)$$

$$Q(\omega) = \frac{\tau'}{1 + i\omega\tau'} \left( 1 + \frac{(\alpha_2 - \alpha_1) \sinh(\alpha_1 L) \sinh(\alpha_2 L)}{(\alpha_1 \alpha_2 L) \sinh[(\alpha_1 - \alpha_2)L]} \right), \quad (4.43)$$

$$\alpha_{1,2} = \frac{\mu' E}{2D'} \pm \left[ \left( \frac{\mu' E}{2D'} \right)^2 + \frac{1 + i\omega\tau'}{D'\tau'} \right]^{1/2}, \quad (4.44)$$

$$\frac{1}{\tau'} = \frac{[1 - \beta(\omega)]}{\tau} + B_c [n_{T_o}^+ + \beta(\omega)(n_1 + n_o)], \quad (4.45)$$

$$\mu' = \mu[1 - \beta(\omega)], \quad (4.46)$$

$$D' = D[1 - \beta(\omega)], \quad (4.47)$$

$$\beta(\omega) = \frac{[B_p(N_T - n_{T_o}^+) - B_n n_{T_o}^+]}{\{i\omega + B_n(n_1 + n_o) + B_p[p_1 + p_o + (N_T - n_{T_o}^+)]\}}, \quad (4.48)$$

$$A(\omega) = \frac{[i\omega + B_n(n_1 + n_o + n_{T_o}^+)]}{[i\omega + B_n(n_1 + n_o + n_{T_o}^+) + B_p(p_1 + p_o)]}, \quad (4.49)$$

and

$$\sigma(\omega) = \frac{1}{i\omega + B_n(n_1 + n_o + n_{T_o}^+) + B_p(p_1 + p_o)}. \quad (4.50)$$

Here  $\lambda$  is the signal photon wavelength and  $Q_B$  is the background photon flux.

Equations (4.36) through (4.50) give the formal results for the responsivity, g-r noise, and detectivity  $D^*$  (assuming that g-r noise dominates) in the presence of deep-level centers. The results reduce to previous expressions [4.3] if the center density vanishes. The deep-level centers affect the results in three ways: the lifetime  $\tau$  is modified by SRH recombination and carrier trapping [equation (4.45)], the effective mobility  $\mu$  and diffusivity  $D$  are modified by carrier trapping [equations (4.46) and (4.47)], and a new noise source term,  $H(\omega)n_{T_o}^+$  appears [equation (4.37)].

From equation (4.37), one sees that there are three basic g-r noise sources. The term proportional to  $p_o$  describes the contribution from band-to-band thermal density fluctuations. (This contribution will be referred to as the thermal noise term.) The term proportional to  $\langle \Delta n_B \rangle$  describes the

contribution from density fluctuations on the background generated carrier density. (This contribution will be referred to as the background noise term.) Both of these terms remain as the deep-level center density goes to zero. The term proportional to  $n_{T_0}^+$  describes a new thermal noise source resulting from fluctuations between trapped and free carriers. This term can be quite important at low temperatures because  $p_0$  decreases faster with decreasing temperature than does  $n_{T_0}^+$ .

The modification of the effective mobility and diffusivity occurs because some of the photogenerated carriers may become trapped on the deep-level centers. Indeed, from equation (4.19), it can be seen that at steady state ( $\omega \rightarrow 0$ )

$$\Delta n_T^+(x) = \beta(0)\Delta n(x). \quad (4.51)$$

Thus,  $\beta$  is just the ratio of photogenerated bound holes ( $\Delta n_T^+$ ) to photogenerated free electrons ( $\Delta n$ ). From equation (4.48) it is seen that  $\beta$  can approach unity if  $B_p \gg B_n$  and  $(N_T - n_{T_0}^+) \gg (p_1 + p_0)$ . For  $n$ -type material,  $n_{T_0}^+$  is much less than  $N_T$  and  $N_T$  is temperature independent. However,  $p_1$  and  $p_0$  decrease rapidly with decreasing temperature. Thus, if  $B_p \gg B_n$ , minority carrier trapping will become important at low temperature. It is possible for  $\beta$  to be negative (more photogenerated electrons are trapped

than photogenerated holes causing  $\Delta n_T^+$  to be negative) if  $B_n \gg B_p$ . However, since  $n_{T_0}^+ \gg n_0$ , if  $\beta$  is negative, it is small in absolute value. The effective bulk lifetime is modified by the deep-level centers both by SRH recombination and because trapping changes the population of free and trapped carriers.

### Solution for the Green's Functions

In this section, the Green's functions defined by equations (4.25) through (4.30) are found and an integral of these functions which appears in the noise voltage expressions is evaluated. Noticing that it is really the time Fourier transform of the function that is needed [see equation (6)], we define

$$g_i(x, x', \omega) = \int_0^\infty K_i(x, x', t) e^{-i\omega t} dt. \quad (4.52)$$

Then the  $g_i(x, x', \omega)$  satisfy the transform of equations (4.25) through (4.30), (replace  $\partial/\partial t$  with  $i\omega$  in the operators  $\Theta_i$ ). In  $\omega$  space,  $\Theta_3(x, \omega)$  and  $\Theta_4(x, \omega)$  are numbers, not differential operators. Thus, from the transform of equation (4.27) one sees that  $g_1(x, x', \omega)$  and  $g_3(x, x', \omega)$  are proportional and

$$g_3(x, x', \omega) = -\frac{\Theta_4}{\Theta_3} g_1(x, x', \omega) \equiv \beta(\omega) g_1(x, x', \omega), \quad (4.53)$$

where  $\beta(\omega)$  is given by equation (4.48). Substituting equation (4.53) into the transform of equation (4.25) gives the equation for  $g_1(x, x', \omega)$

$$\begin{aligned} \delta(x - x') = & \left( i\omega + \frac{(1 - \beta)}{\tau} + B_n[n_{T_o}^+ + \beta(n_1 + n_o)] \right. \\ & \left. + (\mu - \gamma\beta\mu_p)E \frac{\partial}{\partial x} - (D - \gamma\beta D_p) \frac{\partial^2}{\partial x^2} \right) g_1(x, x', \omega). \end{aligned} \quad (4.54)$$

With the replacement

$$\frac{1}{\tau'} = \frac{(1 - \beta)}{\tau} + B_n[n_{T_o}^+ + \beta(n_1 + n_o)], \quad (4.55)$$

$$\mu' = \mu - \gamma\beta\mu_p, \quad (4.56)$$

$$D' = D - \gamma\beta D_p, \quad (4.57)$$

this equation becomes the same as that considered in references [4.3] and [4.4]. (The explicit solution is given as equation (12) in Ref. [4.4].) Equations (4.55) through (4.57) become the same as equations (4.45) through (4.47) if one sets  $\gamma \sim 1$  and takes the ambipolar mobility and diffusivity as nearly equal to the minority carrier values.

From the fact that  $\Theta_3(x, \omega)$  and  $\Theta_4(x, \omega)$  are numbers and from the transforms of equations (4.26) and (4.28) one sees that  $g_i(x, x', \omega)$  for  $i = 3$  and 4 must have the form

$$g_i(x, x', \omega) = g_{i0}(x, x', \omega) + \sigma_i(\omega)\delta(x - x'), \quad (4.58)$$

where  $g_{i_s}$  is nonsingular. From the transform of equation (4.28) one has

$$g_{4_s}(x, x', \omega) = \beta(\omega)g_{2_s}(x, x', \omega) \quad (4.59)$$

and

$$\Theta_3\sigma_2 + \Theta_4\sigma_4 = 1. \quad (4.60)$$

Substituting equations (4.58), (4.59), and (4.60) into the transform of equation (4.26) and integrating three times from  $x' - \epsilon$  to  $x' + \epsilon$  (where  $\epsilon$  is arbitrarily small) one finds that

$$D\sigma_2 - \gamma D_p\sigma_4 = 0. \quad (4.61)$$

Equations (4.61) and (4.57) determine  $\sigma_2$  and  $\sigma_4$

$$\sigma_2 = \frac{1}{\Theta_3 + (D/\gamma D_p)\Theta_4}, \quad (4.62)$$

$$\sigma_4 = \frac{1}{(\gamma D_p/D)\Theta_3 + \Theta_4}. \quad (4.63)$$

From the substitution into the transform of equation (4.26) one also finds that  $g_{2_s}(x, x', \omega)$  is given by

$$\begin{aligned} & -A(\omega)\delta(x - x') - (\mu\sigma_2 - \gamma\mu_p\sigma_4)E\frac{\partial}{\partial x}\delta(x - x') \\ & = \left[ i\omega + \frac{1}{\tau'} + \mu'E\frac{\partial}{\partial x} - D'\frac{\partial^2}{\partial x^2} \right] g_{2_s}(x, x', \omega), \end{aligned} \quad (4.64)$$

where

$$A(\omega) = \left[ i\omega + \frac{1}{\tau} + B_n n_{T_0}^+ \right] \sigma_2 + \left[ B_n (n_1 + n_{T_0}) - \frac{1}{\tau} \right] \sigma_4. \quad (4.65)$$

From the form of equation (4.64), it is clear that

$$g_{2s}(x, x', \omega) = -A(\omega)g_1(x, x', \omega) - (\mu\sigma_2 - \gamma\mu_p\sigma_4)Eg_b(x, x', \omega), \quad (4.66)$$

where  $g_b(x, x', \omega)$  solves

$$\frac{\partial}{\partial x} \delta(x - x') = \left( i\omega + \frac{1}{\tau'} + \mu'E \frac{\partial}{\partial x} - D' \frac{\partial^2}{\partial x^2} \right) g_b(x, x', \omega), \quad (4.67)$$

with the boundary conditions of equation (4.29).

It is quite straightforward to solve equation (4.67) for  $g_b$  and thus complete the solution for the Green's functions. However, by approximating  $\gamma \sim 1$  and taking the ambipolar mobility and diffusivities to be nearly equal to the minority carrier values, we have from equation (4.61) and the Einstein relation that

$$\mu\sigma_2 - \gamma\mu_p\sigma_4 \simeq 0 \quad (4.68)$$

and

$$\sigma_2 \simeq \sigma_4 \simeq \frac{1}{\Theta_3 + \Theta_4}. \quad (4.69)$$

Thus,  $g_b$  drops out of the problem and  $A(\omega)$  and  $\sigma(\omega)$  are given by equations (4.49) and (4.50).

Summarizing the results for the Green's functions (with the approximations  $\gamma \sim 1$ ,  $\mu \sim \mu_p$ , and  $D \sim D_p$ ) gives

$$g_3(x, x', \omega) = \beta(\omega)g_1(x, x', \omega), \quad (4.70)$$

$$g_2(x, x', \omega) = -A(\omega)g_1(x, x', \omega) + \sigma(\omega)\delta(x - x'), \quad (4.71)$$

$$g_4(x, x', \omega) = -A(\omega)\beta(\omega)g_1(x, x', \omega) + \sigma(\omega)\delta(x - x'), \quad (4.72)$$

where  $g_1(x, x', \omega)$  is found by solving equation (4.54) with boundary conditions given by equation (4.29).

In addition to the Greens's functions, the zero time correlation functions must be known. For the one-dimensional model considered, for  $n$ -type material, and taking  $n_o$  to be large compared to  $n_{T_o}^+$ ,  $p_o$ , and the excess densities, these correlation functions are [4.8]

$$\langle \Delta n(x, 0) \Delta n(x', 0) \rangle = \frac{n_T^+(x) + p(x)}{Wd} \delta(x - x'), \quad (4.73)$$

$$\langle \Delta n_T^+(x, 0) \Delta n(x', 0) \rangle = \frac{\hat{N}^+(x)}{Wd} \delta(x - x'), \quad (4.74)$$

$$\langle \Delta n(x, 0) \Delta p(x', 0) \rangle = \frac{p(x)}{Wd} \delta(x - x'), \quad (4.75)$$

and

$$\langle \Delta n_T^+(x, 0) \Delta p(x', 0) \rangle = 0. \quad (4.76)$$

Here,

$$p(x) = p_o + \Delta p(x), \quad (4.77)$$

$$\hat{N}^+(x) = n_T^+(x) \left( 1 - \frac{n_T^+(x)}{N_T} \right) \simeq n_T^+(x), \quad (4.78)$$

$$n_T^+(x) = n_{T_o}^+ + \Delta n_T^+(x), \quad (4.79)$$

and

$$\Delta p(x) = [1 - \beta(0)] \Delta n(x), \quad (4.80)$$

$$\Delta n_T^+(x) = \beta(0) \Delta n(x). \quad (4.81)$$

It has been assumed that  $n_T^+(x) \ll N_T$ .

The expression for the noise spectral density then becomes

$$\begin{aligned} G(V, \omega) = & \frac{4V^2}{n_o^2} \left( \frac{1}{Wd} \right) \left( \frac{1}{2L} \right)^2 \\ & \times \text{Re} \int_{-L}^L \int_{-L}^L [g_1(x, x', \omega) p_o + \{[1 - A(\omega)] g_1(x, x', \omega) \\ & + \sigma(\omega) \delta(x - x')\} n_{T_o}^+ + \{[1 - \beta(0) A(\omega)] g_1(x, x', \omega) \\ & + \beta(0) \sigma(\omega) \delta(x - x')\} \Delta n(x')] dx' dx. \end{aligned} \quad (4.82)$$

The background electron density,  $\Delta n(x')$ , is easily calculated from equation (4.32) by considering steady state excitation

$$\Delta n(x) = \frac{\eta Q_B}{d} \int_{-L}^L g_1(x, x', 0) dx'. \quad (4.83)$$

It remains to evaluate the spatial integrals in equation (4.82). The integral

$$Q(\omega) = \frac{1}{2L} \int_{-L}^L \int_{-L}^L g_1(x, x', \omega) dx dx' \quad (4.84)$$

is easily evaluated to give equation (4.43). The integral in the background noise contribution term can also be evaluated in a straightforward way. (It is just sums of integrals of exponentials.) However, the background noise can be more conveniently calculated by showing (with the same approximations as above) that

$$\begin{aligned} \operatorname{Re} \frac{1}{2L} \int_{-L}^L \int_{-L}^L \{ [1 - \beta(0)A(\omega)] g_1(x, x', \omega) \\ + \beta(0)\sigma(\omega)\delta(x - x') \} \Delta n(x') dx' dx \\ = -\frac{\eta Q_B}{d} \frac{\operatorname{Im}[Q(\omega)]}{\omega}. \end{aligned} \quad (4.85)$$

The proof of this result follows in exactly the same way as the analogous result without including deep-level centers (see Appendix III of Ref. [4.3]). Substituting equations (4.84) and (4.85) into equation (4.82) then gives equation (4.37) of the preceding section.

### Dependence on Trap Density and Temperature

In this section, calculations of the g-r noise voltage, responsivity, and detectivity for various values of the deep-level trap density and

temperature are presented. The calculations were performed for an  $n$ -type  $X = 0.21$   $\text{Hg}_{1-X}\text{Cd}_X\text{Te}$  photoconductor with a length of  $35 \mu\text{m}$ , width of  $50 \mu\text{m}$ , and thickness of  $10 \mu\text{m}$ . The electron and hole mobilities were taken as  $2 \times 10^5 \text{ cm}^2/\text{Vs}$  and  $500 \text{ cm}^2/\text{Vs}$ , respectively. An excess (band-to-band recombination) carrier lifetime of  $1 \mu\text{sec}$ , a quantum efficiency of unity, a shallow donor less shallow acceptor density of  $5 \times 10^{14} \text{ cm}^{-3}$  (over the temperature range considered this is essentially the electron density), and a signal wavelength of  $11 \mu\text{m}$  are assumed. The band gap as a function of temperature was taken from Ref. [4.9] and the effective density of states from Refs. [4.10] and [4.11] (consistent at this composition). The energy of the deep-level center was taken to be  $40 \text{ meV}$  above the valence band and electron and hole capture cross sections of  $\sigma_n = 10^{-15} \text{ cm}^2$  and  $\sigma_p = 10^{-17} \text{ cm}^2$  were used. These parameters are typical of  $\text{HgCdTe}$  photoconductors currently being produced. At these values of the cross sections, the effects of minority carrier trapping are very small ( $\beta \sim 0$ ). To illustrate the effects of carrier trapping, a second series of calculations have been performed with the cross-section values reversed (i.e.,  $\sigma_p = 10^{-15} \text{ cm}^2$  and  $\sigma_n = 10^{-17} \text{ cm}^2$ ). The first series of calculations are meant to represent the effects of a common deep-level center in  $\text{HgCdTe}$ , the second series of calculations are

meant to be for illustrative purposes. In the two-panel figures, the upper panel is for the HgCdTe cross-section values and the lower panel is for the reversed cross-section values.

The temperature range  $100\text{ K} \geq T \geq 50\text{ K}$  is considered. In this range, the electron density is essentially constant, but other densities change rapidly. In figure 4.1,  $p_o, p_1, n_1, n_i,$  and  $n_{T_o}^+$  for three values of  $N_T$  are plotted as a function of  $100/T$ . Notice in particular that  $p_o$  drops with temperature at a much faster rate than  $n_{T_o}^+$ . Although this is obvious, it is important because the deep levels add a thermal noise source with a strength proportional to  $n_{T_o}^+$  whereas the band-to-band thermal noise source is proportional to  $p_o$ . The temperature at which the  $p_o$  and  $n_{T_o}^+$  curves cross depends on  $N_T$ . The deep-level thermal noise source can become important at the lower temperatures. Also notice that  $p_1$  is rather large, much larger than  $n_1$ . This occurs because the hole effective density of states is much larger than the electron effective density of states and indicates that hole thermal emission rates can be fairly high.

In figure 4.2,  $\beta$  is shown at low frequency as a function of  $100/T$  for several values of  $N_T$  and both sets of cross section values. The upper panel is for the HgCdTe cross-section values and the lower panel is for

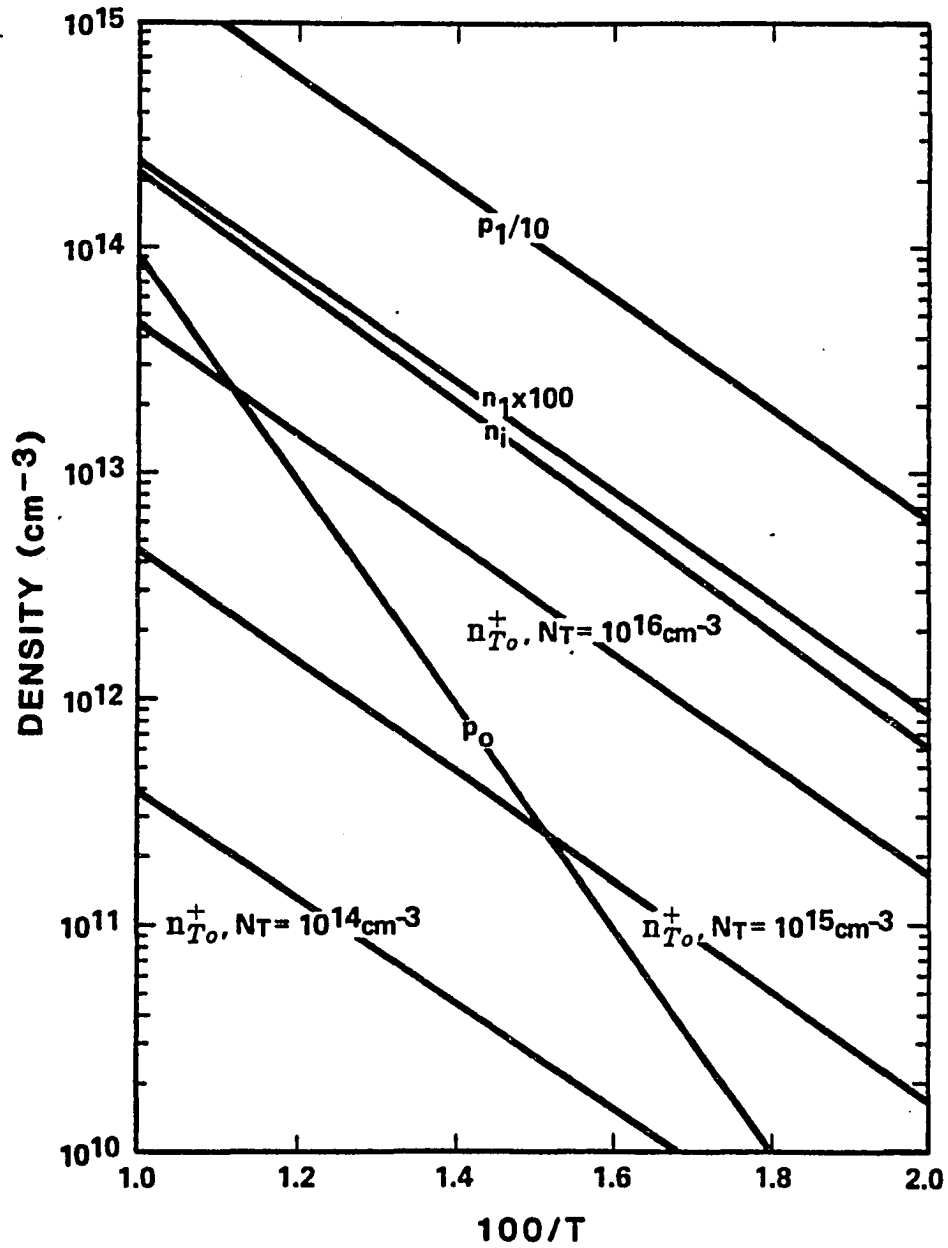


Figure 4.1: A plot of the log of several carrier densities as a function of  $100/T$ .

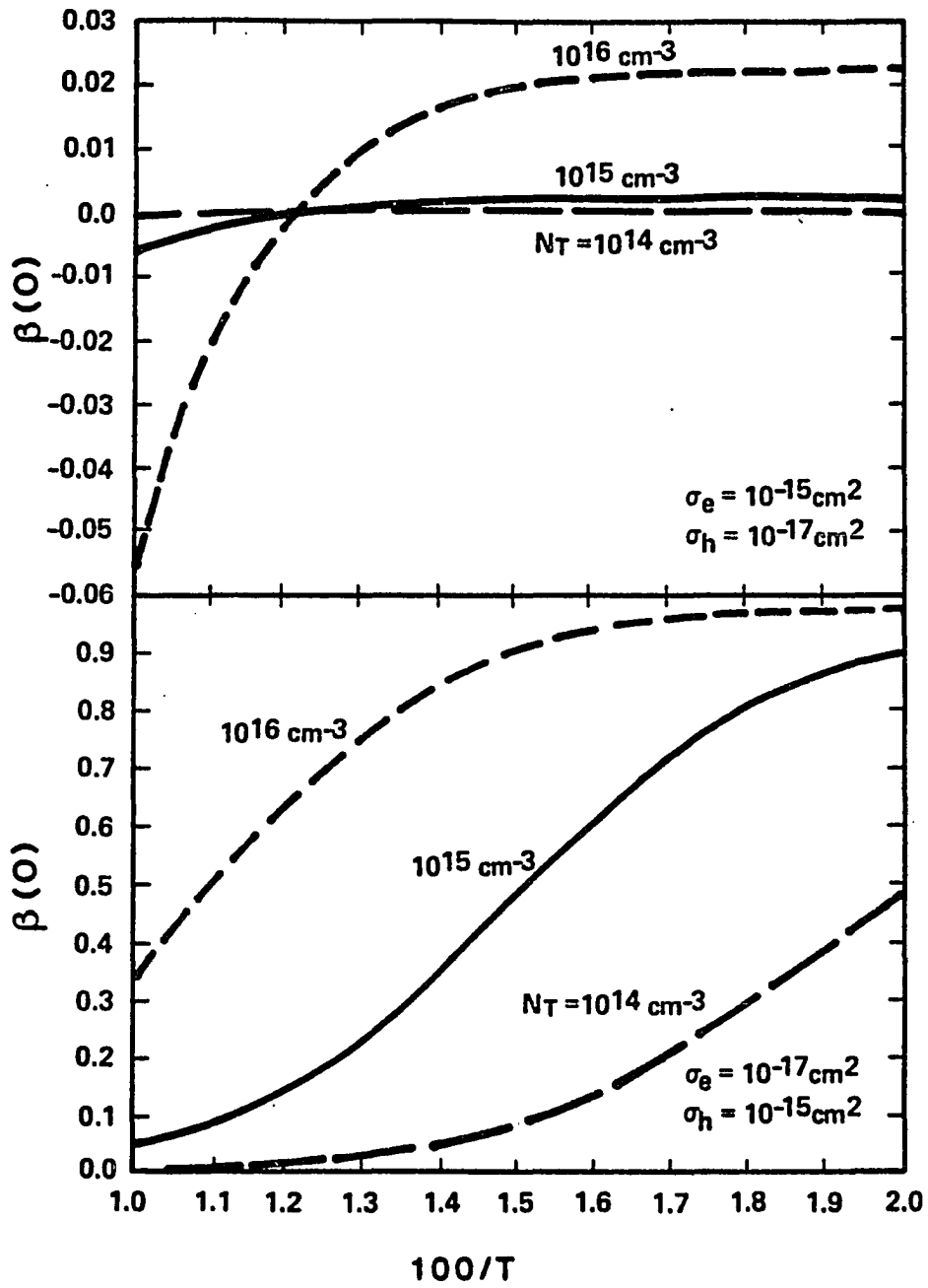


Figure 4.2: The function  $\beta$  at low frequency as a function of  $100/T$  for three values of the deep-level density.

the reversed cross-section values.  $\beta$  gives the degree of minority carrier trapping. (Negative values correspond to predominant electron trapping.) For the cross-section values corresponding to HgCdTe,  $\beta$  is very small, indicating little trapping. For the reversed set of cross-section values,  $\beta$  approaches unity as the temperature decreases indicating a high degree of hole trapping in this case. The fact that there is little trapping for the HgCdTe set of cross-section values and a high degree of hole trapping for the reversed set of cross-section values suggests that these cases will behave rather differently.

Deep-level centers can change the responsivity both by decreasing the carrier lifetime by SRH recombination and by minority carrier trapping which reduces the effective mobility and diffusivity. In figure 4.3, the responsivity is shown as a function of the bias field for two values of the deep-level center density and the two sets of cross-section values. For the HgCdTe cross-section values, the responsivity decreases a little as the center density increases. There is very little trapping in this case and the decrease in responsivity results from SRH recombination. However, the responsivity is largely limited by carrier sweep-out effects and a small decrease in carrier lifetime does not have much effect. For the reversed cross-section values,

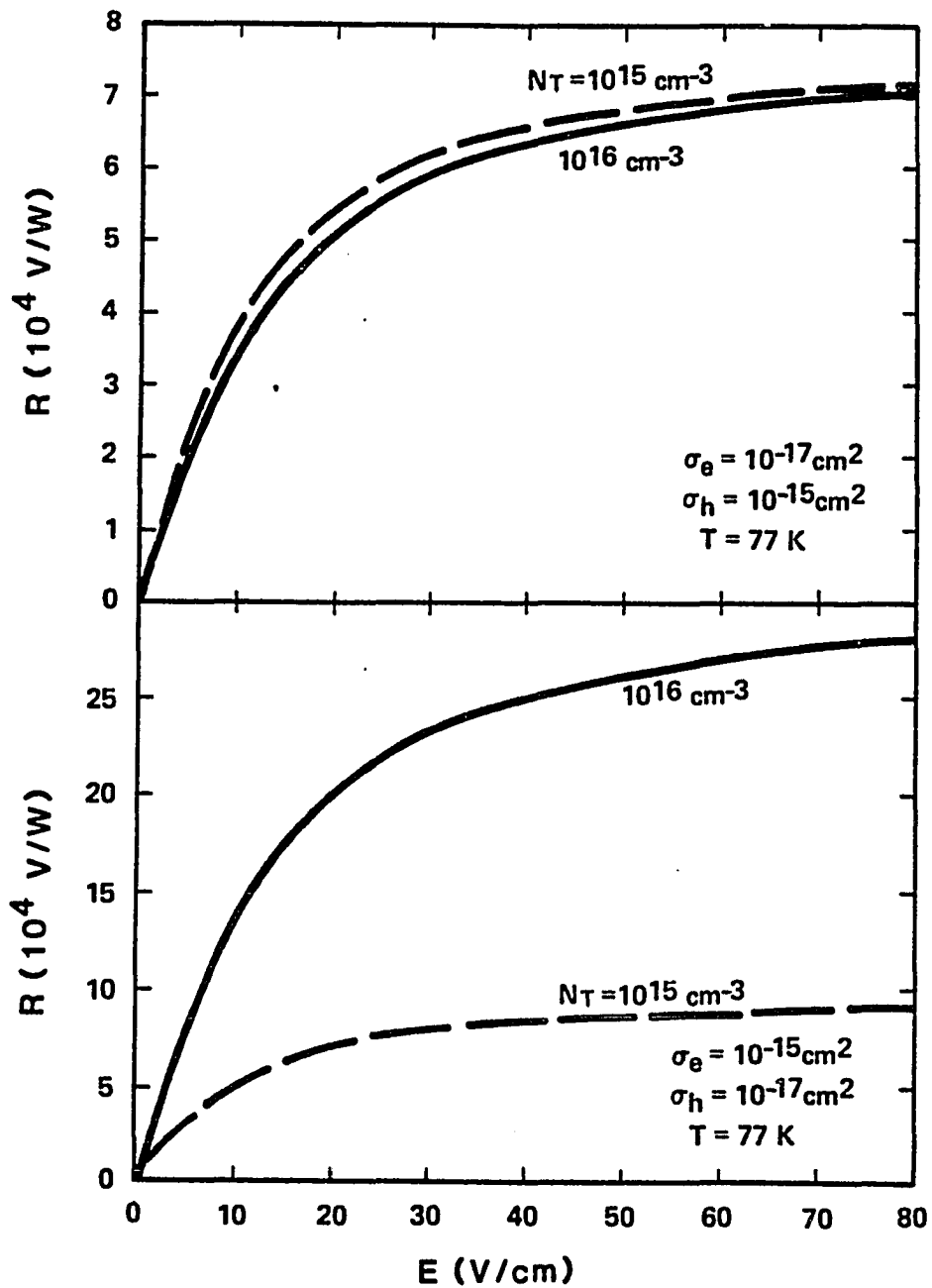


Figure 4.3: Responsivity at two values of the deep-level density as a function of the bias field.

there is a high degree of minority carrier trapping and the mobility and diffusivity are significantly reduced. As a result, sweep out is reduced and responsivity is increased by the minority carrier trapping centers.

In figure 4.4, the three noise components are shown at a temperature of 77 K as a function of bias for the two sets of cross section values. In figure 4.5, these noise components are shown at a bias field of 40 V/cm as a function of  $100/T$ . The total noise voltage is found by adding the three components quadratically [see equation (4.37)]. For the HgCdTe cross-section values, the background noise component increases linearly with field at small fields and saturates at larger fields. The band-to-band thermal component increases linearly with increasing field at small fields and like the square root of field at high fields. This behavior is the same as occurs without the deep-level centers and has been discussed previously [4.3]. The trap component of the thermal noise increases linearly with increasing bias showing that this noise component is not strongly influenced by carrier sweep out. For the reversed cross-section values, minority carrier trapping is significant, but not complete at 77 K. The background and band-to-band thermal noise components have a field dependence similar to that for the HgCdTe cross-section values but because the effective

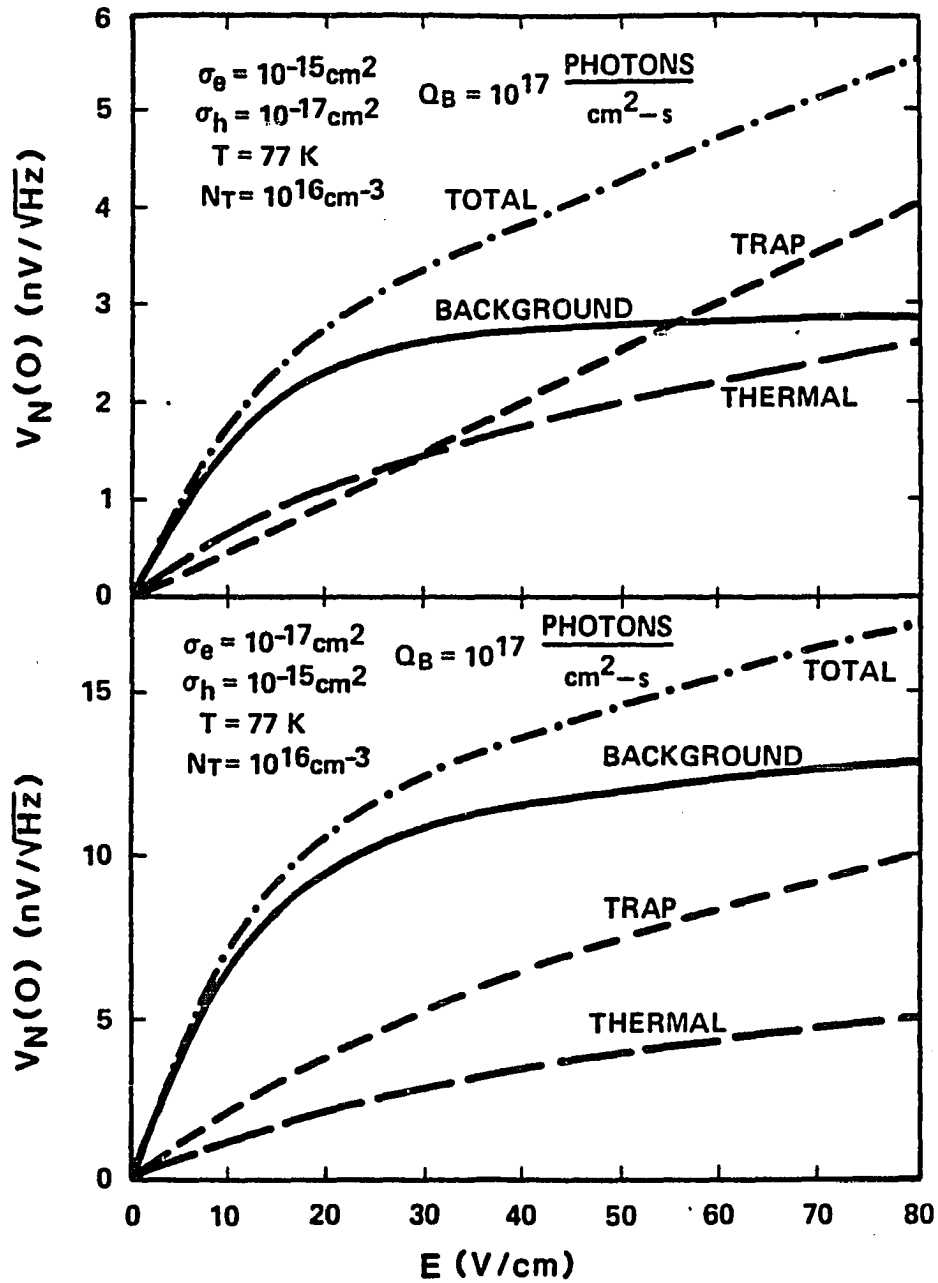


Figure 4.4: The three noise voltage components and the total noise voltage as a function of the bias field.

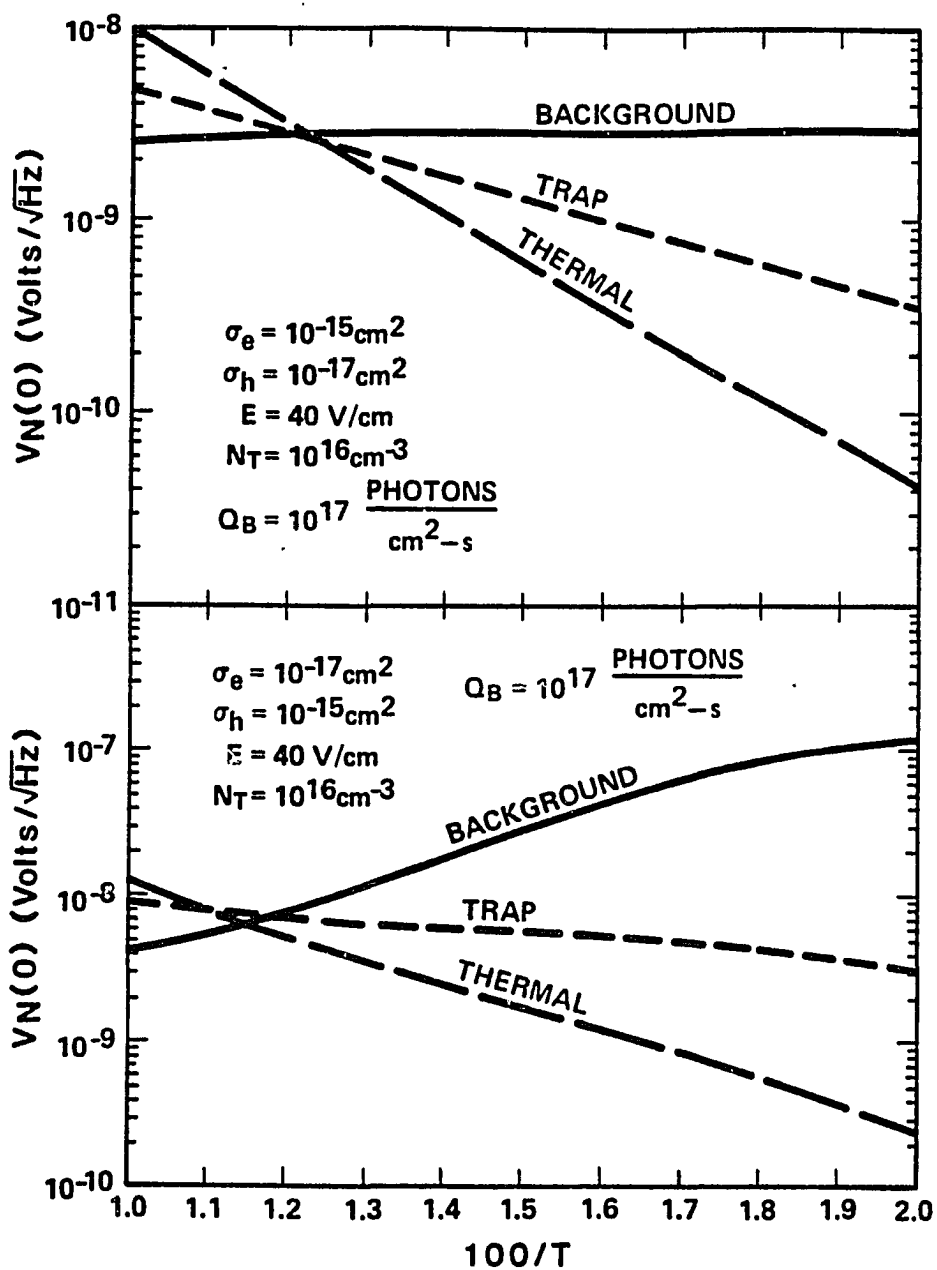


Figure 4.5: A log plot of the three noise voltage components as a function of  $100/T$ .

mobility and diffusivity are smaller, owing to minority carrier trapping, the noise is larger and the saturation with bias field occurs at higher fields. The trap component of the noise increases at a rate which is sublinear with increasing bias field.

For the HgCdTe cross-section values, the background noise component and the trap component both decrease with decreasing temperature but the band-to-band thermal contribution decreases at a faster rate. These two components largely follow  $p_o$  and  $n_{T_o}^+$ , respectively. For the reversed cross-section values, the minority carrier trapping decreases the effective mobility. As a result, sweep-out effects become less important at low temperature. Thus, the background noise component increases with decreasing temperature. The band-to-band thermal and trap noise components decrease with decreasing temperature (because  $p_o$  and  $n_{T_o}^+$  are decreasing) but at a slower rate than for the case where minority carrier trapping is unimportant.

From figure 4.5, it is seen that; at a trap density of  $10^{16} \text{ cm}^{-3}$ , a temperature of 77 K, a bias of 40 V/cm, and  $X = 0.21$ ; the trap component of the noise is slightly greater than the band-to-band thermal noise and slightly less than the background contribution for a background flux of  $10^{17}$

photons/cm<sup>2</sup>/s. Thus, under these conditions, the detector  $D^*$  will be fairly close to the background limited value and the presence of deep-level centers will have degraded the detector performance only modestly. However, if lower background applications are considered (perhaps at lower detector operating temperature) the presence of deep-level centers can become quite important.

In figure 4.6,  $D^*$  is shown as a function of deep-level center density for three values of the background flux. For a background flux  $10^{17}$  photons/cm<sup>2</sup>/s,  $D^*$  is not significantly degraded by the deep-level centers until their density exceeds about  $10^{16}$  cm<sup>-3</sup>. At lower background fluxes, however,  $D^*$  begins to degrade at lower trap densities. For the reversed cross-section value case,  $D^*$  shows a somewhat more complex behavior. There is an initial small drop at a trap density of  $\sim 10^{15}$  cm<sup>-3</sup> and a larger drop as the trap density exceeds a few times  $10^{16}$  cm<sup>-3</sup>. In the calculations in figure 4.6, Johnson noise has not been included. For comparison, the Johnson noise for the detector parameters considered at 77 K is  $4 \times 10^{-10}$  V/ $\sqrt{\text{Hz}}$ .

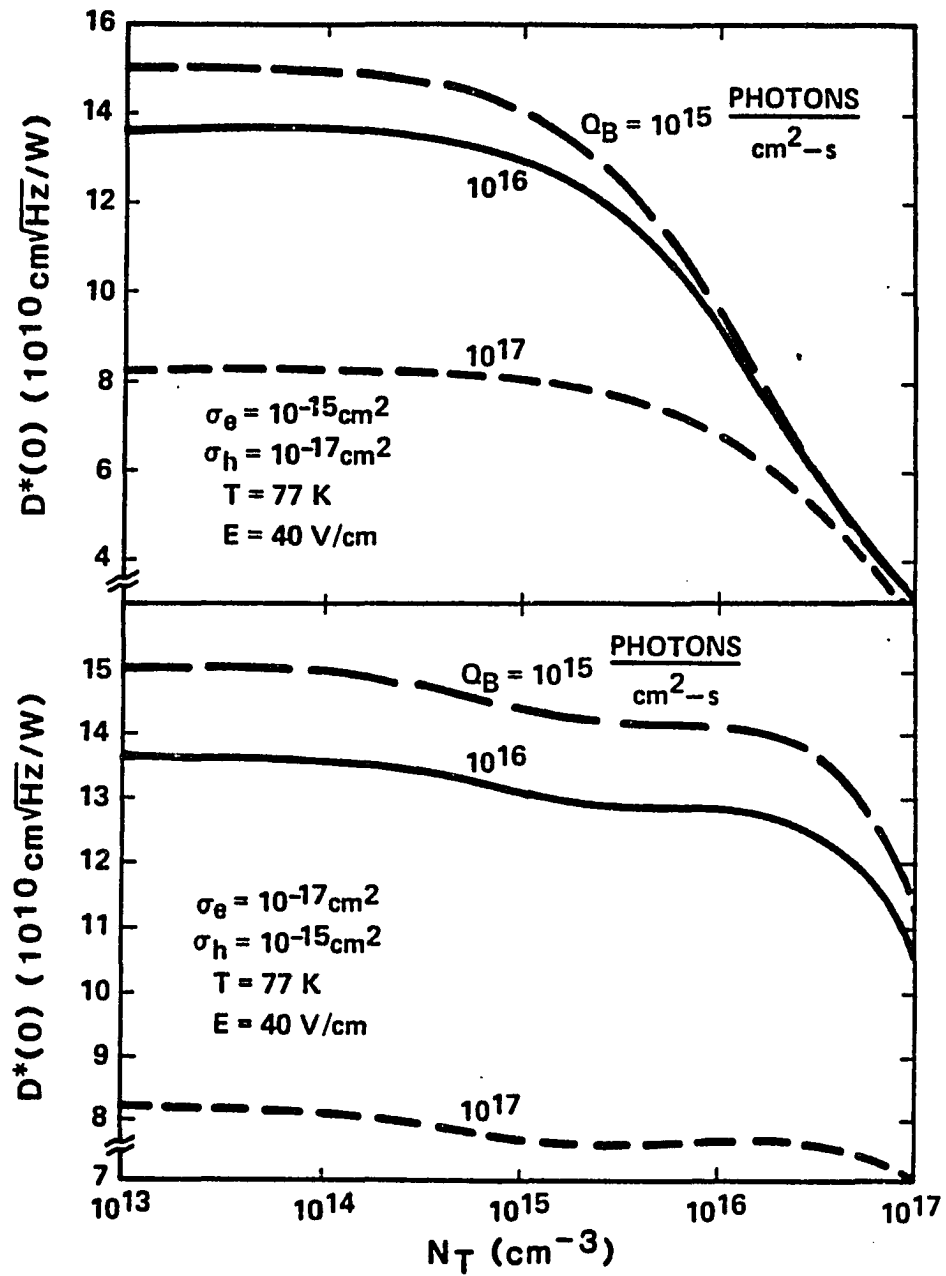


Figure 4.6: Detectivity for three values of the background photon flux as a function of the deep-level density.

The dependence of the three components of the noise voltage on frequency for the two sets of cross-section values are shown in figure 4.7. The three components begin to roll off at approximately the same frequency. For the reversed cross-section values, the roll off occurs at lower frequencies than for the HgCdTe cross-section values because minority carrier trapping reduces the effect of sweep out for the reversed cross-section case.

### Conclusion

In this chapter, a theory of the effect of deep-level centers on the g-r noise and responsivity of an intrinsic photoconductor has been presented. It is found that deep-level centers can influence the g-r noise in three main ways: (i) They can shorten the bulk excess carrier lifetime by Shockley-Read-Hall recombination. (ii) If the minority carrier capture rates are significantly larger than the majority carrier rates, they can trap the photogenerated minority carriers. This trapping reduces the effective minority carrier mobility and diffusivity and thus reduces the effect of carrier sweep out. (iii) The deep-level centers add a new thermal noise source which results from fluctuations between bound and free carriers. A series of calculations were performed for a  $X = 0.21$ ,  $n$ -type  $\text{Hg}_{1-X}\text{Cd}_X\text{Te}$

---

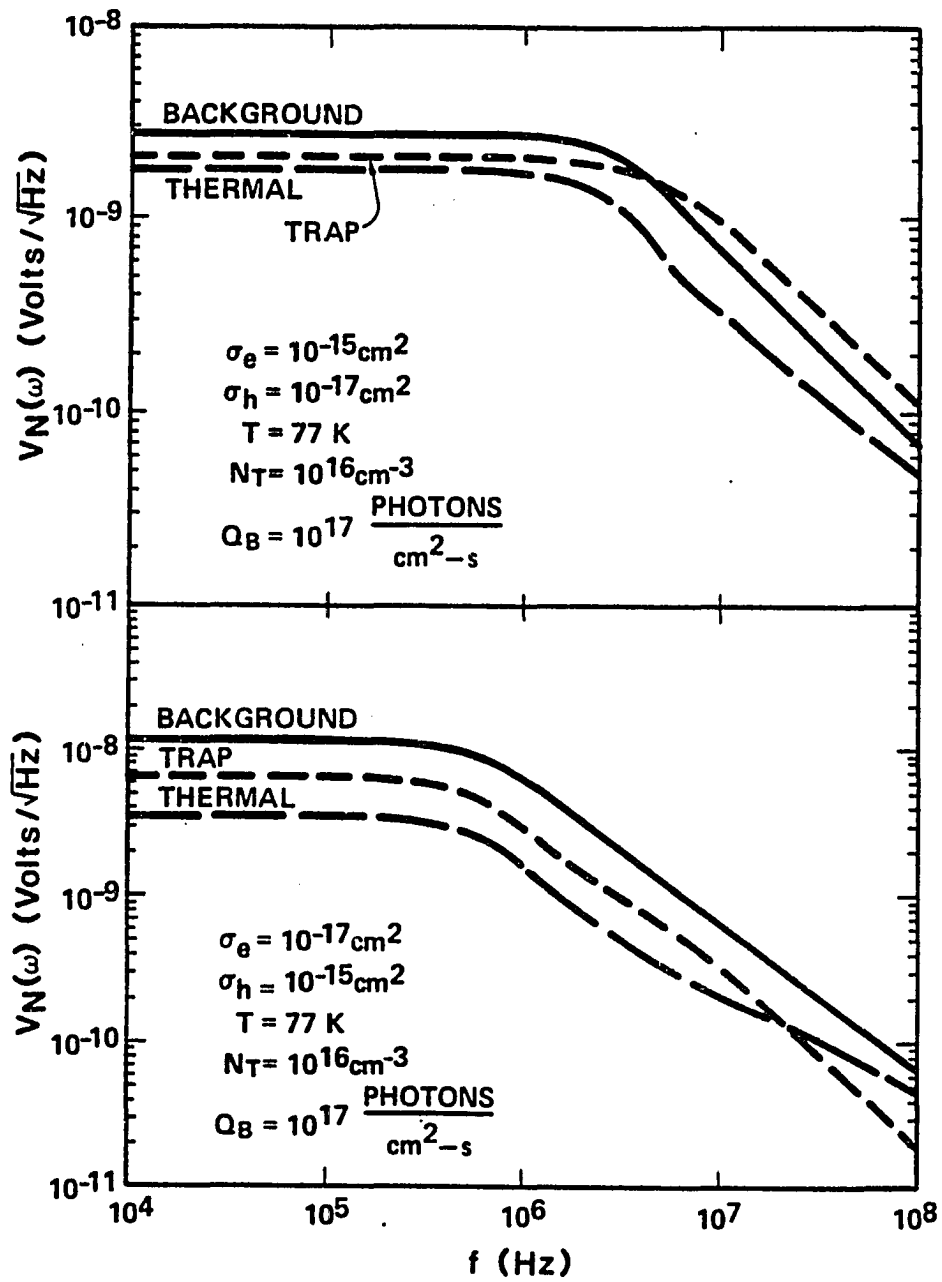


Figure 4.7: A log-log plot of the three noise voltage components as a function of frequency.

photoconductor using the parameters of a commonly occurring deep-level center [4.6] in this material. It is found that for typical bias, background, and temperature operating conditions (40 V/cm bias,  $10^{17}$  photons/cm<sup>2</sup>/s background, and  $T = 77$  K) detector performance begins to degrade as the deep-level center density begins to exceed  $10^{16}$  cm<sup>-3</sup>. For the deep level parameters in *n*-type HgCdTe there is little minority carrier trapping. (The majority carrier cross section is much larger than the minority carrier cross section.) To illustrate the effects of trapping, calculations were also performed in which the cross sections of the two carrier types were reversed from the physical HgCdTe values.

## CHAPTER 5

### NONLINEAR, TIME-DEPENDENT PHOTOCONDUCTIVE DEVICE MODELING

In this chapter a one spatial dimension, photoconductive device model that is based on the time-dependent, convective/diffusive transport equations derived in chapter 2 is presented. Electron and hole trapping on deep-level impurities is accounted for by trapping-kinetics rate equations. The coupling between carrier drift and electric field is completed through Poisson's equation. The model equations are solved numerically with boundary conditions that represent ideal ohmic contacts. Computed results are presented for different photoconductor lengths and bias voltages with spatially uniform, rectangular light-pulse excitation. Material parameters appropriate for iron-doped indium phosphide are used.

#### Introduction

A photoconductor, consisting of a piece of homogeneous semiconductor material on which two electrical contacts have been made, is possibly

the simplest semiconductor device. Photoconductors find applications in a variety of areas, such as high-speed signal sampling [5.1, 5.2, 5.3, 5.4, 5.5], radiation detection [5.6, 5.7], and high-voltage pulse-power switching [5.8]. A wide variety of different semiconductor materials have been used for photoconductor applications. For most applications it is desirable to use a high resistivity material so that the dark current will be low, therefore, semi-insulating semiconductors are widely used. Semiconductors are made semi-insulating by introducing a relatively large density of deep-level impurities into the material, which causes the Fermi energy level to be pinned near the center of the band gap and, thus, the number of thermally produced electron-hole pairs is relatively low. The deep-level impurities in the semiconductor also act as trapping and recombination centers, thus affecting the response of the photoconductor.

Depending upon the application, photoconductors can take on a variety of different sizes and geometrical forms. In most cases the geometrical characteristic of the photoconductor that most affects the response is the gap length, defined as the distance between the electrical contacts. Photoconductors can range in size from a few micrometers for devices used in high-speed sampling applications to a few centimeters in pulse-power

---

applications. The geometry of a photoconductor may be that of a gap in a microstrip transmission line constructed using the semiconductor as the dielectric. For pulse-power and radiation-detector applications, the photoconductor may consist of a block of semiconductor material with the electrical contacts fabricated on two opposite faces of the block.

The time-dependent response of a photoconductor will depend upon the characteristics of the semiconductor material, the geometry of the photoconductor, the properties of the electrical contacts, the characteristics of the electrical circuit connected to the photoconductor, and the characteristics of the excitation source. In this chapter, a photoconductor made from a semi-insulating semiconductor material with a single, deep-level impurity is considered. An example of such a material is iron-doped indium phosphide (InP:Fe). Iron in indium phosphide is a deep, acceptor-like impurity with a single energy level and two charge states, neutral and negative. In chapter 3, the transient bulk-material response of InP:Fe was studied using a simple, trapping-kinetics rate equation model. In this chapter that work is greatly extended to include convective/diffusive transport and space-charge effects on the photoconductive response. The work in chapter 3 can be considered to be a model of the intrinsic material

---

response, whereas this work represents a complete photoconductive device model.

A photoconductor is essentially a one-dimensional device in terms of current flow, so second-order effects occurring in the direction perpendicular to the equilibrium electric field are not considered here. It is assumed that the electrical contacts have an infinite surface recombination velocity that keeps the carrier densities at the contacts at thermal equilibrium. A fixed potential difference applied to the photoconductor, representing a low-impedance external circuit, is also assumed. Computed results are presented for spatially uniform, rectangular excitation pulses with a duration suitable to illustrate the photoconductor rise and fall characteristics.

This chapter is organized as follows: In the second section, time-dependent model equations for a photoconductor with a single type of deep-level impurity are formulated; in the third section, the numerical approach used to solve the nonlinear system of model equations is discussed; in the fourth section, a series of computed results are presented; in the fifth section, experimental data that shows features which can be understood in terms of the model results is presented; and I conclude in the sixth section.

---

### The Model Equations

The dynamics of transient photoconductivity are assumed to be adequately described by continuity equations for electrons and holes, rate equations for trapping kinetics, drift/diffusion current equations, and Poisson's equation. From chapter 2, the continuity equations for electrons and holes are

$$\frac{\partial n}{\partial t} = g(\mathbf{r}, t) - R_n(\mathbf{r}, t) + \frac{1}{q} \nabla \cdot \mathbf{J}_n \quad (5.1)$$

and

$$\frac{\partial p}{\partial t} = g(\mathbf{r}, t) - R_p(\mathbf{r}, t) - \frac{1}{q} \nabla \cdot \mathbf{J}_p, \quad (5.2)$$

where  $n(\mathbf{r}, t)$  and  $p(\mathbf{r}, t)$  denote electron and hole densities,  $g(\mathbf{r}, t)$  is the electron-hole-pair photogeneration rate,  $R_n(\mathbf{r}, t)$  and  $R_p(\mathbf{r}, t)$  are the electron and hole reduction rates caused by trapping on deep-level impurities,  $q$  is the electronic charge, and  $\mathbf{J}_n(\mathbf{r}, t)$  and  $\mathbf{J}_p(\mathbf{r}, t)$  are the electron and hole current densities. For the InP:Fe model system, the sum of the density of iron sites in the neutral charge state,  $n_T^0$ , and the negative charge state,  $n_T^-$ , is equal to the total density,  $N_T$ , of iron sites.

$$n_T^0 + n_T^- = N_T \quad (5.3)$$

Only a single continuity equation for trapping kinetics is required. It can be written in terms of negatively charged trapping sites (trapped electrons) as

$$\frac{\partial n_T^-}{\partial t} = R_n(\mathbf{r}, t) - R_p(\mathbf{r}, t). \quad (5.4)$$

The electron and hole current densities are given as follows, using the drift/diffusion model which is derived from the Boltzmann transport equation:

$$\mathbf{J}_n = q(\mu_n \mathbf{E}n + D_n \nabla n), \quad (5.5)$$

$$\mathbf{J}_p = q(\mu_p \mathbf{E}p - D_p \nabla p), \quad (5.6)$$

where  $\mu_n$  and  $\mu_p$  are the electron and hole mobilities,  $\mathbf{E}$  is the electric field, and  $D_n$  and  $D_p$  are the electron and hole diffusivities. Poisson's equation couples the transport of electrons and holes through the electric-field-driven convection (drift) component of the current densities; it is written as

$$\nabla^2 \psi = -\nabla \cdot \mathbf{E} = -\frac{q}{\epsilon}(p - n - n_T^- + N_D^+ - N_A^-), \quad (5.7)$$

where  $\psi$  is the electric potential ( $\mathbf{E} = -\nabla \psi$ ),  $\epsilon$  is the static dielectric constant of the material, and  $N_D^+$  and  $N_A^-$  are the shallow donor and acceptor doping densities (assumed to be spatially uniform).

The rate of carrier reduction, caused by trapping of electrons and holes on the deep-level impurity sites, is modeled as being proportional to the product of the free carrier density and the number of available trapping sites on which that carrier type can be captured. Thus the carrier reduction rates are written as

$$R_n = B_n n n_T^o \quad (5.8)$$

and

$$R_p = B_p p n_T^-, \quad (5.9)$$

where

$$B_n = \langle v_n \rangle \sigma_n \quad (5.10)$$

and

$$B_p = \langle v_p \rangle \sigma_p. \quad (5.11)$$

Here  $\langle v_n \rangle$  and  $\langle v_p \rangle$  are the electron and hole thermal velocities, and  $\sigma_n$  and  $\sigma_p$  are the electron and hole capture cross sections of the trapping sites. Thermal emission of electrons and holes from deep-level sites at room temperature occurs at a slow rate. This thermalization process is not included in the model equations because it is not important on the time scales considered in this chapter.

The equations can be written in terms of excess densities,  $\Delta n$ ,  $\Delta p$ , and  $\Delta n_T^-$ , which represent deviations from the densities at thermal equilibrium. In the case of transient photoconductivity in semi-insulating semiconductors, the excess electron and hole densities are large compared to their thermal-equilibrium values. Detailed balance and charge neutrality are applied to the equations at thermal equilibrium [ $g(\mathbf{r}, t) \equiv 0$ ] and, with the small thermal-equilibrium electron and hole densities neglected, equations (5.1)–(5.9) can be written as a system of four equations in one spatial dimension.

$$\frac{\partial \Delta n}{\partial t} = g(x, t) - B_n(N_T - n_{T_0}^- - \Delta n_T^-)\Delta n + \mu_n \left[ \frac{\partial(E\Delta n)}{\partial x} + \frac{kT}{q} \frac{\partial^2 \Delta n}{\partial x^2} \right] \quad (5.12)$$

$$\frac{\partial \Delta p}{\partial t} = g(x, t) - B_p(n_{T_0}^- + \Delta n_T^-)\Delta p + \mu_p \left[ -\frac{\partial(E\Delta p)}{\partial x} + \frac{kT}{q} \frac{\partial^2 \Delta p}{\partial x^2} \right] \quad (5.13)$$

$$\frac{\partial \Delta n_T^-}{\partial t} = B_n(N_T - n_{T_0}^- - \Delta n_T^-)\Delta n - B_p(n_{T_0}^- + \Delta n_T^-)\Delta p \quad (5.14)$$

$$\frac{\partial^2 \psi}{\partial x^2} = -\frac{\partial E}{\partial x} = -\frac{q}{\epsilon}(\Delta p - \Delta n - \Delta n_T^-) \quad (5.15)$$

Here,  $n_{T_0}^-$  is the thermal-equilibrium density of negatively charged trapping sites and Einstein's relation,  $D_{n,p} = \frac{kT}{q} \mu_{n,p}$ , has been used.

To complete the mathematical description of the problem, boundary conditions and initial conditions must be specified. The one-dimensional

photoconductive device model being considered has the electrical contacts as boundaries. The contacts are taken to be located at  $x = 0$  and  $x = L$ . With the assumption of ideal ohmic contacts with an infinite surface recombination velocity, the densities of electrons and holes at the electrical contacts are taken to be at thermal equilibrium, i.e., their excess densities are zero. The initial conditions for the excess electron and hole densities are zero as well.

$$\Delta n(0,t) = 0 \quad , \quad \Delta n(L,t) = 0 \quad (5.16)$$

$$\Delta n(x,0) = 0 \quad (5.17)$$

$$\Delta p(0,t) = 0 \quad , \quad \Delta p(L,t) = 0 \quad (5.18)$$

$$\Delta p(x,0) = 0 \quad (5.19)$$

Boundary conditions on equation (5.14) are not required because this equation is an auxiliary rate equation for trapped (nonmobile) electrons and does not contain any explicit spatial coupling. The initial condition for this equation is that the excess density of negatively charged trapping sites is zero.

$$\Delta n_T^-(x,0) = 0 \quad (5.20)$$

An arbitrary reference point for electric potential can be chosen because the

coupling to the drift current is in terms of  $E = -\partial\psi/\partial x$  and not in terms of  $\psi$  itself. The left electrical contact ( $x = 0$ ) is chosen as the electric potential reference point and a voltage of  $-V_o$  is applied to the photoconductor at  $x = L$ . Because the photoconductor is homogeneous and semi-insulating, the initial potential profile is linear, i.e., the initial electric field is constant.

$$\psi(0, t) = 0 \quad , \quad \psi(L, t) = -V_o \quad (5.21)$$

$$\psi(x, 0) = -V_o \frac{x}{L} \quad , \quad E(x, 0) = \frac{V_o}{L} \quad (5.22)$$

The photoconductive-device model equations (5.12)–(5.15) are a nonlinearly coupled, parabolic/elliptic system of partial differential equations. One source of nonlinear coupling occurs through the electric field and the carrier densities in the convective (drift) term, and through Poisson's equation. This coupling works against charge separation of the electron and hole densities by changing the drift force on the electrons and holes through the electric field. Note that the density of negatively charged deep-level impurities is present in Poisson's equation and therefore the electric field is also influenced by the charge that is "locked" onto the deep levels as trapped electrons and holes. The sensitivity of the electric field to the electron and hole densities is much greater here than in the usual device

problems where the doping density profile of the device structure sets up an operating electric field condition.

Another source of coupling occurs through the trapping of electrons and holes on the deep-level impurities, as represented by the nonlinear "damping" terms in equations (5.12) and (5.13) and by the auxiliary rate equation (5.14). This coupling is quadratic in the specific case of InP:Fe and would be quadratic for other more complicated cases as well. In general there would be more deep-level states, and more auxiliary rate equations would be required. If Poisson's equation (5.14) and the divergence of current density terms in equations (5.12) and (5.13) are dropped under the assumption of spatial uniformity and charge neutrality; the bulk-material-response, trapping-kinetics rate equation model used in chapter 3 is recovered.

Another important observation about the equations is the relative magnitude of the convective (drift) component of the current density compared to that of the diffusion component. It appears that the drift current component will dominate the diffusion current component because  $\frac{kT/q}{V_o}$  is a small parameter for most cases of interest. However, because the electric field can vary considerably and sharp density profiles can result, there may

be regions in the photoconductor where the diffusion current component will be equal to or greater than the drift current component. Mathematically this feature is referred to as a singular perturbation of the equations, which results in "boundary layer" behavior.

A conservation law exists for this system of equations in the form of a spatial invariant that is the total current density  $J_T(t)$ . This invariance can be shown by taking the time derivative of Poisson's equation (5.15) and substituting the three continuity equations (5.12), (5.13), and (5.14) into the right-hand side. This results in the expression

$$\frac{\partial}{\partial x} \left[ J_n + J_p + \epsilon \frac{\partial E}{\partial t} \right] = 0, \quad (5.23)$$

which leads to the definition of the total current density as

$$J_T(t) = J_n(x, t) + J_p(x, t) + J_D(x, t), \quad (5.24)$$

where

$$J_D = \epsilon \frac{\partial E}{\partial t} \quad (5.25)$$

is the electromagnetic displacement current density. This spatial invariant property of the total current density, which is the one-dimensional form of  $\nabla \cdot \mathbf{J}_T = 0$ , will be used as a check of the accuracy of the numerical solutions.

Another important result is found by integrating equation (5.24) across the length of the photoconductor. The homogeneous Dirichlet boundary conditions on the excess electron and hole densities and the fixed bias voltage applied to the photoconductor are used in the derivation of this result. The result can be written as

$$J_T(t) = \frac{q}{L} \int_0^L E(x,t) [\mu_n n(x,t) + \mu_p p(x,t)] dx. \quad (5.26)$$

This integral form provides an alternate way of computing the total current density other than by summing the three current components at a given point.

In preparation for the task of solving this problem numerically, the equations are put into dimensionless form. The nondimensionalization of the independent variables of equations (5.12)–(5.15) is performed by normalizing the position  $x$  to the device length  $L$  and by normalizing the time  $t$  to a free parameter  $\tau$ , which is taken to be equal to 1 ns for the results presented in this chapter. The driving term is written as  $g(x,t) = g_o \eta(x) \phi(t)$ , where  $g_o = \max[g(x,t)]$  is the maximum electron-hole pair photogeneration rate and  $0 \leq \eta(x), \phi(t) \leq 1$  gives the spatial profile and temporal shape of the applied radiation pulse. (In general,  $g(x,t)$  may not be separable

which causes no problems.) The excess electron and hole densities are then normalized to  $g_o\tau$ . A density constant  $N$  is used to normalize the excess negatively charged trap density. The value of  $N$  is taken to be  $10^{15} \text{ cm}^{-3}$  for the results presented in this chapter.

The electric potential  $\psi$  is normalized to the applied voltage  $V_o$  and, therefore, the electric field is normalized to  $V_o/L$ . This results in the current densities being normalized to  $qLg_o$ . The parameters  $\tau$  and  $N$  could be defined in terms of photoconductor physical characteristics, but they have been left as free parameters to allow greater flexibility in the scaling for the numerical computations. Using the five constants  $g_o, \tau, N, V_o$ , and  $L$  the dimensionless model equations corresponding to equations (5.12)–(5.15) and the associated boundary and initial conditions corresponding to equations (5.16)–(5.22) can be written as

$$\frac{\partial \hat{n}}{\partial \hat{t}} = \eta(\hat{x})\phi(\hat{t}) - \hat{N}_T \hat{B}_n (1 - C - \hat{n}_T^-) \hat{n} + \frac{\partial \hat{J}_n}{\partial \hat{x}}, \quad (5.27)$$

$$\hat{J}_n = \hat{\mu}_n \left( \hat{E} \hat{n} + \sigma \frac{\partial \hat{n}}{\partial \hat{x}} \right), \quad (5.28)$$

$$\frac{\partial \hat{p}}{\partial \hat{t}} = \eta(\hat{x})\phi(\hat{t}) - \hat{N}_T \hat{B}_p (C + \hat{n}_T^-) \hat{p} - \frac{\partial \hat{J}_p}{\partial \hat{x}}, \quad (5.29)$$

$$\hat{J}_p = \hat{\mu}_p \left( \hat{E} \hat{p} - \sigma \frac{\partial \hat{p}}{\partial \hat{x}} \right), \quad (5.30)$$

$$\frac{\partial \hat{n}_T^-}{\partial \hat{t}} = I \left[ \hat{B}_n (1 - C - \hat{n}_T^-) \hat{n} - \hat{B}_p (C + \hat{n}_T^-) \hat{p} \right], \quad (5.31)$$

$$\frac{\partial^2 \hat{\psi}}{\partial \hat{x}^2} = -Q \left[ I(\hat{p} - \hat{n}) - \hat{N}_T \hat{n}_T^- \right], \quad (5.32)$$

$$\hat{E} = -\frac{\partial \hat{\psi}}{\partial \hat{x}}, \quad (5.33)$$

$$\hat{n}(0, \hat{t}) = 0 \quad , \quad \hat{n}(1, \hat{t}) = 0, \quad (5.34)$$

$$\hat{p}(0, \hat{t}) = 0 \quad , \quad \hat{p}(1, \hat{t}) = 0, \quad (5.35)$$

$$\hat{\psi}(0, \hat{t}) = 0 \quad , \quad \hat{\psi}(1, \hat{t}) = -1, \quad (5.36)$$

$$\hat{n}(\hat{x}, 0) = 0, \quad (5.37)$$

$$\hat{p}(\hat{x}, 0) = 0, \quad (5.38)$$

$$\hat{n}_T^-(\hat{x}, 0) = 0, \quad (5.39)$$

$$\hat{\psi}(\hat{x}, 0) = -\hat{x} \quad , \quad \hat{E}(\hat{x}, 0) = 1, \quad (5.40)$$

where the dimensionless variables and parameters are

$$\hat{t} = \frac{t}{\tau}, \quad (5.41)$$

$$\hat{x} = \frac{x}{L}, \quad (5.42)$$

$$\hat{n} = \frac{\Delta n}{g_0 \tau}, \quad (5.43)$$

$$\hat{p} = \frac{\Delta p}{g_0 \tau}, \quad (5.44)$$

$$\hat{n}_T^- = \frac{\Delta n_T^-}{N_T}, \quad (5.45)$$

$$\hat{\psi} = \frac{\psi}{V_o}, \quad (5.46)$$

$$\hat{E} = \frac{E}{V_o/L}, \quad (5.47)$$

$$I = \frac{g_o\tau}{N}, \quad (5.48)$$

$$\hat{N}_T = \frac{N_T}{N}, \quad (5.49)$$

$$C = \frac{n_{T_o}^-}{N_T}, \quad (5.50)$$

$$\hat{B}_n = N\tau B_n, \quad (5.51)$$

$$\hat{B}_p = N\tau B_p, \quad (5.52)$$

$$\hat{\mu}_n = \frac{\mu_n V_o\tau}{L^2}, \quad (5.53)$$

$$\hat{\mu}_p = \frac{\mu_p V_o\tau}{L^2}, \quad (5.54)$$

$$\sigma = \frac{kT/q}{V_o}, \quad (5.55)$$

$$Q = \frac{qNL^2}{\epsilon V_o}. \quad (5.56)$$

Note that the electron and hole densities are nondimensionalized by  $g_o\tau$  but that the density of negatively charged deep-level impurities is nondimensionalized by  $N_T$ .

### The Numerical Solution Method

The nondimensionalized photoconductive-device model equations with the boundary and initial conditions are solved numerically. The numerical technique used is based on a finite-difference spatial semidiscretization of the nondimensionalized system of equations. The exponentially weighted, upwind-differencing scheme of Scharfetter and Gummel [5.9] is used in the discretization of the terms for the divergence of the current density. The spatial semidiscretization yields a system of nonlinearly coupled, first-order ordinary differential equations in time and algebraic equations resulting from Poisson's equation. This nonlinear ode/algebraic system of equations, with the boundary and initial conditions of the photoconductive-device problem, is integrated forward in time using Gear's method. The electron, hole, and displacement current densities are found from the carrier densities and electric potential in a post computation. The total current density is computed by summing the three current components, and the degree of spatial invariance as a function of time is used as a check of the accuracy of the computation.

The spatial semidiscretization of the nondimensionalized equations is performed assuming a nonuniform spatial grid. For the computations presented here, the nonuniform spatial grid has to be dense near the boundaries to resolve the boundary layer behavior of the densities and potential. Because the region requiring dense grid points is reasonably well-known and remains relatively constant throughout the computation, the nonuniform spatial grid can remain fixed. The dimensionless, discrete independent and dependent variables are designated by a “~”. The  $N$  nonuniform spatial grid points  $\tilde{x}_i \in [0, 1]$ ,  $i = 1, \dots, N$  are generated using the function

$$\tilde{x}_i(\zeta) = \frac{1}{2} + \frac{1}{2\zeta} \tanh \left[ \left( 2 \frac{i-1}{N-1} - 1 \right) \tanh^{-1}(\zeta) \right], \quad (5.57)$$

where  $\zeta \in [0, 1]$  sets the degree of nonuniformity of the grid points. For the computational results presented in this chapter, 101 grid points are used (including the boundary points) and  $\zeta = 0.99$ .

The accuracy of the computation is determined by checking the degree of spatial invariance of the total current density computed by summing the three current components. The spatial invariance of the total current density is a property of the continuous system of equations and

is not necessarily preserved in solving the system of discretized equations. The goal is to discretize the equations, allocate the spatial grid points, and integrate forward in time in a way that approximates the solution to the continuous equations. Checking the spatial invariance of the total current density computed by summing the three components is one way of determining the degree to which the discrete solution approaches the continuous solution. The discrete, dimensionless form of equation (5.24) is

$$\tilde{J}_{T_s}(\tilde{x}, \tilde{t}) = \tilde{J}_n(\tilde{x}, \tilde{t}) + \tilde{J}_p(\tilde{x}, \tilde{t}) + \tilde{J}_D(\tilde{x}, \tilde{t}), \quad (5.58)$$

where now the total current density computed by summing the three components (subscript "S") is not necessarily independent of  $\tilde{x}$ . The integral form of the total current density (subscript "I") corresponding to equation (5.26) is independent of  $\tilde{x}$ .

$$\tilde{J}_{T_I}(\tilde{t}) = \int_0^1 \tilde{E}(\tilde{x}, \tilde{t}) [\tilde{\mu}_n \tilde{n}(\tilde{x}, \tilde{t}) + \tilde{\mu}_p \tilde{p}(\tilde{x}, \tilde{t})] d\tilde{x} \quad (5.59)$$

Here the integral symbolically represents a quadrature scheme, such as Simpson's rule. A relative error based on the degree of spatial invariance of the summed current density  $\tilde{J}_{T_s}(\tilde{x}, \tilde{t})$  is defined as

$$\mathcal{E}_J(\tilde{t}) = \int_0^1 \left| \frac{\tilde{J}_{T_s}(\tilde{x}, \tilde{t}) - \tilde{J}_{T_I}(\tilde{t})}{\tilde{J}_{T_I}(\tilde{t}) + \alpha} \right| d\tilde{x}. \quad (5.60)$$

Here  $\alpha$  is chosen equal to  $\sim 1\%$  of the maximum current density and serves to keep the error  $\mathcal{E}_J(\tilde{t})$  well-defined at times when the current density is close to zero (e.g., the beginning of the excitation pulse). If this error is found to be greater than a few percent, the spatial region where the error was greatest is found, the spatial grid is adjusted to better resolve that region, and the computation is then re-run. This idea could be used as the basis of an adaptive mesh technique, but I have found that obtaining satisfactory results using a fixed nonuniform spatial mesh is straightforward. The region of greatest error is usually easy to identify, and this region does not shift greatly as the photoconductor responds to the excitation pulse. For the computational results presented in the following section of this chapter, the maximum value of the relative error was never greater than 2% and was frequently much less than 1%.

### Computational Results

The range of values that the parameters of the photoconductive-device model equations can take under various conditions is large. To provide an understanding of some of the behavior characteristics of a photoconductor, a number of cases are presented that cover a portion of the

parameter space. For all cases, it is taken that the photoconductor is uniformly illuminated [ $\eta(\hat{x}) \equiv 1$ ] and that the excitation pulse has a rectangular temporal shape [ $\phi(\hat{t}) = 0$  when the excitation is off and  $\phi(\hat{t}) = 1$  when the excitation is on]. The duration of the pulse is taken to be 250 ns (rising at  $\hat{t} = 10$  and falling at  $\hat{t} = 260$ ), which is long enough for the photoconductor to achieve a near-steady-state condition. Three different excitation intensities are considered in order to represent the linear, low-intensity-limit response; a medium-intensity response; and a high-intensity response. These three responses are demonstrated by using generation rates  $g_o$  of  $10^{18}$ ,  $10^{20}$ , and  $10^{22}$   $\text{cm}^{-3}\text{s}^{-1}$ .

The first case considers a photoconductor with a length  $L = 100$   $\mu\text{m}$  and an applied bias voltage  $V_o = 5$  V. This case represents an intermediate-length photoconductor operating under an intermediate-electric-field-strength condition of 500 V/cm. Two cases that differ only in using voltage biases of 1 V and 25 V, giving low- and high-electric-field-strength operating conditions, are then considered. Next, a case is considered with  $L = 10$   $\mu\text{m}$  and  $V_o = 0.5$  V. This represents a short photoconductor operating under intermediate-electric-field-strength conditions. Finally, a case with  $L = 1000$   $\mu\text{m}$  and  $V_o = 50$  V, which represents a long photoconductor

operating under intermediate-electric-field-strength conditions, is considered. The trapped space charge remaining after an excitation pulse means that a second pulse will have different initial conditions than the first pulse. The effect of this nonequilibrium trapped-charge distribution on photoconductor response is demonstrated by presenting the results of double-pulse computations performed with the parameters of the first case ( $L = 100 \mu\text{m}$  and  $V_o = 5 \text{ V}$ ).

The material parameters are chosen to represent InP:Fe. An electron mobility  $\mu_n = 2000 \text{ cm}^2/\text{Vs}$  and a hole mobility  $\mu_p = 100 \text{ cm}^2/\text{Vs}$  are assumed. A total deep-level-impurity (iron) density of  $N_T = 10^{16} \text{ cm}^{-3}$  with a thermal-equilibrium, negative-charge-state density  $n_{T_o}^- = 10^{14} \text{ cm}^{-3}$ , or 1% of the total density, is assumed. The trapping rate parameters are taken to be  $B_n = 1.6 \times 10^{-7} \text{ cm}^3/\text{s}$  and  $B_p = 1.2 \times 10^{-7} \text{ cm}^3/\text{s}$ . This choice corresponds to the modeling work presented in chapter 3 on the bulk-material transient photoconductive response of InP:Fe in giving the ratio  $B_p/B_n \approx 0.75$  and giving an equilibrium electron capture time constant of 0.63 ns.

The two free parameters,  $N$  and  $\tau$ , are chosen as  $N = 10^{15} \text{ cm}^{-3}$  and  $\tau = 1 \text{ ns}$  which gives reasonable values for the dimensionless

parameters. The resulting dimensionless parameters for the first case are

$$I = 10^{-6}, 10^{-4}, \text{ and } 10^{-2}, \quad (5.61)$$

$$\hat{N}_T = 10, \quad (5.62)$$

$$C = 0.01, \quad (5.63)$$

$$\hat{B}_n = 0.16, \quad (5.64)$$

$$\hat{B}_p = 0.12, \quad (5.65)$$

$$\hat{\mu}_n = 0.1, \quad (5.66)$$

$$\hat{\mu}_p = 0.005, \quad (5.67)$$

$$\sigma = 0.0052, \quad (5.68)$$

$$Q = 2884. \quad (5.69)$$

The three different values for  $I$  correspond to low-, medium-, and high-intensity excitations.

Because the electron mobility is approximately 20 times greater than the hole mobility, the electron current will dominate the hole current unless the hole density becomes much greater than the electron density. The equilibrium density of deep levels is taken to be predominantly neutral (capable of capturing electrons but not holes) and therefore the electron

capture rate is much greater than the hole capture rate. Time constants for equilibrium electron and hole capture are defined as

$$\tau_{n_0} = \frac{1}{B_n(N_T - n_{T_0}^-)}, \quad (5.70)$$

$$\tau_{p_0} = \frac{1}{B_p n_{T_0}^-}, \quad (5.71)$$

which have the values  $\tau_{n_0} = 0.63$  ns and  $\tau_{p_0} = 83$  ns for the parameter values chosen. These time constants dominate the recombination rate at low excitation intensities. Because  $\tau_{p_0} \gg \tau_{n_0}$  at low intensities, the hole density can far exceed the electron density and therefore the hole component of the current can become significant. At high intensities the percentage of negatively charged deep levels becomes greater because of electron trapping, and in the limit of very high intensity the electron and hole capture rates become equal. The dynamics of these trapping processes has been presented in chapter 3. In this chapter, a full description of the dynamics of the transient response of a photoconductor, which includes the important effects of transport and charge separation, is presented.

The computed results for the first case ( $L = 100$   $\mu\text{m}$  and  $V_0 = 5$  V) are shown in figures 5.1–5.5. Figure 5.1 shows the computed total current density for the three different intensities. The response of the

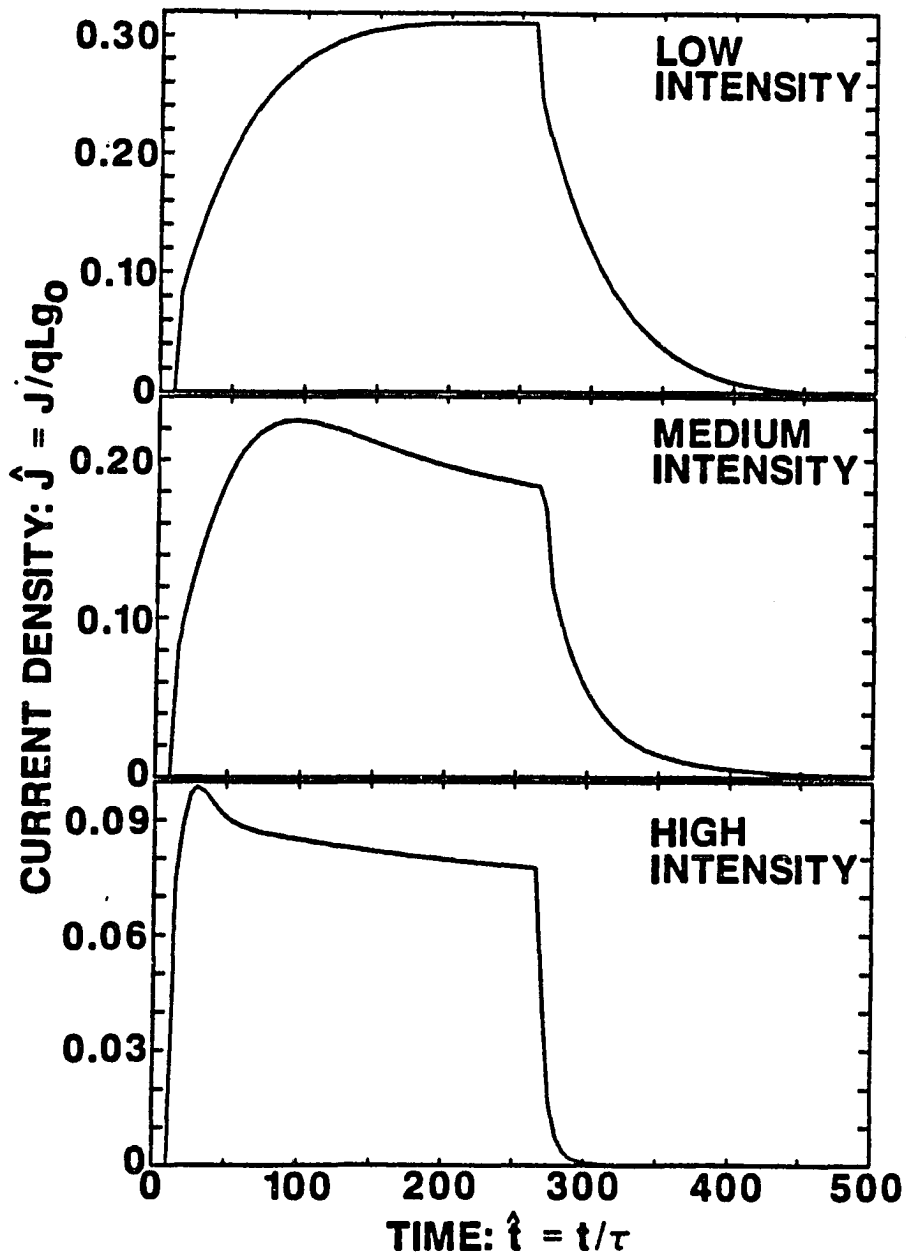


Figure 5.1: Normalized total current density as a function of time for a 100- $\mu\text{m}$ -long photoconductor with 5-V bias.

photoconductor is seen to be sublinear with intensity. A breakpoint between the fast-rising electron component of the current and the slower hole component of the current can be seen at approximately the same normalized amplitude (0.08) on the leading edge of the pulse for each intensity. The fall of the pulse also contains a fast electron component and a slow hole component. The decay tail, predominantly caused by hole current, relaxes faster at higher intensities, as expected because of the increased hole trapping rate (i.e., a larger density of negative trap sites are available to capture holes under high-intensity excitation than under low-intensity excitation). The medium- and high-intensity-excitation results show an overshoot in the total current. This overshoot is smaller and broader for the medium-intensity result than for the high-intensity result.

The spatial profiles of the electron density, hole density, and negative trap density at four different times,  $\tilde{t} = 0, 30, 250, \text{ and } 300$ , are shown in figures 5.2-5.4. The electron density profiles shown in figure 5.2 are quite uniform and linear with intensity in the central region of the photoconductor. The response of the electron density in this region is given accurately by trapping-kinetics rate equations alone. The time constant for the response at all three intensities is  $\sim \tau_{n_0}$  because the value of  $\Delta n_T$

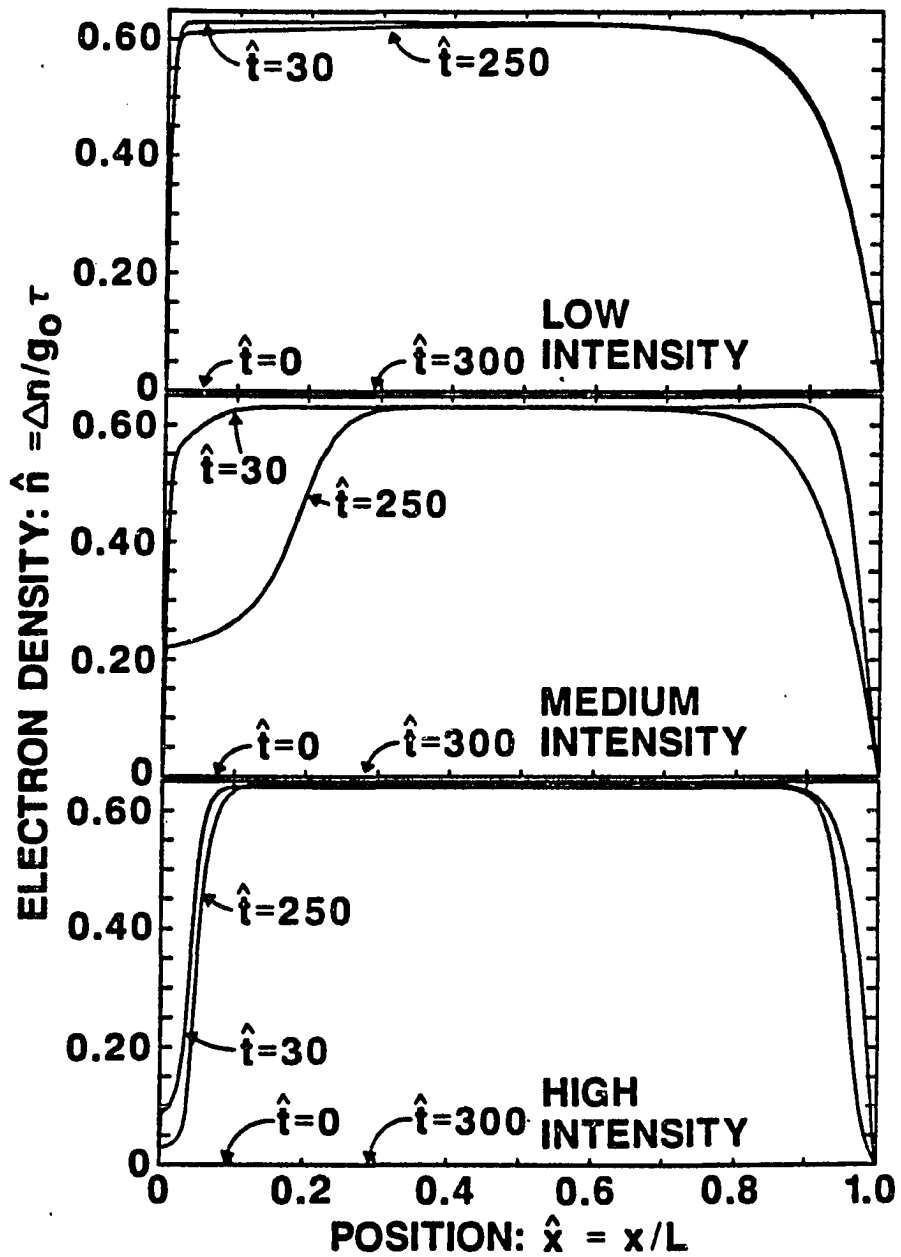


Figure 5.2: Normalized excess electron density as a function of spatial position at four different times for the case  $L = 100 \mu\text{m}$  and  $V_0 = 5 \text{ V}$ .

remains small relative to  $N_T$ . That is, the electron density rises to and falls from the value  $g_0\tau_{n_0}$  with a time constant of  $\tau_{n_0}$ . The electron density is only perturbed by the boundary effects in a narrow region adjacent to the electrical contacts.

The hole density profiles are shown in figure 5.3. At  $t = 30$  ns (20 ns after the pulse turn on), the central region densities are spatially uniform and nearly equal for the three intensities. At  $t = 250$  and 300 ns, the medium- and high-intensity results are spatially uniform in the central region of the photoconductor whereas the low-intensity profiles have no spatially uniform region. For those regions in which a spatially uniform density profile occurs, response times and values are given by trapping-kinetics rate equations alone. Under the high-intensity-excitation condition, the negatively charged trap density (which can capture holes) has been increased by a factor of 3, whereas, at low and medium intensities it has been changed very little. With an electric field of 500 V/cm, a hole takes  $\sim 50$  ns to drift halfway across the photoconductor. At low intensity the electric field is not greatly perturbed from the initial (spatially uniform) value and, therefore, the drift time is less than the hole trapping time  $\tau_{p_0}$ , which leads to a spatially nonuniform hole density. At medium and high intensities the electric

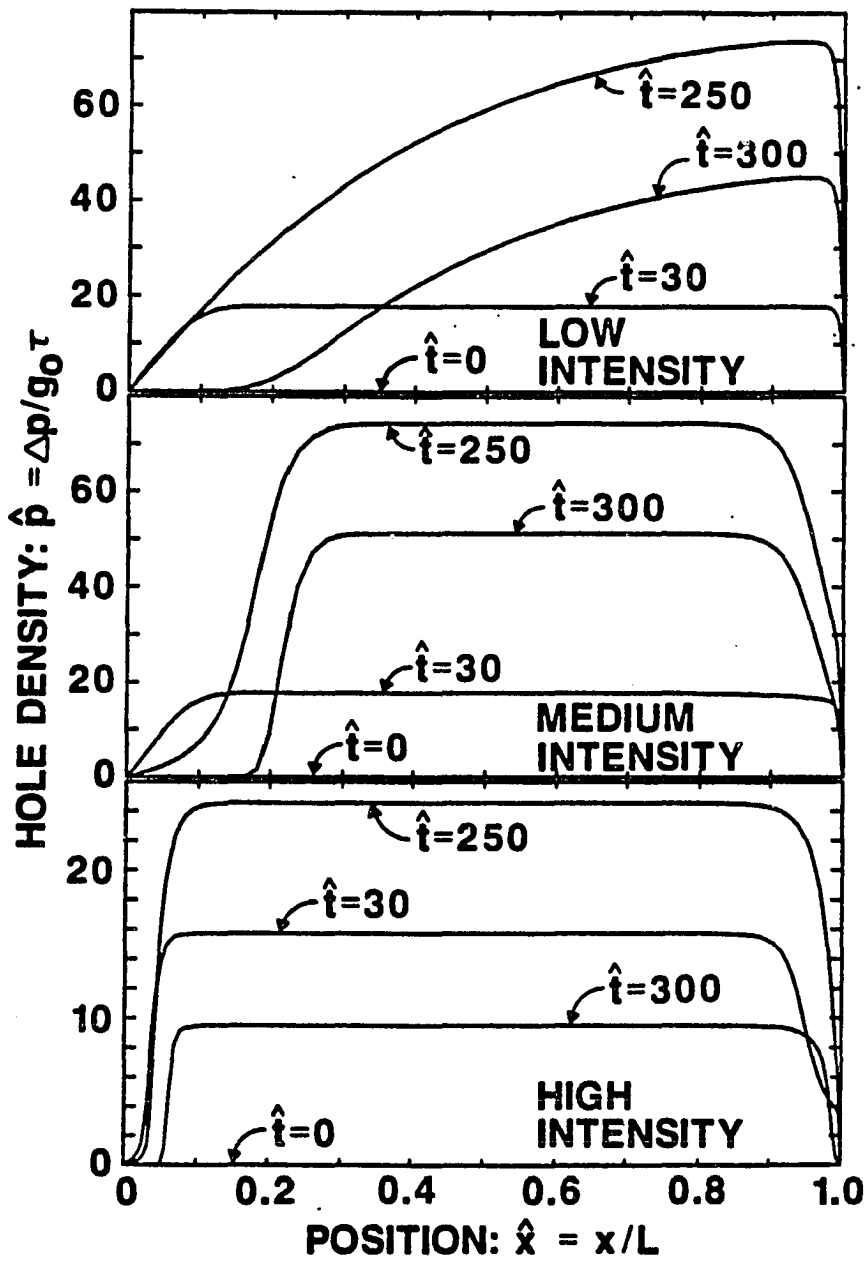


Figure 5.3: Normalized excess hole density as a function of spatial position at four different times for the case  $L = 100 \mu\text{m}$  and  $V_0 = 5 \text{ V}$ .

field is significantly reduced in the central region of the photoconductor (see figure 5.5). Therefore, the drift time is increased, resulting in spatially uniform hole profiles in this region.

The negatively charged trap density profiles are shown in figure 5.4. For regions in which both the electron and hole density profiles are uniform, the trap density profile is also uniform and is given by trapping-kinetics rate equations alone. At low, medium, and high intensities the maximum value of  $\Delta n_T^-$  is  $2.3 \times 10^{11} \text{ cm}^{-3}$ ,  $1.3 \times 10^{13} \text{ cm}^{-3}$ , and  $2.4 \times 10^{14} \text{ cm}^{-3}$ , respectively. These values are all small compared with  $N_T - n_{T_0}^-$ , so the electron capture rate is not significantly affected. However, the high-intensity value is comparable with the value of  $n_{T_0}^-$  and therefore the hole capture rate is significantly affected.

The electric field profiles are shown in figure 5.5. The electric field at the left contact has a value of  $\sim 9$  for  $\hat{t} = 30$ , a value of  $\sim 26$  for  $\hat{t} = 250$ , and a value of  $\sim 35$  for  $\hat{t} = 300$ . The low-intensity computation corresponds to a linear limit where the electron and hole equations are effectively uncoupled and the electric field remains essentially uniform. At medium and high intensities, significant space charge develops near the

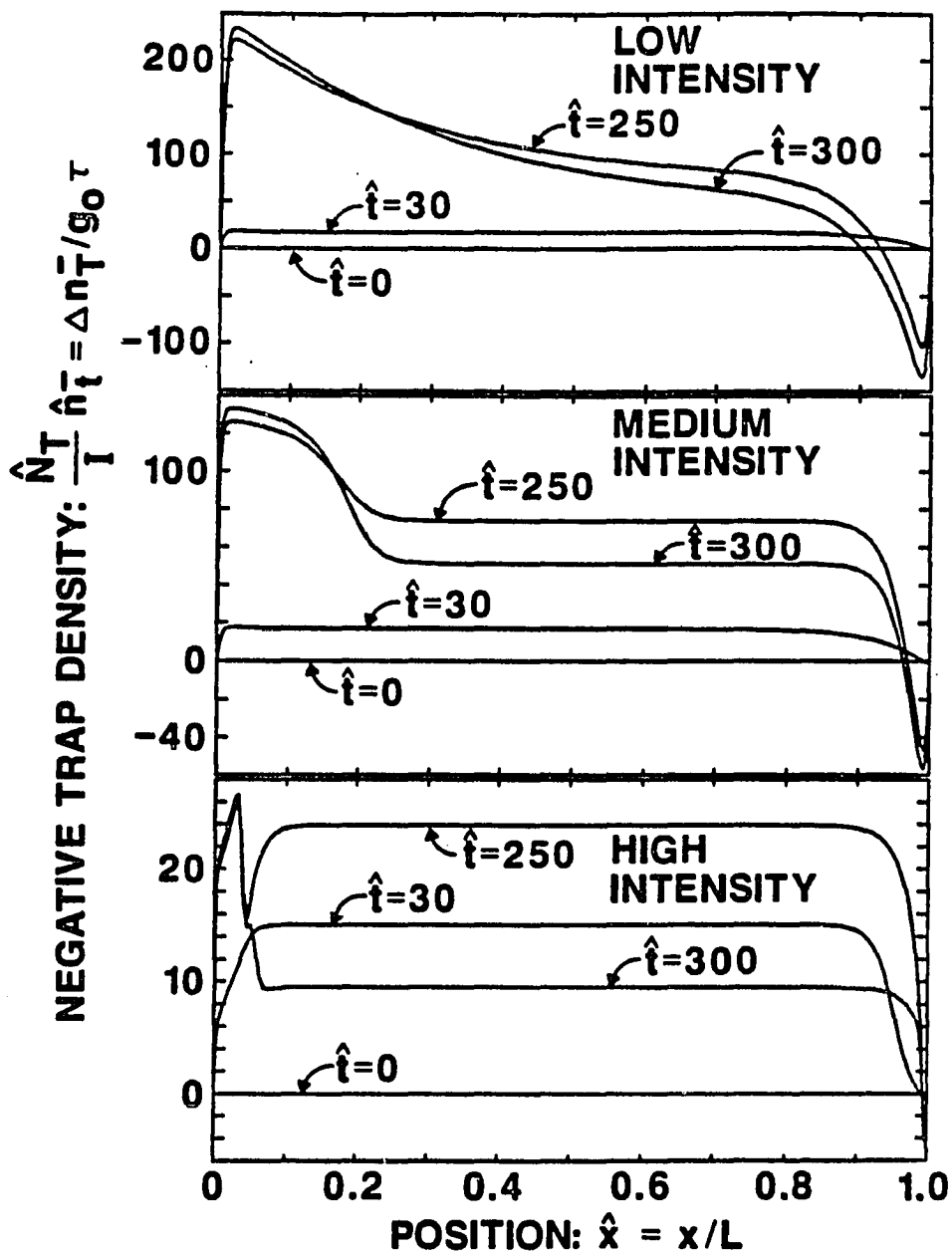


Figure 5.4: Normalized excess negatively charged trap density as a function of spatial position at four different times for the case  $L = 100 \mu\text{m}$  and  $V_0 = 5 \text{ V}$ .

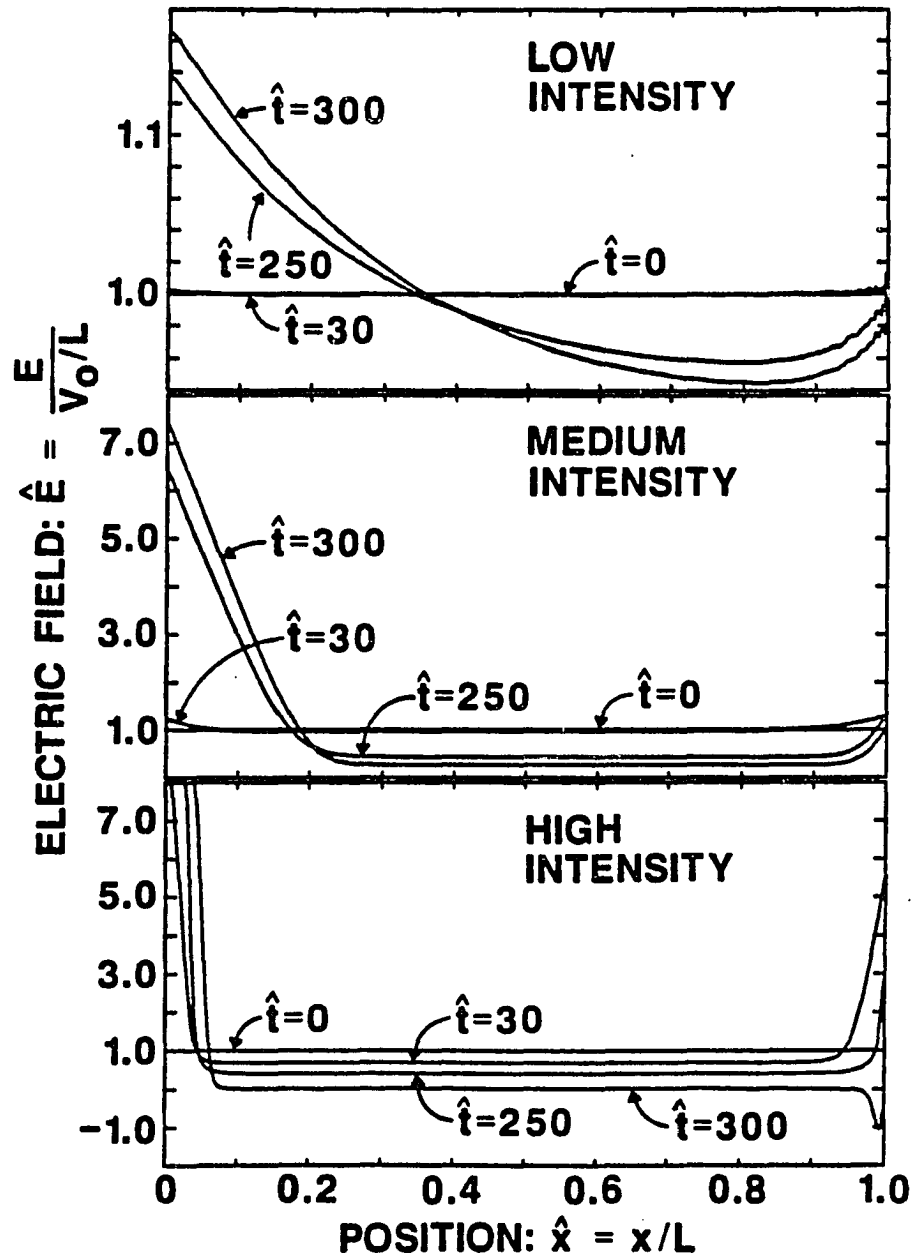


Figure 5.5: Normalized electric field as a function of spatial position at four different times for the case  $L = 100 \mu\text{m}$  and  $V_0 = 5 \text{ V}$ .

electrical contacts. This results in the electric field becoming very large near the boundaries and uniformly reduced in the central region of the photoconductor. The degree of nonlinearity caused by the coupling between the charged species and the electric potential is best seen by observing the degree of nonuniformity of the electric field profile.

As seen in figures 5.2, 5.3, and 5.4, large regions exist in which the densities are spatially uniform and have their dynamics described by the trapping-kinetics rate equations alone. However, this does not imply that the current densities are described by this model. Because the electric field is significantly reduced over these spatially uniform regions, the total current density computed by equation (5.59) is seen to be less than if the electric field remained uniform, as is assumed in the bulk-material-response model. Alternatively, the current density can be computed at a point, say in the spatially uniform central region of the photoconductor. It can be seen from equation (5.58) that the total current density is less because of the reduced electric field over a large portion of the photoconductor.

The slow overshoot of the current in the medium-intensity response and the faster overshoot in the high-intensity response seen in figure 5.1 results from the change in the electric field in response to charge

separation. The overshoot occurs because the electron density in the central region of the photoconductor reaches the maximum amplitude before the electric field has relaxed completely in that region. The rate at which the electric field relaxes to the final value is faster for higher carrier densities and can be thought of as a high-level-injection dielectric relaxation time.

Keeping all conditions the same except for the applied voltage, two other cases are considered with  $V_o = 1$  V and  $V_o = 25$  V. The total current densities at the three intensities for these two cases are shown in figures 5.6 and 5.7. Thus, figures 5.6, 5.1, and 5.7 show the device response for increasing electric-field strength. The device response is seen to be sublinear with bias voltage at all three intensities. The low-electric-field-strength case shown in figure 5.6 most closely resembles the bulk-material-response model. The magnitude of the response in figure 5.6 is less than that given by the bulk-material-response model, and the long-time-constant tails caused by hole current are less pronounced. As the bias voltage is increased the deviation from the bulk-material-response model, which would be linear in bias voltage, increases and the long-time-constant

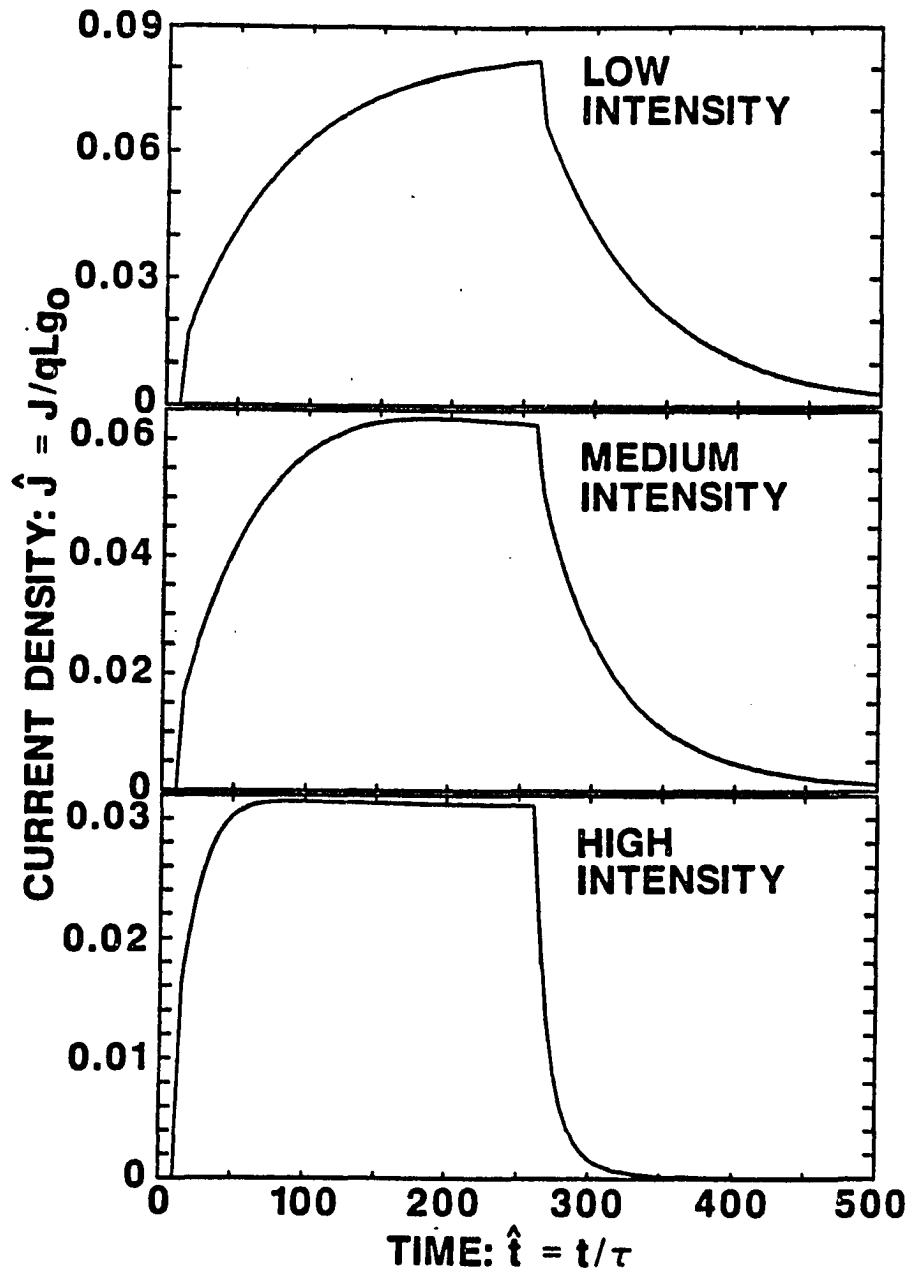


Figure 5.6: Normalized total current density as a function of time for a 100- $\mu\text{m}$ -long photoconductor with 1-V bias.

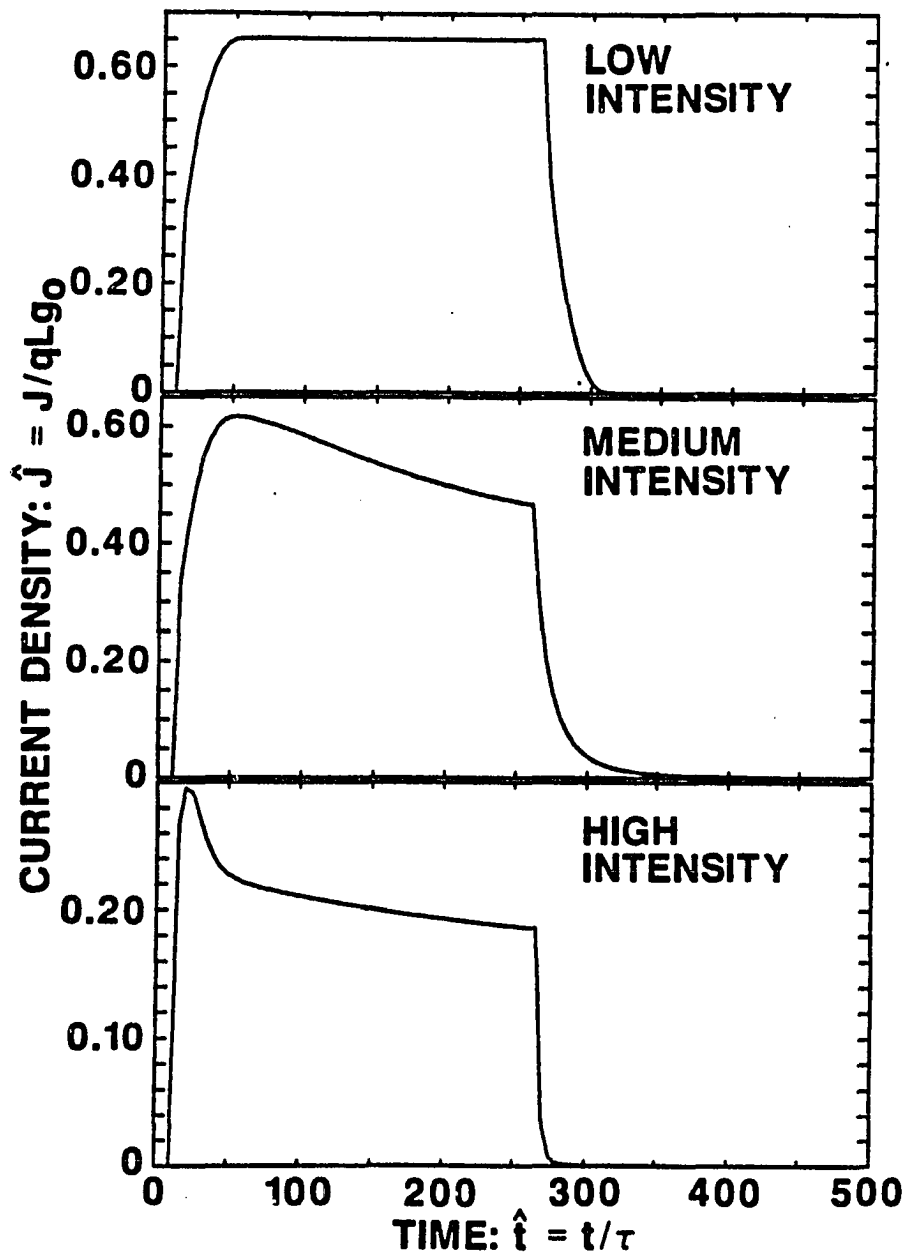


Figure 5.7: Normalized total current density as a function of time for a 100- $\mu\text{m}$ -long photoconductor with 25-V bias.

hole-current tails are reduced. At medium and high intensities the current overshoot becomes more pronounced with increasing bias voltage.

Keeping all conditions the same except for the device length, two other cases are considered with  $L = 1000 \mu\text{m}$  and  $L = 10 \mu\text{m}$ . The bias voltage for these two cases was taken to be  $V_o = 50 \text{ V}$  and  $V_o = 0.5 \text{ V}$ , respectively, so the equilibrium electric-field strength is the same as in the first case, namely,  $500 \text{ V/cm}$ . The total current density at the three intensities for these two cases are shown in figures 5.8 and 5.9. Thus, figures 5.8, 5.1, and 5.9 show the transient photoconductive response as a function of decreasing device length. The magnitude of the total current density (accounting for the length in the nondimensionalization) decreases with decreasing length. Going from  $L = 1000 \mu\text{m}$  (figure 5.8) to  $L = 100 \mu\text{m}$  (figure 5.1), the current density decreases by  $\sim 30\%$ . Going from  $L = 100 \mu\text{m}$  (figure 5.1) to  $L = 10 \mu\text{m}$  (figure 5.9), the current density decreases by a greater amount. Note that for the  $10\text{-}\mu\text{m}$  device, the response is nearly linear with intensity. The  $1000\text{-}\mu\text{m}$ -device response most closely resembles the bulk-material-response model. It also closely resembles the  $100\text{-}\mu\text{m}$ ,  $0.5\text{-V}$  case (figure 5.6) when current scaling is accounted for (multiply the figure 5.8 response by a factor of 2). As the length decreases the deviation

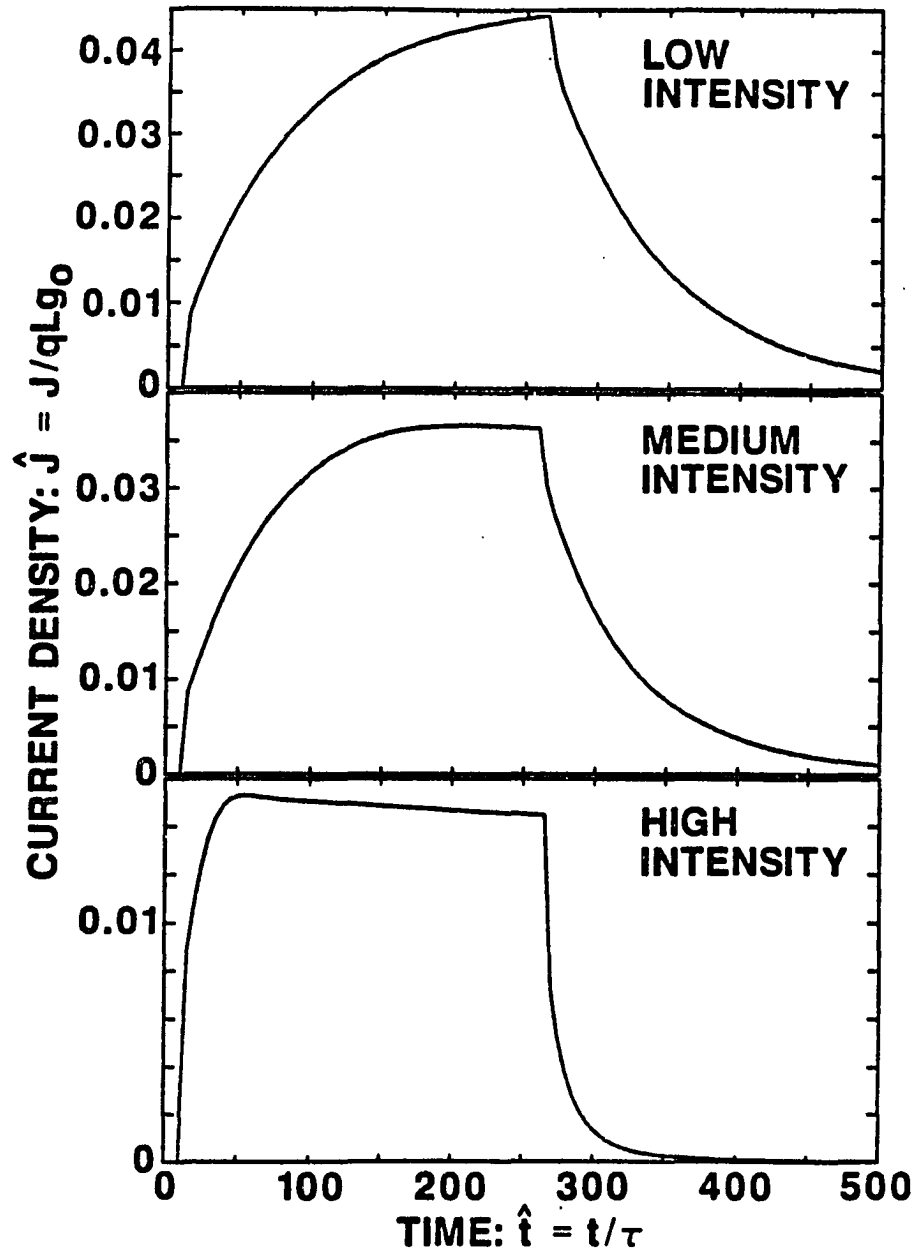


Figure 5.8: Normalized total current density as a function of time for a 1000- $\mu\text{m}$ -long photoconductor with 50-V bias.

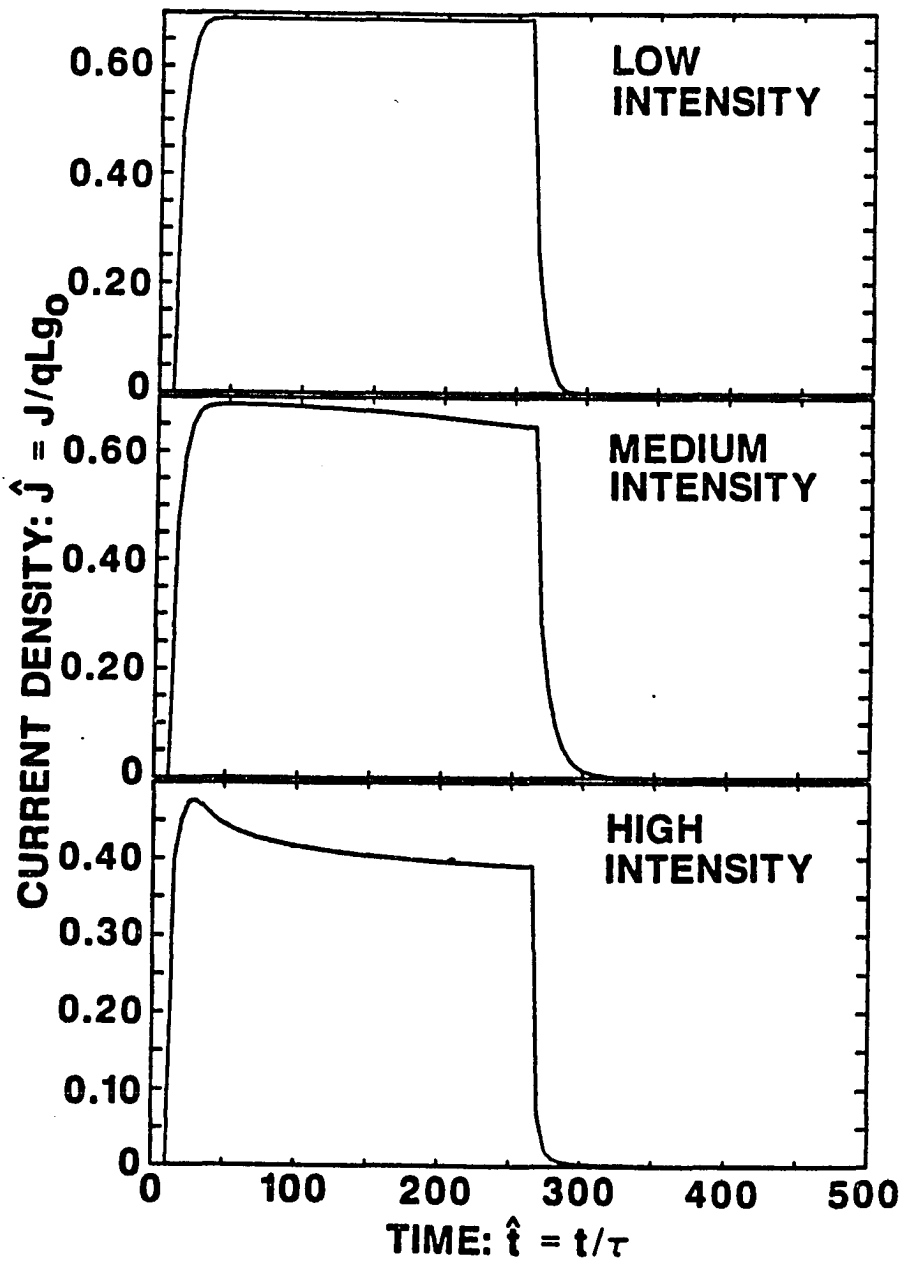


Figure 5.9: Normalized total current density as a function of time for a  $10\text{-}\mu\text{m}$ -long photoconductor with 0.5-V bias.

from the bulk-material-response model increases. The long-time-constant tails are reduced and overshoot effects appear.

One important aspect of device response results from the trapping of charge on deep-level impurities. The time constant for the return of the deep levels to their thermal-equilibrium charge state by thermal emission of electrons and holes can be quite long, i.e., as long as milliseconds. I have not included this thermal-emission process in my model equations because it is not important on the time scales that are considered in this chapter. The effect of the spatially nonuniform trapped-charge distribution on the photoconductor response comes about mainly through the electric field. After the electron and hole densities have returned to zero, the electric field may still be highly nonuniform because of the trapped-charge distribution. The photoconductor response to a second pulse may therefore be quite different than its response to the first pulse applied in thermal equilibrium, owing to the different initial conditions. Figure 5.10 shows double-pulse computational results using the same parameter values as the first case presented in this chapter ( $100\ \mu\text{m}$  and  $5\ \text{V}$ ). Note that for low-intensity excitation the photoconductor response to both pulses is the same, whereas at medium- and high-intensity excitation levels the response to the second pulse is

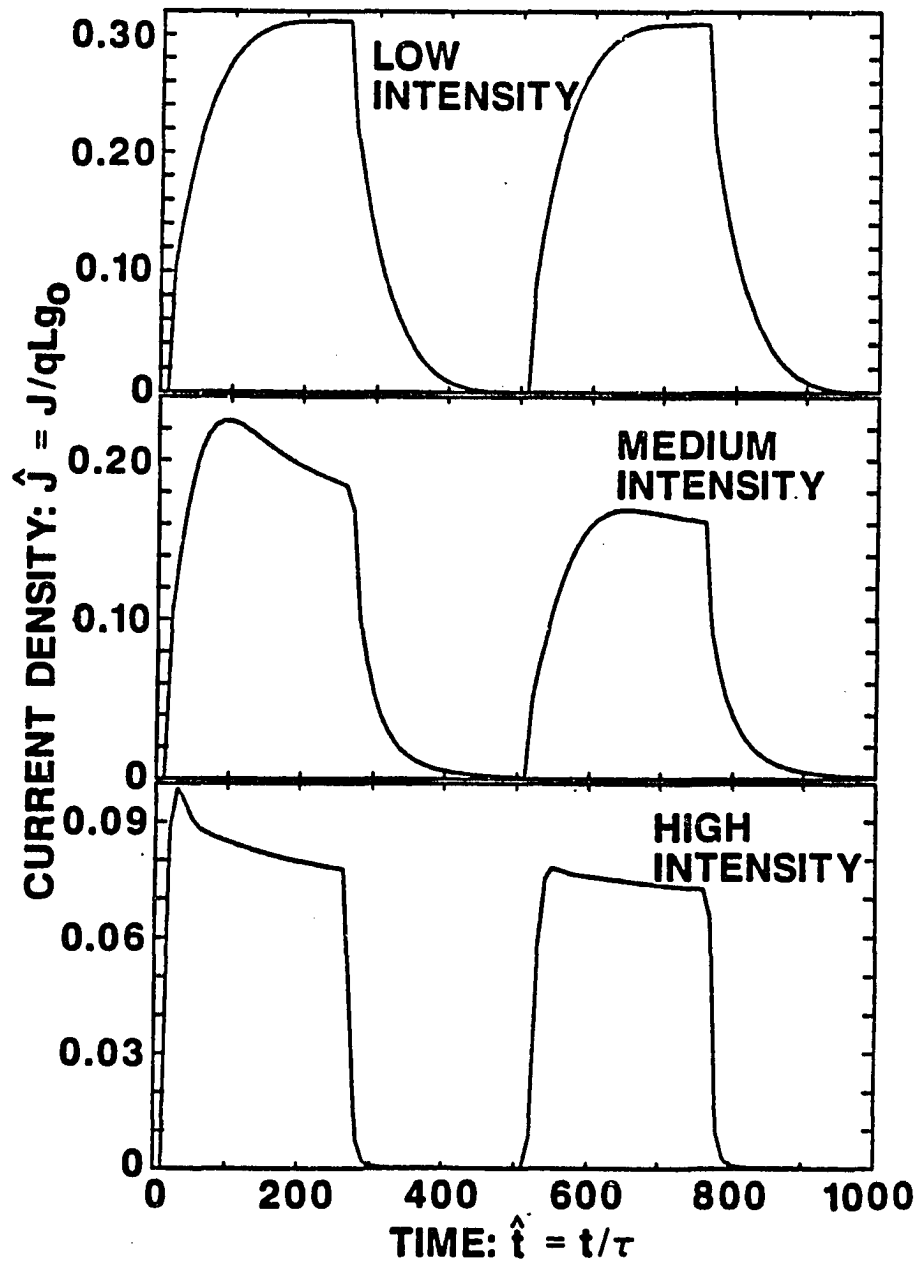


Figure 5.10: Normalized total current density for double-pulse excitation as a function of time for a 100- $\mu\text{m}$ -long photoconductor with 5-V bias.

quite different than the response to the first pulse. The current overshoot seen in the first pulse, resulting from the relaxation of the electric field, is reduced in the second pulse response. In a repetitive pulse experiment, a dynamic steady-state condition would be reached and the amount of overshoot would depend upon the repetition rate and the thermal-emission time constant. The thermal-emission time constant is an extremely strong function of temperature, and predicting its behavior requires detailed knowledge of the deep-level trap characteristics.

#### Experimental Observation of Overshoot

The overshoot behavior caused by the electric-field-relaxation time constant that was seen in many of the computations has also been experimentally observed. Figure 5.11 shows experimental data taken at four different intensities using an InP:Fe photoconductor with a 25- $\mu\text{m}$  gap length and an applied bias voltage of 30 V. The photoconductor was excited by a near-infrared, single-mode injection laser diode. The temporal shape of the excitation pulse was rectangular with subnanosecond rise and fall times, and the illumination of the photoconductor was nearly spatially uniform. The excitation intensity increases going from figure 5.11(a) to figure

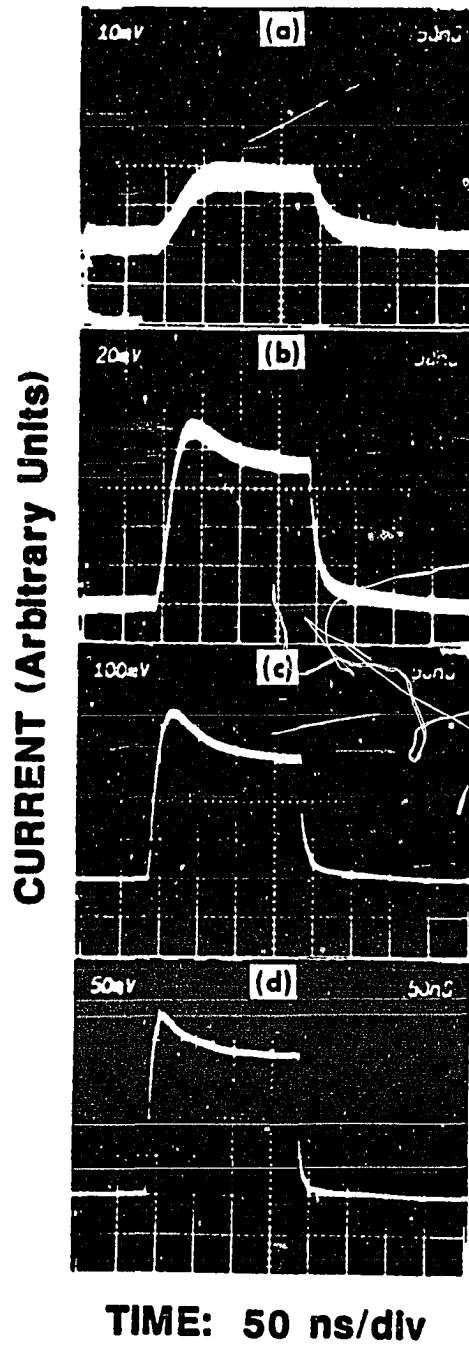


Figure 5.11: Experimental data showing overshoot behavior of the electron current component.

5.11(d). The data in panels (a)–(c) has an additional amplification factor of 10 as compared with the data in panel (d). The low-intensity response presented in panel (a) shows no sign of overshoot. Panel (b) shows the response at a higher intensity and overshoot is clearly visible. As the intensity is increased further, as shown in panels (c) and (d), the overshoot is seen to decay faster to the steady-state response in the same way as observed in the computational results. The experimental data is qualitatively consistent with the computational results, which show faster decay of the overshoot to steady state as a function of intensity.

### Conclusion

In this chapter, model equations that account for two of the most important factors in photoconductor transient response have been presented. One of these factors is the reduction of excess electron and hole densities by trapping on deep-level sites. The dynamics of this process are modeled as being proportional to the product of the carrier density times the number of available trapping sites on which that carrier type can be captured. The electron and hole densities are coupled by this process through auxiliary continuity equations for the density of available deep-level

trapping sites. This process is linear as long as the charge states of the deep-level trapping sites remain near their thermal-equilibrium values. The effect of changing charge-state density of deep-level trapping sites comes into the model quadratically with the carrier densities. The consideration of this process alone gives the basic material-response characteristics of the semiconductor, and in the case of InP:Fe, this simple model was studied in detail in chapter 3.

Another factor affecting photoconductive transient response which was considered was the convective/diffusive transport of electrons and holes. This process comes into the continuity equations for electrons and holes through the term for the divergence of the current density. The current densities are defined by the standard drift/diffusion model, which introduces the electric field as an important variable because the electric field is the dominant force for most operating conditions of photoconductors. The process of diffusion is important near the boundaries of the problem and is required to make the problem mathematically well-posed.

In the limit of long device length and low electric field, the response qualitatively approaches that of the bulk material. At high intensities the amplitude of the response is less than what would be predicted

---

from the bulk model, however, because of the reduction in the electric field over most of the length of the device. In the case of photoconductors that are not operating in this long-device, low-electric-field limit, transport is an important factor in photoconductor response. One important feature of the response in these cases is that of an overshoot in the current response. The overshoot comes about when the carrier density reaches its maximum value before the electric field has relaxed to its minimum value. The decay of the overshoot is faster for higher intensity excitation and indicates the time constant at which the electric field is relaxing.

The ability to faithfully reproduce an incident pulse shape is an important characteristic for a photoconductor used as a radiation detector. Linearity over a wide dynamic range of intensities is also very important. As indicated from the computational results presented in this chapter (in particular figure 5.9), these desirable characteristics would be best achieved using a short photoconductor with a large bias voltage.

Factors other than trapping and transport that contribute to photoconductor transient response may need to be considered in future modeling. One of these factors is the electrical contact characteristics, which may not have the ideal properties that were assumed. Another important case

to be considered is that of a photoconductor operating in a "switching" application, where the voltage across the photoconductor does not remain constant but may drop to some low value dependent on the intensity of the excitation and the impedance of the external electrical circuit. Velocity saturation and negative differential mobility also need to be considered in regions of high electric field.

---

## CHAPTER 6

### CONCLUSION

A model of the bulk-material photoconductive response based on the dynamics of electron and hole trapping and recombination on deep-level impurities was presented in chapter 3. From this trapping-kinetics, rate equation model, it was learned that the essential features of iron-doped indium phosphide that lead to the experimentally observed behavior are the following:

- (1) The electron mobility is  $\sim 20$  times larger than the hole mobility.
- (2) The capture rate coefficients of electrons and holes,  $B_n$  and  $B_p$ , are approximately equal.
- (3) At thermal equilibrium, the density of neutral iron sites (which can capture electrons) is much greater than the density of negatively charged iron sites (which can capture holes).

Because the electron mobility far exceeds the hole mobility, the electron current dominates the hole current in the photoconductor response

unless the density of holes is much greater than the density of electrons. At low intensities, the equilibrium population of iron charge states is not significantly changed by the photogenerated carriers. As a result, the capture rates of electrons and holes are independent of the carrier densities, and the electron and hole densities decay as independent exponentials with different time constants. The model equations describe this behavior in the limit of small  $I$ . In this case, the electron time constant is given by  $\tau_{n_0}$  and the hole time constant is given by  $(1 - C)\tau_{n_0}/BC$ . Because the neutral iron density exceeds the negatively charged iron density ( $C \ll 1$ ), the electron time constant is much less than the hole time constant. For low-intensity impulse excitation, the electron and hole densities are initially equal so that the electron time constant  $\tau_{n_0}$  dominates the response. For low-intensity pulse excitation with a pulse length much greater than  $\tau_{n_0}$ , the hole density can build up to far exceed the electron density. In this case, the contribution to the photoconductor response resulting from hole conduction is important. The photoconductor response will show a fast time constant owing to electron current and a slow time constant owing to hole current. Because of the larger contribution of hole current, the photoconductor response does not faithfully reproduce the driving pulse.

---

At high intensities, the electron and hole densities do not decay independently. Indeed, for electron and hole densities far exceeding the total iron concentration, the electron and hole densities are approximately equal. Thus, they decay together so that

$$\frac{d\Delta n}{dt} \simeq \frac{d\Delta p}{dt}. \quad (6.1)$$

This equation determines the charge-state densities of the iron impurities. The mutual decay time constant of the electrons and holes is seen to be

$$\tau_{HI} \simeq \frac{(1 - C)(1 + B)}{B} \tau_{n_0}. \quad (6.2)$$

This high-intensity time constant holds as long as the density of electrons and holes exceeds that of the iron impurities. For high-intensity impulse excitation, the electron and hole densities decay with the time constant  $\tau_{HI}$ . From equation (3.26) it can be seen that  $\tau_{HI}$  is somewhat larger than  $\tau_{n_0}$ . For high-intensity pulse excitation, the electron and hole densities are equal and respond with a time constant  $\tau_{HI}$ . Thus, for pulses which are long with respect to  $\tau_{HI}$ , the photoconductor faithfully reproduces the excitation pulse shape.

InP:Fe photoconductors are often used as radiation detectors. From the results presented here it is shown that, for low-intensity

excitation, the material response can be described as having two different time constants. The shorter time constant results from electron trapping and the longer time constant results from hole trapping. For radiation pulse lengths intermediate between these two time constants, detectors can faithfully replicate the temporal shape of the incident radiation signal. For radiation pulse lengths comparable to the longer (hole) time constant, the temporal response shape of the detector will be distorted. Of course, for radiation pulse lengths much longer than the hole time constant, the detector will faithfully replicate the radiation pulse shape. For high-intensity excitation, the detector response is determined by the single time constant  $\tau_{HI}$ . The detector will faithfully replicate a high-intensity radiation pulse which is long with respect to this time constant.

For fast pulse generation and sampling applications, the impulse response of the photoconductor is the important characteristic. My results show that the material response following impulse excitation is essentially an exponential decay. The decay time constant for low-intensity excitation is the equilibrium electron-capture time constant  $\tau_{n_0}$ . For high-intensity impulse excitation, the decay time constant  $\tau_{HI}$  is longer.

---

The model presented in chapter 3 qualitatively accounts for the experimentally observed behavior and provides an understanding of the photoconductive response of InP:Fe based on the trapping and recombination of electrons and holes on deep-level iron impurities. The model parameters  $B$  and  $C$  were chosen to provide the best agreement with the experimental data. It is not claimed that the values chosen for  $B$  and  $C$  accurately represent the true material parameters for InP:Fe. The model displays the same basic behavior with some variation in  $B$  and  $C$ , and some aspects of the model behavior are dependent on the  $BC$  product.

In chapter 4, a theory of the effect of deep-level centers on the generation-recombination noise and responsivity of an intrinsic photoconductor was presented. It was found that deep-level centers can influence the g-r noise in three main ways: (i) They can shorten the bulk excess carrier lifetime by Shockley-Read-Hall recombination. (ii) If the minority carrier capture rates are significantly larger than the majority carrier rates, they can trap the photogenerated minority carriers. This trapping reduces the effective minority carrier mobility and diffusivity and thus reduces the effect of carrier sweep out. (iii) The deep-level centers add a new thermal noise source which results from fluctuations between bound and free carriers. A

---

series of calculations were performed for a  $X = 0.21$ ,  $n$ -type  $\text{Hg}_{1-x}\text{Cd}_x\text{Te}$  photoconductor using the parameters of a commonly occurring deep-level center in this material. It was found that for typical bias, background, and temperature operating conditions (40 V/cm bias,  $10^{17}$  photons/cm<sup>2</sup>/s background, and  $T = 77$  K) detector performance begins to degrade as the deep-level center density begins to exceed  $10^{16}$  cm<sup>-3</sup>. For the deep level parameters in  $n$ -type HgCdTe there is little minority carrier trapping. (The majority carrier cross section is much larger than the minority carrier cross section.) To illustrate the effects of trapping, calculations were also performed in which the cross sections of the two carrier types were reversed from the physical HgCdTe values.

In chapter 5, model equations that account for two of the most important factors in photoconductor transient response have been presented. One of these factors is the reduction of excess electron and hole densities by trapping on deep-level sites. The dynamics of this process are modeled as being proportional to the product of the carrier density times the number of available trapping sites on which that carrier type can be captured. The electron and hole densities are coupled by this process through auxiliary continuity equations for the density of available deep-level trapping sites.

This process is linear as long as the charge states of the deep-level trapping sites remain near their thermal-equilibrium values. The effect of changing charge-state density of deep-level trapping sites comes into the model quadratically with the carrier densities. The consideration of this process alone gives the basic material-response characteristics of the semiconductor, and in the case of InP:Fe, this simple model was studied in detail in chapter 3.

Another factor affecting photoconductive transient response which was considered was the convective/diffusive transport of electrons and holes. This process comes into the continuity equations for electrons and holes through the term for the divergence of the current density. The current densities are defined by the standard drift/diffusion model, which introduces the electric field as an important variable because the electric field is the dominant force for most operating conditions of photoconductors. The process of diffusion is important near the boundaries of the problem and is required to make the problem mathematically well-posed.

In the limit of long device length and low electric field, the response qualitatively approaches that of the bulk material. At high intensities the amplitude of the response is less than what would be predicted

from the bulk model, however, because of the reduction in the electric field over most of the length of the device. In the case of photoconductors that are not operating in this long-device, low-electric-field limit, transport is an important factor in photoconductor response. One important feature of the response in these cases is that of an overshoot in the current response. The overshoot comes about when the carrier density reaches its maximum value before the electric field has relaxed to its minimum value. The decay of the overshoot is faster for higher intensity excitation and indicates the time constant at which the electric field is relaxing.

The ability to faithfully reproduce an incident pulse shape is an important characteristic for a photoconductor used as a radiation detector. Linearity over a wide dynamic range of intensities is also very important. As indicated from the computational results presented in chapter 5, these desirable characteristics would be best achieved using a short photoconductor with a large bias voltage.

Factors other than trapping and transport that contribute to photoconductor transient response may need to be considered in future modeling. One of these factors is the electrical contact characteristics, which may not have the ideal properties that were assumed. Another important case

---

to be considered is that of a photoconductor operating in a "switching" application, where the voltage across the photoconductor does not remain constant but may drop to some low value dependent on the intensity of the excitation and the impedance of the external electrical circuit. Velocity saturation and negative differential mobility also need to be considered in regions of high electric field.

## REFERENCES

- [3.1] S. Fung, R. J. Nicholas, and R. A. Stradling, *J. Phys. C* **12** (1979), p. 5145
- [3.2] P. S. Tapster, M. S. Skolnick, R. G. Humphreys, P. J. Dean, B. Cockayne, and W. R. MacEwan, *J. Phys C* **14** (1981), p. 5069
- [3.3] G. Bremond, A. Nouailhat, G. Guillot, and B. Cockayne, *Electron. Lett.* **17** (1981), p. 55
- [3.4] B. T. Debney and P. R. Jay, *Semi-Insulating III-V Materials*, edited by G. J. Reed, (Shiva, Kent, UK, 1980), p. 305
- [4.1] C. T. Elliot, *Handbook on Semiconductors*, Vol. 4, edited by C. Hilsum, (North-Holland, Amsterdam, 1981), p. 727
- [4.2] R. M. Broudy and V. J Mazurczyk, *Semiconductors and Semimetals*, Vol. 18, edited by R. K. Willardson and A. C. Beer, (Academic, New York, 1981), p.157

- [4.3] D. L. Smith, *J. Appl. Phys.* **53** (1982), p. 7051
- [4.4] D. L. Smith, *J. Appl. Phys.* **54** (1983), p. 5441
- [4.5] D. L. Smith, *J. Appl. Phys.* **56** (1984), p. 1663
- [4.6] D. L. Polla and C. E. Jones, *J. Appl. Phys.* **52** (1981), p. 5118
- [4.7] E. S. Rittner, *Photoconductivity Conference*, edited by R. G. Breckenridge, (Wiley, New York, 1956), p. 215
- [4.8] M. Lax and P. Mengert, *J. Phys. Chem. Solids* **14** (1960), p. 248
- [4.9] G. L. Hansen, J. L. Schmit, and T. N. Casselman, *J. Appl. Phys.* **53** (1982), p. 7099
- [4.10] G. L. Hansen and J. L. Schmit, *J. Appl. Phys.* **54** (1983), p. 1639
- [4.11] F. L. Madarasz, F. Szmulowicz, and J. R. McBath, *J. Appl. Phys.* **58** (1985), p. 361
- [5.1] D. H. Auston, A. M. Johnson, P. R. Smith, and J. C. Bean, *Appl. Phys. Lett.*, **37** (1980), p. 371
-

[5.2] P. R. Smith, D. H. Auston, and W. M. Augustyniak, *Appl. Phys. Lett.*, **39** (1981), p. 739

[5.3] D. H. Auston and P. R. Smith, *Appl. Phys. Lett.*, **41** (1982), p. 599

[5.4] W. R. Eisenstadt, R. B. Hammond, and R. W. Dutton, *IEEE Electron Device Lett.*, **EDL-5** (1984), p. 296

[5.5] W. R. Eisenstadt, R. B. Hammond, and R. W. Dutton, *IEEE Trans. Electron Devices*, **ED-32** (1985), p. 364

[5.6] D. R. Kania, A. E. Iverson, D. L. Smith, R. S. Wagner, R. B. Hammond, and K. A. Stetler, *J. Appl. Phys.*, **60** (1986), p. 2596

[5.7] D. R. Kania, R. J. Bartlett, R. S. Wagner, and R. B. Hammond, *J. Appl. Phys.*, **44** (1984), p. 1059

[5.8] W. C. Nunnally and R. B. Hammond, *Appl. Phys. Lett.*, **44** (1984), p. 980

---

[5.9] D. L. Scharfetter and H. K. Gummel, IEEE Trans. Electron Devices, ED-16 (1969), p. 64